Design and Optimization of the Periodic Porous Polymer Composite Metamaterial Electromagnetic Absorbers

by

Kanat Anurakparadorn

A dissertation submitted in partial fulfillment
of the requirements for the degree of
Doctor of Philosophy
(Macromolecular Science and Engineering)
in the University of Michigan
2024

Doctoral Committee:

Professor Alan Taub, Chair
Assistant Professor John Heron
Professor Jinsang Kim
Professor Eric Michelssen

Kanat Anurakparadorn

kanata@umich.edu

ORCID iD: 0000-0002-1831-5655

Dedication

As I embark on the journey to become the first member of our family to attain a doctorate degree, I am deeply moved to dedicate my efforts to several remarkable individuals who have played pivotal roles in shaping my path.

Firstly, to the great engineer and exceptional father.

Secondly, to the great scientist and extraordinary mother.

Thirdly, to the great grandma, a steadfast supporter.

To my great partner, the most significant person in my life.

To the great guardian, a brilliant lawyer and influencer.

A heartfelt thanks to my great siblings whose unwavering cheerfulness has lifted my spirits.

To all my teachers, both formal and informal, who have imparted invaluable life lessons.

Lastly, to everyone in my life—colleagues, friends, family, and more—whose love and support I can never fully repay.

This achievement is a collective triumph,

made possible by the encouragement and belief of each of you.

Acknowledgements

In reflecting on my comprehensive PhD journey and achievements, I extend heartfelt gratitude to the Royal Thai Government Scholarship and the forthcoming institution, King Monkut's Institute of Technology Ladkrabang, for providing the invaluable scholarship and opportunity that have brought me to this pivotal juncture.

Moreover, I express sincere appreciation to the University of Michigan, with special recognition given to my academic advisor, Dr. Alan Taub. His welcoming spirit into his team, coupled with insightful guidance not only on technical research but also on meaningful life lessons, has been instrumental in my academic and personal growth. I am thankful for his kind mentorship, unwavering patience in keeping me motivated, and assistance in attaining the designation of a qualified researcher. Additionally, a generous portion of funding from Dr. Taub significantly eased my life in a foreign country with markedly higher living costs than my country of origin. I am pleased to note his willingness to continue our collaboration as I embark on my new career in the academic field.

I express profound gratitude to all my family members, including my grandma, dad, mom, uncle, aunt in law, sisters, cousins, and all other relatives, for their unwavering love and support throughout my PhD journey. Special thanks to my partner, Yong, who has been one of the most important people in my life, standing by my side since the beginning of my life in the USA, and hopefully forever. My heartfelt appreciation goes to my emotional support animal, Nomdoo, a female silver Labrador retriever, who has been like a daughter, always cheering me

up and being a reason for me to stay alive. I extend my thanks to all friends in my life for their love and support.

For my PhD research and study, I am indebted to a multitude of individuals. I start by acknowledging the project collaborator, Dr. Eric Michielssen, who serves as both my teacher and dissertation committee member. His guidance has been crucial from the very beginning, especially when I had zero knowledge of electromagnetic fields. I extend my thanks to my previous academic advisor, Dr. Henry Sodano, for providing me with the opportunity to start performing research and for his guidance on composite materials, despite my lack of background at the beginning of my study.

My gratitude extends to all current and past members of my research committee, including Dr. Jinsang Kim, Dr. John Heron, and Dr. Max Shtein, for their assistance, suggestions, and provision of equipment that contributed to the completion of this research. Special thanks to Dr. Anthony Grbic and his team, especially Steve Young, for their invaluable help with knowledge and experience in the electromagnetic laboratory. I appreciate all professors and instructors of the courses I attended, as well as their assistants, for providing valuable knowledge in the field.

A heartfelt thank you goes to all personnel who helped train me on equipment and technical skills in the research. This includes both active and previous staff from Van Vlack undergraduate laboratories, such as Sahar Farjami, Keith McIntyre, Tim Chambers, Ying Qi, Jack Eilers, as well as technical staff from MSE, including Chris Christian and Kelvin Worth. Importantly, I express my gratitude to every graduate student, both current and past members of the Taub research team, including Avi Bregman, Wesley Chapkin, Yipeng He, Maya Nath, Caleb Reese, Aaron Gladstein, Randy Cheng, Anshul Singal, Dandan Zhang, Amy Langhorst,

Anita Luong, Xhulja Biraku, Xingkang She, Ankush Bansal, Jonathan Goettsch, Louise Batta, Jaime Perez, Gabrielle Grey, Yiheng Xiao, Steven Mamolo, Colin Romine, Seth Fox, and members of other groups, such as Erin Chapkin, Tony Chiang, Nguyen Vu, Brian Reaker, Cody Scarborough, Yiqiao Huang, Zhixiong Yin, Yixuan Chen, Jiwon Lim, and many more, for their support, collaboration, advice, and training. My sincere appreciation goes out to each one of you!

I also want to express my thanks to Dr. Lawrence Drzal and Mr. Edward Drown from MSU for lending me equipment and guiding me in its usage. For my PhD life at the University of Michigan, I am immensely grateful for the help provided by all leading people from Macro, including Dr. Jinsang Kim, Julie Pollak, and Hiba Baghdadi, and especially the students, including Julie Rieland, Jiwon Lim, Boojae Jang, Jennie Paik, Mengjie Yu, Tongqing Zhou, Jaehyun Jang, Lisha Zhang, Tianyu Yuan, and others, for welcoming me and being a part of the family.

I cannot envision my PhD life without the MSE family, including Ellen Kampf, Renee Hilgendorf, Shelley Fellers, Shelly Christian-Sherman, Debra Johnson, Lourdes Jorgensen, Tod Richardson, Amy Holihan, and other staff, and without their help and support. Special thanks to Mike Lazars from GGB dock, who is always kind in delivering heavy crates of lab supplies to our lab. I extend my gratitude to Mr. Alexander Hermanowski from the university legal office for saving me when I was in a critical stage of life. Thank you to all other University of Michigan personnel for their unwavering support.

Table of Contents

List of Tables

List of Figures

List of Acronyms and Symbols

A = Absorbance

ABS = Acrylonitrile Butadiene Styrene

BW = Operation Frequency Bandwidth

CBs = Carbon Blacks

CNC = Computer Numerical Control

CNFs = Carbon Nanofibers

CNTs = Carbon Nanotubes

DMF = N,N-Dimethylformamide

DOF = Degree of Freedom

EDX = Energy – Dispersive X-ray Spectroscopy

EM = Electromagnetic

EMI = Electromagnetic Interference

ERR = Electric Ring Resonators

FDM = Fused Deposition Modelling

FEA = Finite Element Analysis

FTIR = Fourier Transform Infrared Spectroscopy

GNPs = Graphene Nanoplatelets

GO = Graphene Oxide

H_c = Magnetic Coercivity

K = Wave Number

MWCNTs = Multi-walled Carbon Nanotubes

M_s = Saturation Magnetization

NRW = Nicholsen – Ross – Weir Method

OA = Oleic Acid

PEC = Perfect Electrical Conductor

PEG = Polyethylene Glycol

PEI = Polyetherimide

PEO = Poly(ethylene oxide)

P_i = Power of the incidence EM wave

PLA = Polylactic Acid

PML = Perfectly Matched Layer

P_o = Power of the EM wave that transmits through the shield

PP = Polypropyline

PVA = Poly(vinyl alcohol)

PVDF = Polyvinylidene Fluoride

R = Reflectance

RF = Radio Frequency

rGO = Reduced Graphene Oxide

RL = Reflection Loss

SE = Shielding Efficiency

SEM = Scanning Electron Spectroscopy

T = Transmittance

t = Thickness of the Material

TE = Transverse Electric Polarization

TM = Transverse Magnetic Polarization

TPU = Thermoplastic Polyurethane

UHMWPE = Ultra-high molecular weight polyethylene

V = Voltage at the Back of Material

VNA = Vector Network Analyzer

VSM = Vibrating Sample Magnetometer

WVIPS = Water Vapor Induced Phase Separation

XRD = X-ray Diffraction

Z_{in} = Input Impedance

Z_L = Intrinsic Impedance of the Load

Z_{mat} = Intrinsic Impedance of the Material

Z_o = Intrinsic Impedance of the Free Space

Γ = Reflection Coefficient

Γ_o = Reflection Coefficient at the back of the material

Γ_s = Phase – Shifted Reflection Coefficient

δ = Skin Depth

ε_o = Electrical Permittivity of the Free Space

ε^* = Complex Relative Electrical Permittivity

ε' = Real Complex Relative Electrical Permittivity

ε'' = Imaginary Complex Relative Electrical Permittivity

λ = Wavelength

ρ = Bulk Resistivity

σ = Electrical Conductivity

τ = Transmission Coefficient

θ = Phase Angle

μ_o = Magnetic Permeability of the Free Space

μ^* = Complex Relative Magnetic Permeability

μ' = Real Complex Relative Magnetic Permeability

μ'' = Imaginary Complex Relative Magnetic Permeability

ω = Angular Frequency

Abstract

This dissertation addresses the imperative need for affordable Electromagnetic Interference (EMI) shielding materials in the era of burgeoning wireless technology. The goal is to mitigate the vulnerability of electronic devices to undesirable incoming radiation. Ideally, these materials should provide protection by absorbing a broad spectrum of frequencies and be insensitive to the polarization and angle of incidence of the impinging fields. The research introduces next-generation EM absorbers, comprising composite materials in a periodic porous structure. These absorbers leverage the concept of metamaterials, focusing on enhancing EM resonances within the absorber structures to meet multiple user-specified objectives.

Polymer-based composites exhibit a promising capacity to customize EM intrinsic properties by adjusting the concentration and micromorphology of each constituent. Initial designs of fundamental polymer-based composites are tailored to meet specific application requirements, serving as a foundational benchmark for subsequent meta-structure designs. The emphasis is placed on meticulous consideration of composition, dispersion, and micromorphology to achieve desired electrical permittivity and magnetic permeability. Composites, comprising polylactic acid, graphene-based materials as conductive fillers, and $CoFe_2O_4$ as a magnetic constituent, are designed and fabricated to fulfill commercial requirements. Additionally, the surface modification of $CoFe_2O_4$ with oleic acid and polyethylene glycol demonstrates improved dispersion quality, particularly when a high volume fraction is introduced into the composite system. The resultant composite, fabricated through the

solution mixing method, achieves a maximum reflection loss (RL) of -38 dB at 0.63 GHz, with an operational frequency bandwidth (BW) at -20 dB for an absorber thickness of 2.3 mm. In comparison, the composite compounded via a twin-screw extruder, offering enhanced production capabilities, yields a maximum RL of -21 dB with a BW at -20 dB of 0.2 GHz at an absorber thickness of 2.0 mm.

EM-field-based finite element computational modeling and a Monte-Carlo optimizer are employed to design periodic porous meta-structures using the specified composites. Multi-objective functions, focused on maximizing RL and BW, guide the optimizer in selecting structures suitable for various applications. The optimizer identifies the most efficient structure as the truncated cone pillar with a Perfect Electric Conductor (PEC) on the top surface, achieved from the 2.3 mm thick absorber in the solution mixed composite. This structure significantly broadens the operation bandwidth at RL of -20 dB from 0.63 GHz to 1.8 GHz. Additionally, the optimizer shows the enhancement of RL for a poorly absorbing composite material produced by a twin-screw extruder, improving from -21 dB to -67 dB for a thickness of approximately 2 mm. This improvement is attributed to metamaterial behavior induced by resonance from the interaction between repeated pores, as confirmed by electric field distribution analysis.

This research includes guidelines for metamaterial manufacturing, introducing techniques such as traditional CNC, compression molding, and additive manufacturing. These guidelines can enhance processing parameters and aid in achieving desired absorber structures in future work. The outlined strategy in this research demonstrates the capability to design and produce metamaterial absorbers that enhance absorption performance. These absorbers not only exhibit elevated RL but also encompass additional benefits aligned with user-defined multiple objective functions.

Chapter 1 Introduction and Motivation

1.1 Electromagnetic Interference (EMI) Shielding

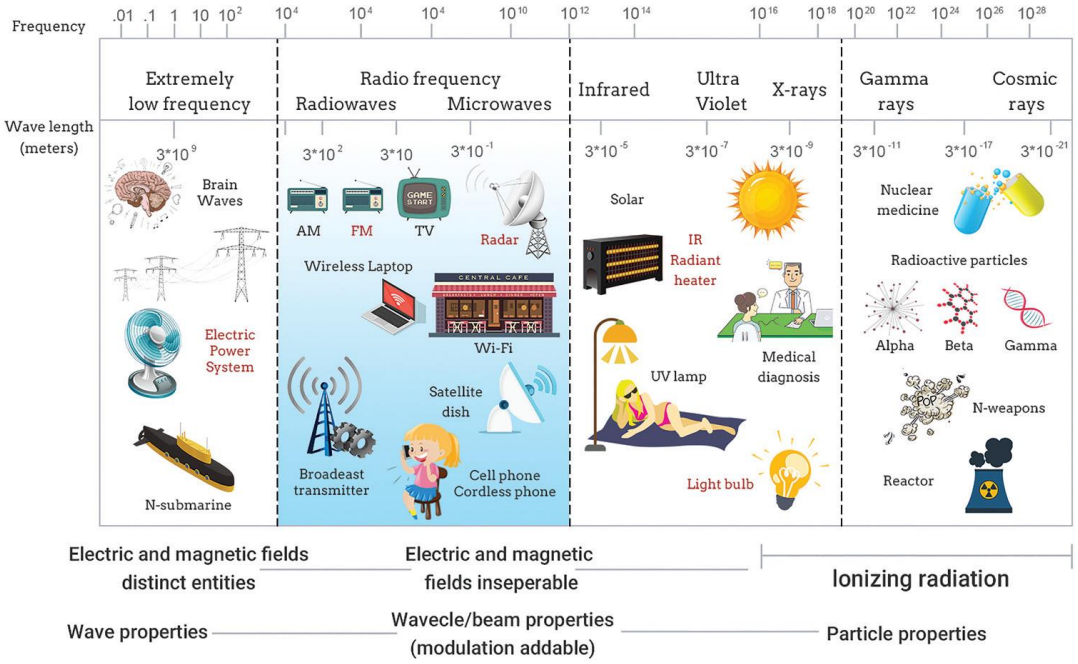

Figure 1-1 Examples of applications that use EM technology based on the frequency ranges adapted from [1].

In the current digitalized era, there is a swift acceleration in the pace of development and the extensive adoption of high-speed electronics and wireless technology in diverse applications. These applications (Figure 1.1) span a wide range based on the frequency ranges, including wireless communications, satellites, radar systems, electric transportation, camouflage military defense, and even everyday electronics in our daily lives (computers, mobile phones, antenna, electronic filters, Wi-Fi, etc.) [1–6]. Consequently, both desired and undesired electromagnetic (EM) radiation, generating electromagnetic pollution environment from the extensive utilization of these technologies, has progressively emerged as a significant concern. This radiation poses not only potential harm to human health [7–9] but also undermines the performance of electronic

devices by causing interference. Subsequently, there is a pressing need for the development of EMI shielding materials. Such materials aim to diminish the susceptibility of high-speed electronic circuits to undesired incoming radiation, ensuring the continued reliability and functionality of electronic devices.

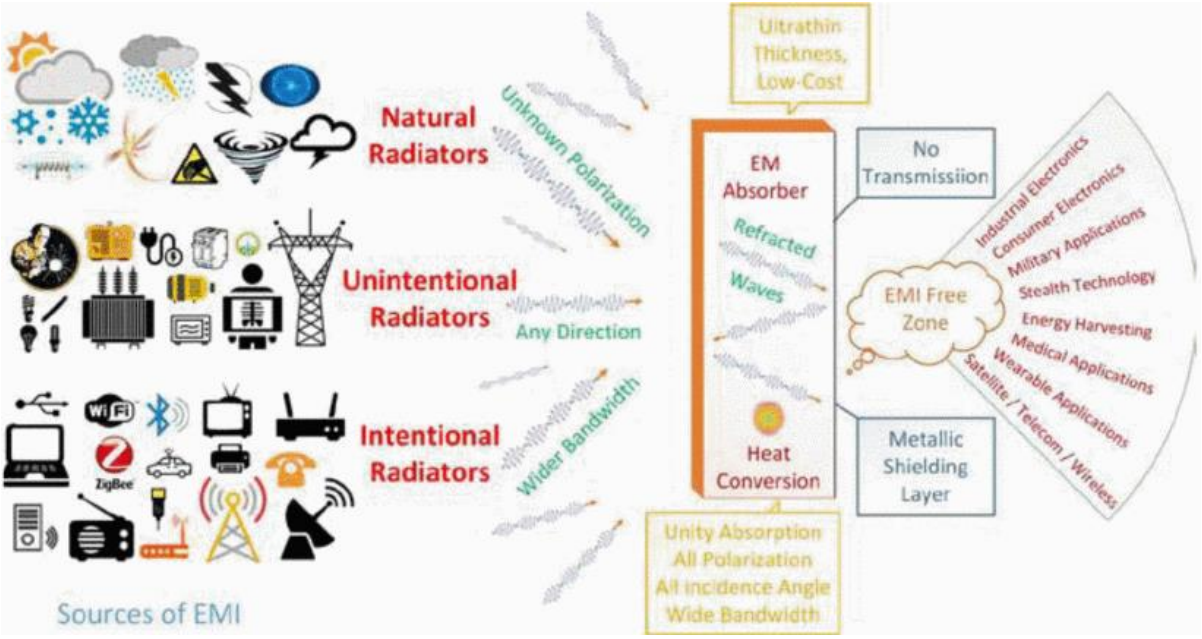

Figure 1-2 Schematic of the summary of EM absorption route adapted from [10].

EMI shields are generally classified into two categories based on their protective mechanisms: reflectors and absorbers. While reflector shields are easier to design and manufacture, they fall short in fully reducing EMI since reflected EM waves can still propagate and interfere with nearby devices. In contrast, absorbers are engineered to enhance the attenuation as the main mechanism. Figure 1.2 illustrates a schematic summary of the EM absorption pathway. The electromagnetic pollution environment originates from the radiation of natural sources, unintentional radiation sources, and intentional radiation sources. The randomized radiation and interference energy interact with the absorbers which convert this energy into heat [11]. In addition to high attenuation, modern EMI shielding materials must meet multiple objectives for current applications such as providing protection over a wideband of

operational frequency, being able to operate for both transverse magnetic and transverse electric polarizations and being able to absorb incident radiation from any direction and angle [6,12–15]. Therefore, researchers need to focus on developing cost-effective and for some applications also lightweight EM absorbers that fulfill these multiple objectives to effectively reduce EM pollution.

1.2 EMI Shielding Mechanism and Transmission Line Equations

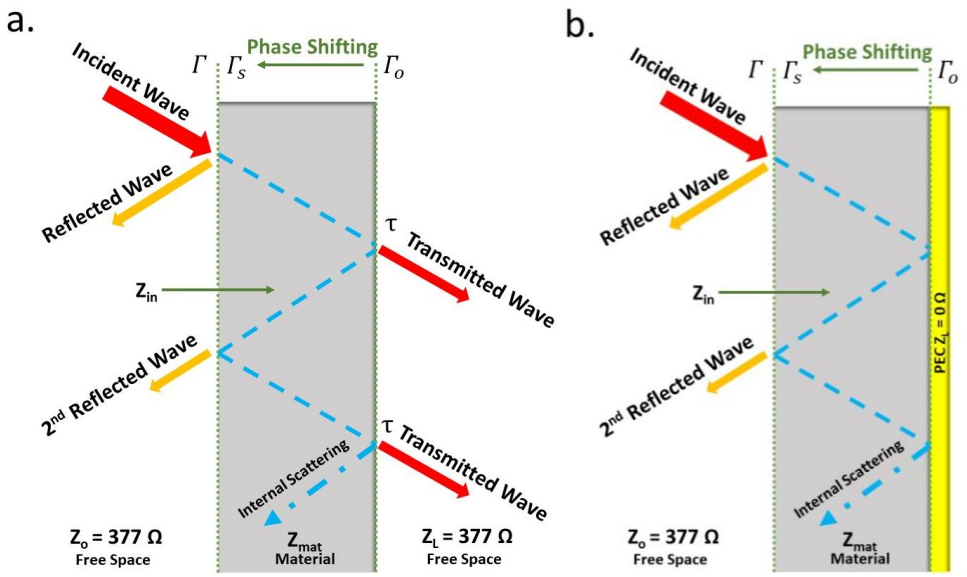

Figure 1-3 Schematic of the transmission line of a. air-backed shielding material b. PEC-backed shielding material.

The EM wave is constructed by the oscillation of electric and magnetic fields which are affected by the medium [16]. Hence, the effects of the material characteristics on the EM wave behavior are determined by complex electrical permittivity ($\varepsilon^* = \varepsilon' + j\varepsilon''$) and complex magnetic permeability ($\mu^* = \mu' + j\mu''$) of the material. The real parts of both parameters (ε', μ') indicate dielectric and magnetic energy storage respectively, while the imaginary parts (ε'', μ'') are associated with the energy dissipation in terms of dielectric loss and magnetic loss [17]. Reliant on the material characteristics and structures of the medium, the encountered incident wave at the front face of the shield can either be reflected at the surface, transmitted through the medium,

absorbed, or scattered causing the multiple reflections inside the medium. The multiple reflections lead to other outcomes such as secondary reflections and secondary transmission as shown in figure 1.3a. The energy of the reflected, absorbed, and transmitted waves can be described as the fractions of the overall energy which are reflectance (R), absorbance (A), and transmittance (T) respectively. By the law of energy conservation R+A+T =1. Hereafter, the ability to stop the transmission of the actual EMI shields can be represented as "Shielding Efficiency" (SE) which is the portion of the incident power that is not transmitted to the protected device defined in

$$\mathrm{SE} = 10log_{10}\left(\frac{P_i}{P_o}\right) \text{ (dB)} \tag{1.1}$$

where P_i is the power of the incidence EM wave and P_o is the Power of the wave that transmits through the shield.

Most EMI shielding applications require zero transmission from the medium to prevent radiation toward the protected objects. Therefore, a reflective layer is usually placed at the protected object side of many shields to reflect all the incident EM wave back to the original direction. As shown in figure 1.3b, this layer is usually made of high conductive materials that acts like a perfect electrical conductor (PEC). Consequently, the performance of the shields can be measured as the difference of the incident power and reflected power. This reduction results from the attenuation due to the absorption within the shield. The figure of merit is referred to as the "Reflection Loss" (RL).

$$\mathrm{RL} = 20log_{10}|\Gamma| \text{ (dB)} \tag{1.2}$$

where Γ is the reflection coefficient.

Both SE and RL can be quantitatively described from the theory of the transmission line [18–21]. The cutoff level of 20-30 dB of SE/RL is the lowest requirement for commercial

application, and acceptable for human exposition [22]. On the other hand, the military applications need much higher SE/RL at least 40 dB due to the sensitive behavior to the interference of the protected devices [3,5,23].

The transmission line equations provide the EM wave propagation behavior in terms of the reflection coefficient (Γ) and the transmission coefficient (τ) at the interfaces between materials. To obtain SE/RL of the shielding material, the first step is to determine the reflection coefficient at the back of the material slab (Γ_o) from

$$\Gamma_o = \frac{(Z_L - Z_{mat})}{(Z_L + Z_{mat})} \tag{1.3}$$

Here, Z_L represents the intrinsic impedance of the load, which is equal to $Z_o = \sqrt{\frac{\mu^0}{\epsilon^0}}$ if the material is backed by free space, where ϵ^0 = 8.854E-12 F/m is the electrical permittivity of the free space, and μ^0 = (4Π)E-7 N/A^2 is the magnetic permeability of the free space, or 0 if the material is backed by a perfect electric conductor (PEC). $Z_{mat} = \sqrt{\frac{\mu^*}{\epsilon^*}}$ is the intrinsic impedance of the fabricated material.

Subsequently, Γ_o is used to determine the phase-shifted reflection coefficient (Γ_s) that is shifted to the front face of the material slab:

$$\Gamma_s = |\Gamma| e^{j(\theta_o - 2kt)} \tag{1.4}$$

In this equation θ_o represents the phase angle of Γ_o, k is the wave number that is determine from $k = \omega\sqrt{\mu^* \cdot \epsilon^*}$ where ω is the angular frequency, and t is the thickness of the material slab. Consequently, the input impedance of the material can be determined by

$$Z_{in} = Z_{mat} \frac{(1 + \Gamma_s)}{(1 - \Gamma_s)} \tag{1.5}$$

The reflection coefficient at the front face of the material that is exposed to the free space (Γ) can be computed from

$$\Gamma = \frac{(Z_{in} - 1)}{(Z_{in} + 1)} \tag{1.6}$$

For transmission coefficient (τ) can be calculated from the voltage at the back of the material slab (V). This calculation can be started by setting up a two variables linear equation system.

$$a + b = 1 + \Gamma \tag{1.7}$$

$$a - b = \frac{1 + \Gamma}{Z_{mat}} \tag{1.8}$$

Then, V can be determined from

$$V = \tau = ae^{-jkt} + b^{jkt} \tag{1.9}$$

The shielding efficiency of the free space – backed materials can be determined by

$$SE = -20log_{10}|\tau| \text{ (dB)} \tag{1.10}$$

In order to determine the absorption of the material. The normal incidence RL for perfect electric conductor (PEC) backed materials can be determined by equation 1.2.

$$RL = 20log_{10}|\Gamma| \text{ (dB)} \tag{1.2}$$

where c is the velocity of electromagnetic waves in free space, and t is the thickness of the material.

From these transmission line equations, the main parameters that determine the shielding mechanism of the material are the intrinsic impedance of the material which is related to the material intrinsic properties (ε*, μ*). Electrical permittivity is directly linked to electrical conductivity, representing how well a material can respond to an electric field. Magnetic permeability is associated with the magnetization properties of composite materials, reflecting their ability to respond to a magnetic field. The absorption mechanism can be explained by the

interactions of the EM field with the material's molecular and electronic structure which cause the transformation of the incident EM wave energy into thermal energy leading to the heat dissipation. The ideal EM shield has 100% absorption, thus reducing 100% EM pollution and interference. The absorption effectiveness is related to the complementarities of the dielectric loss, magnetic loss, and the impedance characteristic of the materials. Hence, most EM absorbers are designed with lossy dielectric materials and/or with lossy magnetic materials. The dielectric loss ability is mainly dependent on the conductivity loss and polarization loss [24]. Higher conductivity (σ) enhances the imaginary part of the complex permittivity (ε"). However, ε" reduces while the angular frequency (ω) increases. This conductivity loss is the main mechanism at low frequency, while the polarization loss (ionic polarization, electronic polarization, dipole orientation, and interfacial polarization) dominates mainly at higher frequency [25]. The magnetic loss includes eddy current losses, dimensional resonance losses, magnetic resonance losses, domain wall resonance losses, and ferromagnetic resonance (electron spin) losses [10,26]. Moreover, proper impedance matching between the absorber materials with free space (377 Ω) can lower the front-faced reflection allowing the incident EM wave to enter into the absorber and convert to heat or be dissipated through internal interference via multiple reflections [27]. Thus, the absorbers are usually designed with low surface reflection.

1.3 Polymer Nanocomposites as EM Absorbers

Generally, the electrical and magnetic properties of the materials as well as the shielding geometry control the behavior and effectiveness of EMI shields. Because of their high shielding efficiency (SE) that meets requirements of most applications, EMI shields are traditionally fabricated from metal-based materials [28,29]. However, they exhibit high reflective behavior due to the mismatch of the wide difference of impedances at the front-face and the environment

which results in poor absorption characteristics. This lack of EM absorption combined with other disadvantages such as high density, low structural flexibility, limited processability, poor corrosion resistance, low environment stability, and durability reduces the viability of these materials in many EMI shielding applications. Polymer-based materials have been developed to create EM absorbers that can overcome many of these limitations [30]. Since most polymers are nearly completely transparent to EM waves, polymer composites with conductive and magnetic fillers were developed and are widely used as EM absorber materials.

Recently, lightweight, high conductivity, and high strength graphitic materials have been reported as potential fillers to enhance the mechanical, thermal, and electrical properties of the polymer composites [31]. By also incorporating magnetic particles and controlling the concentration and dispersion quality, the intrinsic electrical permittivity and magnetic permeability of these polymer composites can be tuned [32–35]. Thus, the level of reflection and absorption of polymer composites can be controlled for EM absorbing applications. Furthermore, the loss mechanisms which were discussed previously are also directly related to the electrical conductivity of the composites. Dhakate et al. [36] provided the recommended electrical conductivity range for the polymer composites filled with carbonaceous material for each application (figure 1.4). Notably, semi – conductive materials are needed for EMI shielding applications while more insulative materials are commonly used for electrostatic dissipation and more conductive materials are used for lightning strike protection.

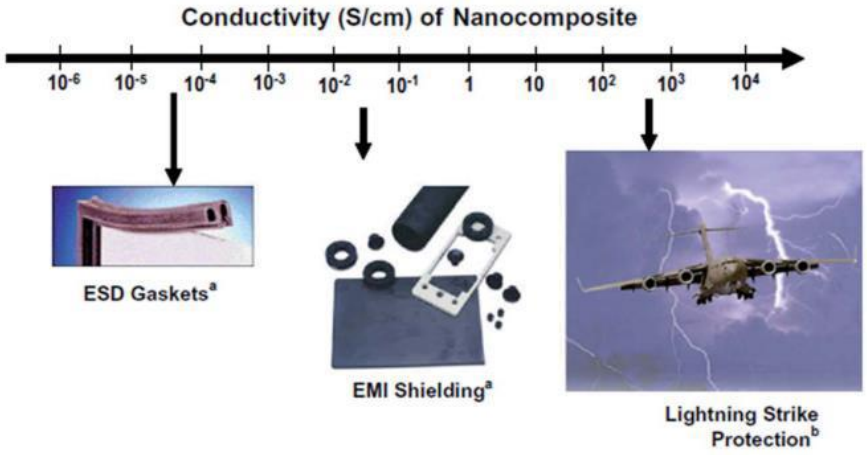

Figure 1-4 Schematic showing the conductivity range of the composites for different applications. Semi-conductive materials are used for EMI shielding applications, lower conductivity materials are used for electrostatic dissipations, and high conductivity is needed for extreme applications like lightning strikes protection.

Recent advancements have seen the extensive application of high aspect ratio, nano-sized fillers in polymer-based EM absorbers. Furthermore, the performance of the EM absorber can be enhanced with smaller unit sizes of fillers, mainly due to the skin effect. The skin effect refers to the phenomenon where electromagnetic waves penetrate only the near-surface region of the electrical conductor at high frequencies [37]. Nano-sized fillers provide an increased opportunity for uniform distribution, enabling the creation of outstanding electrically conductive networks [38]. The extent to which a conductive network of fillers is established plays a pivotal role in determining the conductivity of the composite material [30,39–41]. The percolation threshold signifies a critical concentration of conductive fillers, indicating the point at which conductive paths begin to form within the insulating matrix. The primary challenge in the development of conductive polymer composites lies in minimizing the percolation threshold of the filler while simultaneously enhancing the electrical conductivity of the composite. The composites exhibit electrical conductivity if they meet either of two conditions: a continuous filler phase in an enriched state, or a rich filler phase forming a continuous network, both of which contribute to achieving a low percolation threshold [38]. This threshold is influenced by various filler

characteristics, including shape, size, aspect ratio, spatial distribution in the matrix, adhesion to the matrix, and dispersion [42–44].

Table 1-1 Al Saleh et al. reported EMI SE of ABS-based composites with different aspect ratio of fillers [45].

Fillers	Size	EMI SE
15 wt% MWCNTs	Diameter/Length: 9.5nm/1.5μm	50 dB
15 wt% CNFs	Diameter/Length: 110nm/4.2μm	35 dB
15 wt% CBs	Diameter: 12 nm sphere	20 dB

For example, Al-Saleh et al. [45] conducted a study comparing the X-band EM interference shielding efficiency (EMI SE) of fillers with different sizes and aspect ratios, including multi-walled carbon nanotubes (MWCNTs), carbon nanofibers (CNFs), and carbon blacks (CBs) in an Acrylonitrile butadiene styrene (ABS) matrix (Table 1). The research revealed that the percolation threshold decreases for smaller-sized fillers with higher aspect ratios. This trend was consistent across various filler loadings.

In order to enhance the EM absorption capabilities, another effective strategy involves incorporating magnetic materials into conductive materials. The addition of magnetic components to composites serves to improve impedance matching with free space and introduces a magnetic loss mechanism (μ”), ultimately contributing to the absorption efficiency of the shielding materials [46]. Moreover, the interfacial polarization loss can also be enhanced when incorporated conductive polymer composites with multiple fillers. For example, Zeng et al. successfully produced EMI shields using PVDF (polyvinylidene fluoride) combined with nickel (Ni)/carbon nanotube (CNTs) hybrid filler (Ni@CNTs) [21]. The resulting film exhibited an impressive EMI SE of 102.8 dB/mm, accompanied by an absorption ratio of 81.3% when incorporating 10 wt% multi-walled carbon nanotubes (MWCNTs) and 2 wt% Ni@CNTs. The authors attributed the high absorption performance primarily to the notable electrical conductivity imparted by the CNTs. Furthermore, the heterogeneous structure featuring a

magnetic filler (Ni) offered additional advantages. The presence of Ni contributed to polarization loss at the interface between the constituents, enhancing overall absorption. Additionally, the introduction of magnetic loss by Ni in the Ni@CNTs sample played a crucial role in attenuating electromagnetic waves. This was achieved through natural resonance and eddy-current loss, further enhancing the EMI shielding capabilities of the composite material [47].

There are many other reports on utilization of conductive polymer composites in addition of magnetic fillers for EM absorber applications [48–61]. For examples, Li et al. [62] produced Nickel-Nitrogen/Carbon composites in paraffin matrix. The resulted RL is -32.31 dB with the absorption band width at -10dB (BW@10) of 12.79 – 18 GHz. Kong et al. [63] fabricated graphene modified with CNTs/poly(dimethyl siloxane) in paraffin composite that the resulting max RL is -55 dB with 10.1 GHs of BW@10.

1.4 Macrostructures of the EM Absorbers

The shielding mechanisms are dependent not only on the intrinsic properties (ε^*, μ^*) of the polymer composites, but also on the morphology of the shield structure. EMI shields have been developed in a variety of forms to enhance the absorption, as well as to achieve the desired multi-objectives. Traditionally, shields that consisted of laminations of bulk materials are easy to fabricate and demonstrate efficient EMI shielding ability. A single layer of material is the simplest structure. However, high loading of conductive fillers in the concentrations range from 20 wt% to 60 wt% is required for most of the single-layer shields to achieve the desired absorption [64]. It can be observed from the transmission line equations that if the thickness of the material is equal to a quarter of the wavelength ($\lambda/4$), the phase reflection coefficient is shifted π rad along the thickness of the of the material. This results in π rad phase lag of the reflected wave to the incidence wave at a certain frequency. This model is called the quarter

wave matching model which is satisfied for all the odd multiple of λ/4 (i.e., for n λ/4, n = 1,3,5…).18 Therefore, manipulating the shield thickness is one of the common techniques to improve the absorption at a certain frequency which may not be applicable in most applications that require small thickness and lightweight characteristics [3,65]. On the other hand, multilayer laminates take advantage of internal reflections at the interface due to the impedance mismatch between layers to enhance attenuation as introduced by Lin et al [66]. All samples have the same thickness of 1 mm. However, it can be observed that there is no guarantee that any multilayer will have a higher absorption than the individual layers as in the case of PPC and PPC-PVA-PPC. The impedance matching which also contributes to the level of absorption is strongly dependent on the thickness of each layer, as well as the permittivity and permeability of each layer. While the laminated structure yields the benefit of interface reflection, the impedance matching can be decreased due to the change of material thickness which can lead to lower SE.

1.5 Porous Structure EM Absorbers

As an alternative to multilayer laminates, porous materials have also gained attention for EMI shielding due to their benefits of lower density and less material required to achieve sufficient EMI SE compared to the bulk materials. Fletcher et al. [67] compared the EMI SE of foamed and unfoamed structures of fluorocarbon/CNT composites. The foamed structures exhibit ~2dB lower SE compared with bulk structures for five concentrations of CNT varied from 0 – 12 wt%. In addition, the benefit of 30% weight reduction was achieved. Thomassin et al. [68] reported the decrease in dielectric constant in foamed multiwalled-CNT/Polycaprolactone composites compared with un-foamed, while the electrical conductivity is approximately 3 to 4 times higher. The reduction was attributed to the presence of the air pores leading to better impedance matching. Thus, the front face reflection of the shield can be

lowered, reducing the overall reflectivity of the shield. Therefore, the introduction of air porosity also induces the absorbance-dominated behavior of shielding. Ling et al. [55] reported low density (0.3 g/cm3) graphene/polyetherimide (PEI) nanocomposites foams for EMI shielding applications. The SEM micrograph characterization shows the obvious orientation of graphene on the cell wall of the porous structure. This is caused by the applied biaxial stretching action during cell growth. This stretching pushes the surrounded graphene to the cell wall which results in the enrichment of graphene inter-connectivity and forming conductive networks. Thus, the DC electrical conductivity increases two order of magnitudes (3.9 x 10-10 S/cm to 1.75 x 10-8 S/cm), while the graphene loading decreases (1.13 vol% to 0.39 vol%) from un-foamed sample to foamed sample. The electrical percolation threshold also decreases by the foaming process from 0.21 vol% to 0.18 vol%. Approximately 5 dB lower EMI SE of the composite foam compared with un-foamed composite was reported for all concentrations, however; the specific EMI SE (dB/(g/cm3)) was about 2 times increased by the process. The authors also suggested that the introduction of air porosity not only decreases the dielectric constant, but also enhances the internal reflection and scattering due to the impedance mismatch between the air pores and the composite. Thus, the EM waves were difficult to escape from the structure before being attenuated into heat. The effect of filler enrichment at the cell wall was also confirmed by Ameli et al. [69,70] who studied the EMI shielding of CNF/polypropylene (PP) foams. Higher EMI SE of the foams were reported. They claimed that more random orientation of CNF leads to a higher chance to form conductive networks. Similarly, Shen et al. [70] prepared PEI based composite foams filled with rGO/Fe_3O_4 by water vapor induced phase separation (WVIPS) process. With the same EM absorption mechanism, the absorption dominated SE was achieved at 41.5 dB/(g/cm3) in X-band. Alkuh et al. [71] studied the relationship of EM absorption properties and

the cell structure of poly (methyl methacrylate)/MWCNT foams which were prepared by CO_2 pressurization and fast cooling. The obtained cell size, shape, and density were influenced by multiple process parameters such as temperature, depressurization rate, filler loading, etc. which affects the EM absorption ability. This implies the difficulty to control the morphologies of the porous structure by the foaming process to obtain the desired EMI shielding characteristics. They also found that for the processing conditions that make the cell wall get thinner and become polyhedron shape, the MWCNTs nonuniformly distribute and accumulate at the cell struts which leads to discontinuous of the conductive networks [72].

Inspired by the foams, complex structures of EMI shield structure consisting of cellular patterns of dielectric materials with conductive materials as the cell wall have emerged as a new forms of EM absorber. Yan et al. [73] introduced the segregated structure of rGO/Ultra-high molecular weight polyethylene (UHMWPE) composite. The powders were fused into bulk-solid composites with a segregated structure. This structure allows rGO to form continuous conductive networks leads to a very low percolation threshold at 0.063 vol% with DC conductivity of 3.4 S/m. High absorption-dominated EMI SE (28.3-32.4 dB) can be achieved at low rGO loading (1.5wt%) of 2.54 mm thick sample. Jiang et al. [74] reported the similar work with rGO/TPU composite. Additionally, the air pores were introduced into the TPU cells via the supercritical CO_2 foaming method. SE of 21.8 dB of 1.8 mm thick sample was achieved with only 3.17 vol% rGO. The absorption through the impedance matching via the introduced air pores and internal reflection and scattering by multistage cellular structure is the main shielding mechanism. Castles et al. [75]reported the dielectric characterization of 3D-printed $BaTiO_3$/ABS composites in complex rod-connected diamond photonic crystal structures. The resulted material has loss tangents in the range of 0.005 - 0.027 for frequency around 15 GHz. Song et al. [76] decorated

CoFe alloy on hierarchically porous carbon fibers by using natural alginate fibers. The treated fibers were immersed in paraffin wax for EM absorption characterization. The resulting absorber provided the maximum RL of -69.1 dB with BW@10 of 5.2 GHz. Yin et al. [77] 3D printed rGO/ Polylactic Acid (PLA) composites into multilayer cross - shaped repeated structures. The gradient index size of each cross – shaped unit cell and thickness of each layer were varied to study the absorption. The fabricated absorber can achieve absorption above 90% with BW@10 broaden from 4.5 – 40 GHz. Similar 3D printing method was presented by Shi et al. [78] that repeated cellular porous structures were fabricated from CNTs/GNPs/PLA composites. The EMI SE of 36.8 dB can be achieved. Yuan et al. [79] produced structural EMI absorber of carbon/rGO honeycomb structure. The EM waves were subjected to multiple reflections by the highly conductive cell wall and were absorbed by multi-layer porous rGO foam. This work demonstrated the strategy for designing novel high- performance lightweight EM absorber by engineering the structure of the material. Moreover, the controllable morphologies allow us to achieve the desired EMI shielding performance. Other works on honeycomb structures of polymer composites for EMI shielding were also reported [78,80–82]

1.6 Metamaterial EM Absorbers

Another strategy to enhance the absorption of EMI shielding via engineering its structure is based on the concept of "Metamaterials" which refers to the artificial structure that has the ability to exhibit exotic effective properties that are impossible to achieve with natural material [83]. For the EM field, EM metamaterials refer to material structures that consist of arrays of structured subwavelength elements which may be described as effective electrical permittivity and magnetic permeability [84]. The interactions of the repeated elements with incidence EM wave result in resonance of the electric field within the material [83] By controlling the structure

of the repeated units, resonance of the EM fields can be created at specific positions inside the absorber which leads to nonuniform distribution of the fields and establishing the dipolar relaxation process. This results in dielectric loss, ohmic loss, interference, and impedance matching mechanisms [15,85]. Enhanced absorption is obtained while the periodic geometries of the shield meet the conditions that create resonant waves of the EM field in the interior of the shield and dissipated into heat [85]. Thus, this kind of material allows us to achieve absorption characteristics that are far beyond what can be achieved from monolithic materials.

Traditional EM metamaterial absorbers consist of three layers, the dielectric layers are located in the middle which is coated with highly conductive material as the bottom layer. A periodic structure of metal is placed on the top surface as the resonance unit [15,85–90]. Landry et al. [89] were the first to introduce the resonant metamaterial for EM absorber applications in 2008 [91]. They proposed a structure consisting of arrays of electric ring resonators (ERR) on the top layer of a dielectric matrix which provides the electric response coupling strongly to the incident electric field at the resonance frequency. Inspired by this work, there are more reports on the development of EM absorbers using metamaterial concept. Shen et al. [15] presented the triple-band metamaterial absorber. The consolidated single unit cell is composed of three interlocked electric closed-ring resonators and a metallic ground plane, with a dielectric layer serving as a separator. Both simulation and experimental outcomes reveal that the absorber displays three discernible absorption peaks occurring at frequencies 4.06 GHz, 6.73 GHz, and 9.22 GHz. Notably, the absorption rates at these frequencies are 0.99, 0.93, and 0.95, respectively. Importantly, this absorber proves effective across a broad spectrum of incident angles for both transverse electric (TE) and transverse magnetic (TM) polarizations. Zhu et al. [90] also reported the similar metamaterial absorber. The metamaterial's unit cell is designed

with a four-fold rotational symmetric electric resonator and a cross structure printed on each side of a printed circuit board. This configuration is engineered to achieve dual resonances, both electric and magnetic, in the metamaterial. Experimental verification confirms that the absorption characteristics of this particular metamaterial absorber consistently exceed 90%. This high absorption performance is observed across a wide incident angle range spanning from 0° to 60° for both TE and TM modes. With similar mechanism, Ding et al. [14] developed the metamaterial absorber composed by pyramid shape unit cell of alternated layers of conductive and FR4 dielectric. This results in continuous multi-resonance response due to the corresponding to the different sizes of resonators on the tapered shape of pyramid. Absorption above 90% was achieved for ultra-wideband from 7.8-14.7 GHz due to the continuous resonance peaks. Furthermore, the absorber geometries of all mentioned works were investigated via EM field computational model. This hybrid simulation/experimental approach allows opportunities for exploration of novel absorbing structure. Ma et al. [92] introduced more complicated structure of composite metamaterial absorber. 2D hexagonal Ti_3CNT_x MXene- based magnetic composites Fe@NC (nitrogen - doped carbon)/Ti3CNTx were fabricated. The absorber exhibits excellent broadband microwave absorption with the BW@10 of 12.5 GHz ranging from 5.5 GHz to 18 GHz at a total thickness of 4.5 mm owing to the multiscale microwave loss mechanism. There are also reported works on polymer nanocomposites metamaterial absorbers [77,93–96]. For example, Zhou et al. [93] reported the 3D printed honeycomb skeleton coated by the conductive coating composed of carbon fibers, carbon nanotubes and resin. 90% absorption in 5.65 ~ 40 GHz with a total thickness of 6 mm were achieved. It can be noted from these works that metamaterial concept not only helps enhance the EM absorption at a certain frequency, but also

meets the requirements of multi-objective operating conditions such as wide frequency bandwidth, polarization independent, and wide angle of incident.

Previously, our group members Bregman et al. [97–99] proposed the ability to investigate the EMI shielding responses of periodic porous structure via EM field-based computational method. The authors aimed to design the geometries of polymer-based composite foams without trial and error on the foaming process using computational based modelling, in order to achieve the desired cellular structures which provides sufficient EMI shielding performance. The model introduced a single layer of periodic cubic and spherical pores in subwavelength size into the plague of a periodic unit cell from Song et al. [21] rGO/Fe_3O_4/wax composite. It was found from the simulation that the composite contained periodic pores not only act like impedance matching elements but also perform as metamaterial absorber. When the geometry, size, and position of the periodic pores meet the certain conditions that induce the interaction between the pores and incidence EM wave, the interior resonance can be excited. Thus, enhanced absorption can be achieved. This periodic porous structure takes advantages not only from impedance matching, internal reflection, and scattering of the air pores, but also the metamaterial behavior of the design. However, the improvement is not monotonic with the pore size, which implies that only certain geometry can be the optimized design to achieve the highest absorption performance. This approach can be extended to more complex structures that can be optimized to attain the desired multi-objectives.

1.7 Dissertation Outlines

From the introduction in this chapter, this dissertation provided opportunities for further exploration of periodic porous structure, and optimization can be taken place to achieve multi-objective design of the EM absorbers. Furthermore, it also proposed the workflow for designing

for the periodic porous structured polymer composite via simulation and experimental method to achieve desired EM absorption.

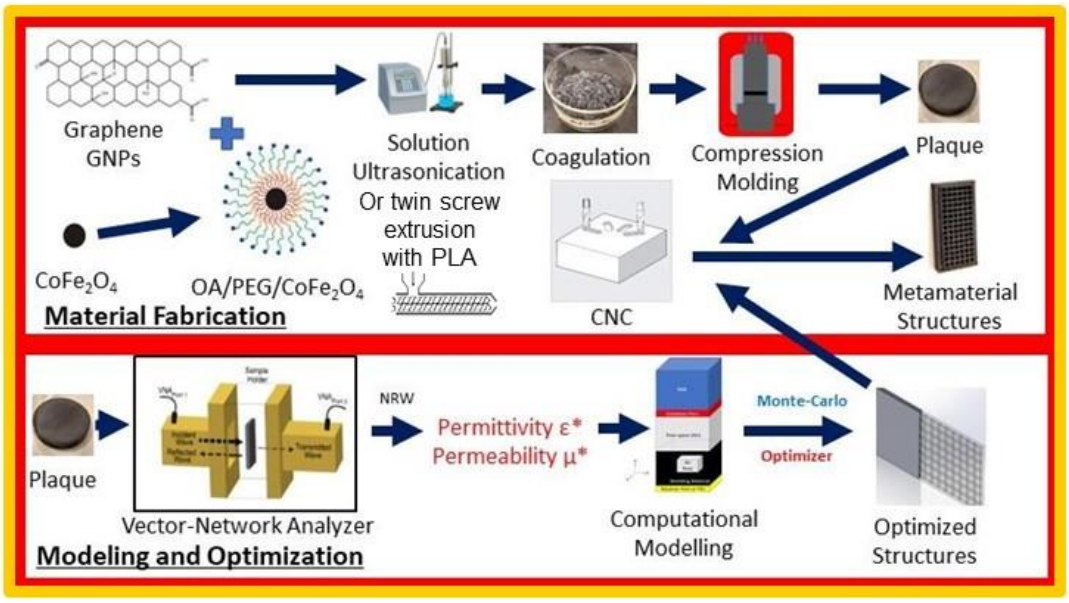

Figure 1-5 The schematic of the strategy for design and optimization periodic porous metamaterial absorber in this research.

Figure 1-5 illustrates the schematic of the strategy for design and optimization periodic porous metamaterial absorber in this research. It can be noted that all processes including material fabrication, material characterizations, computational modelling, optimization, metamaterial production and model validation are sequentially performed. Chapter 2 presents the work according to the objective of design, fabricating, and characterization of polymer composites with the intrinsic properties (ε*, μ*) that provide the commercial/military level of absorptions in term of maximum RL as baseline materials. The polymer composites consisting of GNPs and $CoFe_2O_4$ were processed, and their EM intrinsic properties were characterized. Chapter 3 is related to construction and validation of EM field-based computational models, based on the intrinsic properties from chapter 2, to predict the EM absorption in term of the Reflection Loss (RL) of the designed periodic porous metamaterial structures and apply the optimizer to select the most efficient geometries for multi-objective function (max RL and wide

BW). Chapter 4 illustrates the next step of fabrication of the optimized geometries of periodic porous metamaterial absorber with the designed polymer composites. Finally, the summary of the contributions of this dissertation and the future work are proposed in Chapter 5.

Chapter 2 Polymer Composites Electromagnetic Absorbers

2.1 Related Publications

1. Kanat Anurakparadorn, Alan Taub EM. Dispersion of Cobalt Ferrite Functionalized Graphene Nanoplatelets in PLA for EMI Shielding Applications. Proceedings of the American Society of Composite the 36th technical conference, Virtual Conference, Texas A&M University, College Station, Texas, USA: 2021, p. 2163–92.

2. Anurakparadorn Kanat, Taub Alan. A Comparative Study of the Effect of Compounding Methods and Processing of PLA/GNPs on the Micromorphology and Electrical Conductivity. Proceedings of the American Society of Composite the 38th Technical Conference, Boston, MA, USA 2023.

2.2 Introduction

To design periodic porous metamaterial absorbers, it is essential to have the intrinsic properties of the baseline materials as inputs for computational modeling before introducing any meta-structures. As highlighted in Chapter 1, polymer composites, comprising conductive and magnetic constituents, offer the flexibility to be customized to attain the desired electrical permittivity (ε^*) and magnetic permeability (μ^*). This customization involves manipulating factors such as concentration, micromorphology, and dispersion quality of each constituent within the composite materials.

Graphene, a two-dimensional (2D) sheet composed of sp^2-bonded carbon atoms in a honeycombed structure, has attracted considerable attention as a promising conductive filler for

polymer-based electromagnetic (EM) absorbers [46,54,63,64,100–120]. In a study conducted by Bhattacharya et al. [121], the reflection loss (RL) of graphene and multi-walled carbon nanotubes (MWCNTs) in a thermoplastic polyurethane (TPU) matrix was compared. The graphene-based composite exhibited a maximum RL of -12.56 dB at 10.43 GHz, outperforming the -7.6 dB RL of MWCNT-based composites at 10.73 GHz. Despite both composites displaying RL peaks at a similar frequency, graphene demonstrated a superior ability to absorb electromagnetic waves. Additionally, graphene-based materials are more cost-effective and environmentally friendly compared to carbon nanotubes (CNTs). The advantages of graphene-based materials are also attributed to their lightweight nature, corrosion resistance, high electrical conductivity, large specific surface area, and high carrier mobility [122–124].

Pristine graphene possesses many desirable characteristics; however, its poor dispersion, stemming from its smooth and chemically inert surface, hinders interfacial interaction, leading to reduced electrical conductivity and consequently, diminished electromagnetic (EM) absorption performance [125]. The introduction of matrix-compatible functional groups through chemical modification can enhance graphene dispersion [111,126].

Reduced graphene oxide (rGO) is a straightforward method for functionalizing graphene by incorporating carboxylic (-OOH) and hydroxyl (-OH) groups on the surface. Wang et al. achieved a high reflection loss (RL) of -36.4 dB at 4.5 GHz for a 3.5 wt% loading of rGO in poly(vinyl alcohol) (PVA) [56]. The improved absorption was attributed to the molecular-level dispersion quality enhanced by hydrogen bonding between rGO and PVA. These functional groups serve as polarization centers, augmenting polarization loss. Similarly, Bai et al. developed an rGO/poly(ethylene oxide) (PEO) composite [127], emphasizing the enhanced dispersion due to hydrogen bonding between rGO and PEO, alongside dielectric relaxation and scattering at the

fillers/matrix interface. However, the preparation of rGO involves the transition of nonconductive graphene oxide (GO) to conductive rGO through chemical reduction and high-temperature thermal treatment [21,128–130]. This process results in weight loss, morphological changes, phase transitions, and other concerns that can affect EM absorption [21]. Incomplete reduction and defects from the process can lead to lower electrical conductivity than the original pristine graphene [131].

Alternatively, graphene nanoplatelets (GNPs) introduce less residue out-of-plane functional groups. This choice of material helps avoid the defects that can deteriorate conductivity, a concern presents in reduced graphene oxide (rGO). While maintaining dispersion quality, GNPs are more suitable than pristine graphene, offering a balance between improved properties and minimized drawbacks. Our previous work has proven that the composites consist of GNPs can provide higher EM absorption performance in term of RL and operation bandwidth (BW) than rGO at the same loading [46].

For magnetic constituents in EMI shielding polymer composites, ferromagnetic nanomaterials such as Mn, Ni, Fe, and Co have been widely investigated [62,132–136]. However, utilizing pure metals as magnetic fillers presents challenges like corrosion and poor dispersion in polymer matrices, driving efforts towards alternative magnetic materials. Ferrimagnetic nanoparticles, specifically magnetite (Fe_3O_4) and spinel ferrites (γ-Fe_2O_4, where γ can be Co, Ni, Mn, Zn, etc.), exhibit high saturation magnetization, excellent chemical compatibility with polymers, high mechanical hardness, and significant magnetic loss [137]. These materials have been incorporated with graphene-based conductive fillers to form hybrid structures for electromagnetic (EM) absorbers [26,47,52,54,58,59,64,101,103,120,134,137–147]. Song et al. developed a Fe_3O_4/graphene composite, demonstrating that the electrical permittivity

(ε*) and magnetic permeability (μ*) can be tuned by adjusting the concentration of Fe_3O_4 and graphene nanoplatelets (GNPs). The saturation magnetization of the heterogeneous composite significantly increased, reaching a maximum of 47 emu/g with a 50% concentration of Fe_3O_4 on graphene, as well as providing broader absorption bands than the composites without the magnetic filler. Among ferromagnetic materials, $CoFe_2O_4$ nanocomposites have the advantage of a simple synthesis method at low temperatures without requiring an inert gas [42,43]. Examples of reported EM absorbers fabricated from $CoFe_2O_4$ [46,48,49,58,64,101,139,148–158], indicating opportunities to tune the EM absorption performance by tuning the composition of the nanoparticles with the conductive fillers in the composites.

In order to tailor the magnetic permeability of the composites, high volume fraction of $CoFe_2O_4$ is necessary while risking disturbing the dispersion quality at high concentrations due to the magnetic attraction behavior. Therefore, chemical modification of $CoFe_2O_4$ is needed to overcome the magnetic agglomeration issue. One potential way to improve the dispersion is introducing the coating layer of the stabilizer chemical compound on the nanoparticle. Thus, the dispersion quality can be improved and provide the ability to bed dispersed at high concentrations. One simple method that is widely used and provides acceptable dispersion quality is covalent bonding the surface of the nanoparticle with oleic acid (OA) and polyethylene glycol (PEG) [159,160]. This technique can provide the opportunity to tailor the loading of $CoFe_2O_4$ to extra-high level and achieving the desired EM intrinsic properties.

The literature review reveals that polymer composites, incorporating graphene-based materials and $CoFe_2O_4$, have been deliberately designed, fabricated, characterized, and optimized to achieve the desired EM absorption properties as baseline materials for designing the periodic porous structure metamaterial absorbers. Various graphene materials, including reduced

graphene oxide (rGO) and graphene nanoplatelets (GNPs), were utilized in these composites, allowing for a comparative analysis. The investigation also delved into the impact of incorporating $CoFe_2O_4$ into the composites, exploring different methods to introduce it at high concentrations. This comprehensive study aims to enhance the understanding of the role of graphene-based materials and $CoFe_2O_4$ in achieving effective EM absorption, with the ultimate goal of developing materials suitable for commercial EM absorption applications (targeting a Reflection Loss of -20 dB) [3,5,71].

2.3 Experimental

2.3.1 Materials

M25 grade xGNPs were purchased from XGscience (Michigan, USA). Cobalt nitrate hexahydrate ($Co(NO_3)_2 \cdot 6H_2O$), iron nitrate nanohydrate ($Fe(NO_3)_3 \cdot 9H_2O$), sodium hydroxide (NaOH), methanol, potassium permanganate ($KMnO_4$), hydrogen peroxide (H_2O_2), L-ascorbic acid, ethylene glycol, oleic acid and N,N-Dimethylformamide (DMF) were obtained from Sigma-Aldrich, Inc. (USA). Reagent grade deionized water, sulfuric acid (H_2SO_4), phosphoric acid (H_3PO_4), hydrochloric acid (HCl), and ethanol, were purchased from Thermo Fisher Scientific (USA). Polylactic Acid (PLA) pellets were purchased from 3DXTech (Michigan, USA).

2.3.2 Material Fabrications

Overall fabrication processes are shown in Figure 2.1. The production started with filler preparations including: the synthesizes of the $CoFe_2O_4$, the decoration on graphene-based materials, and the surface modification by OA/PEG. Subsequently, the fillers were mixed with

PLA matrix which followed by compression molding into the plaque samples. The details of each step are listed in this subsection.

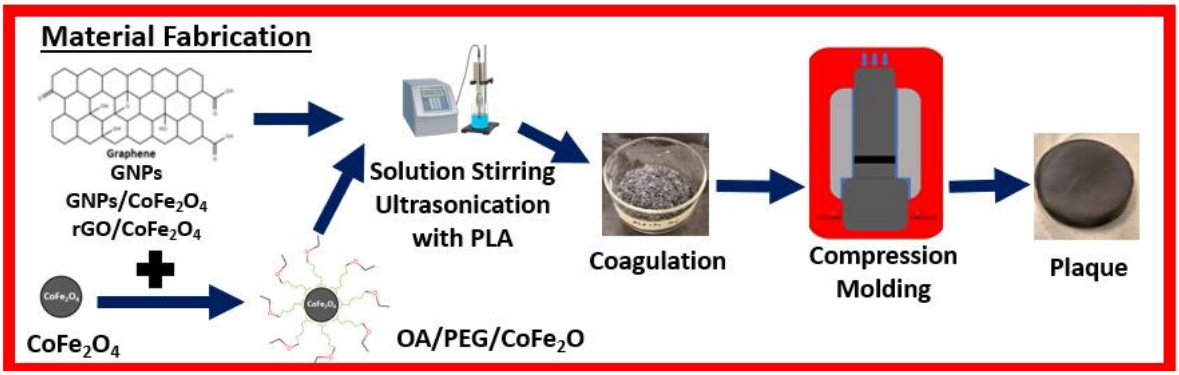

Figure 2-1 Process of design and optimization of PLA/GNPs/COE metamaterial absorbers

2.3.3 Fabrication of rGO

The synthesis of GO was conducted following the improved Hummer's method [161]. GNPs (2g) were added to 1:9 volume ration of H_2SO_4 and H_3PO_4 (26.6 mL:240 mL). The mixture was stirred in an ice bath for 10 minutes before adding $KMnO_4$ (6g) to start the reaction. The mixture was heated up to 50 ºC and maintained for 12 hours. The black mixture turns brown color during the reaction. After cooling down to room temperature, the mixture was poured into ice (800g) and stirred for 10 minutes. H_2O_2 (5mL) was slowly added dropwise to the vigorously stirred mixture until color changes from brown to bright yellow to stop the reaction. The mixture was further stirred for 20 minutes and then centrifuged. The precipitant was washed by centrifuge in sequence of 1 time with water, 1 time with HCl, 2 times with water, and 1 time with ethanol. The supernatant phase was disposed. The brown solid pastes of GO were collected and dried in air-circulated oven at 60 ºC for 12 hours.

Chemical reduction by L-ascorbic acid was chosen as the reduction process. It can take place at relatively lower temperature compared with a thermal reduction process. Furthermore, L-ascorbic acid is non-explosive and less poisonous compared with traditional reduction

chemicals such as hydrazine or hydrazine hydrate [162–164]. Beginning with 400 mL of the GO/water suspension (5 mg/mL, carbon/water) was prepared by ultrasonication until a homogeneous suspension was obtained. The suspension was heated up to 90 ºC. Then, 10 mg/mL of L-ascorbic acid is added to the flask and kept stirring for 60 minutes to perform the reduction The precipitated rGO powder was cooled to room temperature before washed and centrifuged for 10 minutes multiple times in the in methanol until Ph is approximately 7 to removed excess precursors and impurities. The precipitant was collected and dried in an air-convection oven at 80 ^{o}C for 24 hours.

2.3.4 Fabrication of $CoFe_2O_4$

The chemical reaction of $CoFe_2O_4$ synthesis were adapted from Zhao et al. [165]. Briefly, 0.1 mol of $Co(NO_3)_2{\cdot}6H_2O$ (29.1g) and 0.2 mol of $Fe(NO_3)_3{\cdot}9H_2O$ (80.8g) were added to 250 mL of the DI water and heated up to 90 ^{o}C. The solution was stirred for 20 minutes until homogeneous brown solution was obtained. NaOH (35g) was added to raise the pH up to 12 to start the reaction. The reaction was maintained for 4 hours. The black suspension that showed that $CoFe_2O_4$ was observed during the reaction. At the end of the reaction, black solid powders of precipitates can be observed at the bottom of the flask. The precipitant was washed and centrifuged multiple times in the in methanol until Ph is approximately 7 before dried in air-convection oven at 80 ^{o}C for 24 hours.

2.3.5 Fabrication of rGO/$CoFe_2O_4$

Similar to $CoFe_2O_4$, the decoration of the magnetic nanoparticles on rGO surfaces was achieved by co-precipitation in GO suspension before the reduction. The carbon content in prepared GO was characterized by elemental analysis before determining the precursor amount.

$Co(NO_3)_2 \cdot 6H_2O$ and $Fe(NO_3)_3 \cdot 9H_2O$ precursors with 1:2 molar ratio of Co^{2+} : Fe^{3+} were added to 400 mL of the GO/water suspension with the desired ration of $CoFe_2O_4$ product with carbon content in GO (1:1 by weight or 1:1 by volume). The suspension was heated up to 90 ^oC and maintained for 20 minutes before adding NaOH to the flask until pH around 12. The reaction took 2 hours before cooled down to room temperature. The precipitant was washed in the in the same sequence as rGO and dried in convection oven at 80 ^oC for 24 hours.

2.3.6 Fabrication of GNPs/$CoFe_2O_4$

The GNPs/water suspension was prepared in a round-bottom flask by stirring 5mg/mL of GNPs (2g) with water (400mL) for 30 minutes. The decoration of $CoFe_2O_4$ on GNPs was performed in the same method as rGO/$CoFe_2O_4$.

2.3.7 The Treatment of OA/PEG Surfactant on $CoFe_2O_4$

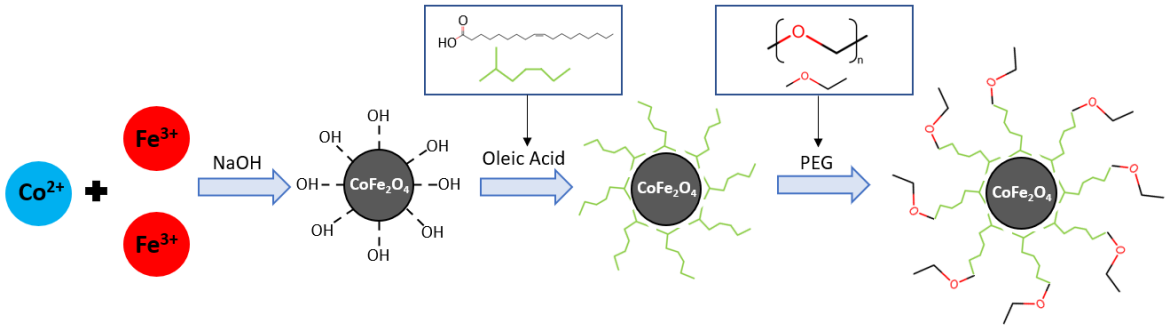

Figure 2-2 Oleic acid/Ethylene glycol surfactant treatment on $CoFe_2O_4$

The polymerization of OA/PEG process is shown in Figure 2.2 The precipitated $CoFe_2O_4$ after washing process was collected and put in the round bottom flask. Thereafter, 150 mL of ethylene glycol and 10 mL of oleic acid were added to the mixture and heated up to 150 ^oC and stirred for 4 hours. Afterward, the mixtures were washed with methanol until the Ph of the supernatant is approximately 7 to remove access oleic acid and ethylene glycol. The precipitants were collected and dried in the convection oven at 60 ^oC for 12 hours.

2.3.8 Composite Processing

2.3.8.1 Solution Mixing

The PLA composites were prepared by the solution mixing and coagulation method [166]. The overall weight of the materials in each mixing batch is set constant at 10g. The blending was started by dissolving PLA pellets in 100 mL of DMF via mechanical stirring at 60 ^{o}C. In the meantime, the measured loading of $CoFe_2O_4$ was dispersed in 250 mL of DMF via tip ultrasonication with the total energy transferred to the system around 250 kJ. The result suspension was black without residue $CoFe_2O_4$ chunks settling on the bottom of the beaker. The decided loading of GNPs was added to the suspension and further ultrasonicated for 150 kJ. Afterwards, the suspension was poured into the prepared PLA solution and stirred at room temperature for 12 hours. PLA/GNPs/$CoFe_2O_4$ suspension was further ultrasonicated for 170 kJ. The composite suspension was coagulated in 1200 mL of methanol before filtered. The solid filtered cake was dried in the vacuum oven at 65 ^{o}C for 48 hours. The dried composite was ground into powders and compression molded at 170 ^{o}C 2.5 MPa in vacuum hot press. The resulting composite plaques were cut into 22.9 mm x 10.1 mm x 5 mm cuboid samples for characterization.

2.3.8.2 Twin Screw Extrusion Compounding

The compounding was process under the twin screw extruder (Leistritz MIC27/GL-480). PLA pellets were fed from the hopper into the extruder at the rate of 183 g/min. In the meantime, GNPs powders were fed into another hopper at the rate of 9.63 ,14.85, and 19.26 g/min providing the mixing at the concentration of 5wt%, 7.5wt%, and 10wt%, respectively. The screw chamber is divided into 8 stages. The temperature was set to 160 ^{o}C and 170 ^{o}C at the first and the second stages, respectively. The rest of the stage and the extrusion die was set to 180 ^{o}C. The

screw speed was set to make the melt pressure at 1 MPa with the side stuffer speed of 1000 RPM. The extruded strands were chopped into the pellet with Scheer Bay pelletizer with the length around 5 mm and the diameter around 2 mm. Consequently, the pellets were ground into powders under liquid nitrogen and compression molded at 170 ^{o}C 2.5 MPa in vacuum hot press. The resulting composite plaques were cut into 22.9 mm x 10.1 mm x 5 mm cuboid samples for characterization.

2.4 Characterization

Surface morphologies and elemental analysis by energy-dispersive X-ray spectroscopy (EDX) spectrum were characterized by Joel IT500 scanning electron microscopy (SEM). Fourier transform infrared spectroscopy (FTIR) spectra were measured from JASCO 4100. The crystallographic properties were characterized by X-ray diffraction spectra that was performed in Rigaku Miniflex XRD. Magnetizations hysteresis loops were obtained from LakeShore 7404 vibrating sample magnetometer (VSM). The volumetric DC electrical conductivity was determined using a two-points probe resistance technique for through-thickness analysis of rectangular samples with 5V supplies from Keithley multimeter. The sample surfaces were covered with silver paint to ensure full electrical contact and to perform the average measurement across the entire surface. A constant voltage of 5V was applied on both surfaces and the resistance was measured. The conductivity (σ) was calculated from

$$\sigma = \frac{t}{lwR} \tag{2.1}$$

while t is the thickness of the sample, l is the length of the sample, w is the width of the sample, and R is the measured resistance across the thickness.

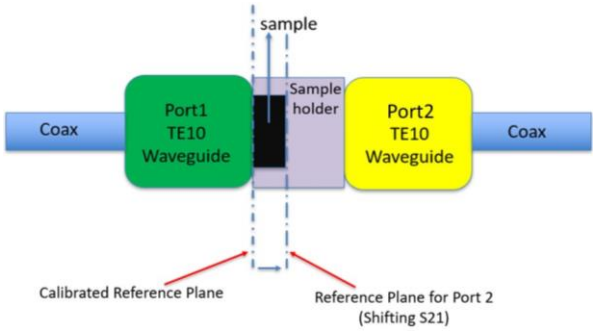

Figure 2-3 Schematic of the setup of vector network analyzer characterization with WR90 waveguide

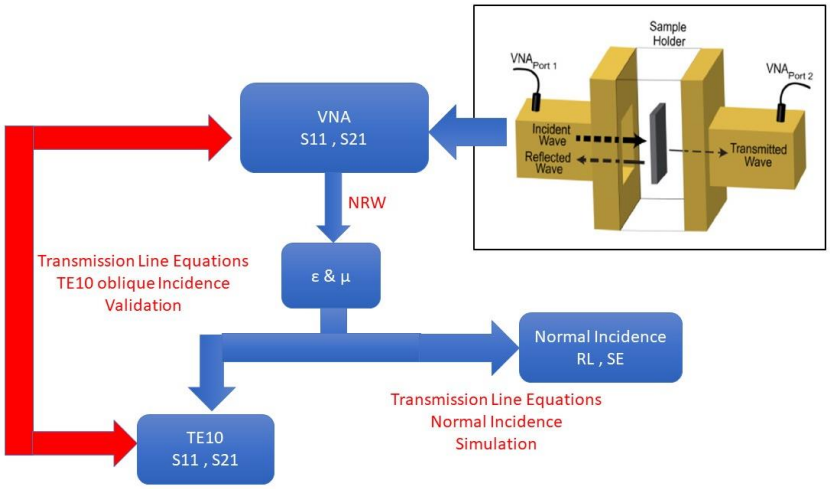

Figure 2-4 Process of Scattering parameters characterization, model validation, and RL/SE determination

Electromagnetic properties characterization process is shown in figure 2.3 and figure 2.4. The process was started by the measurement of scattering parameters S11 and S21 which was performed in the Anritsu vector network analyzer (VNA) (figure 2.3). The samples were placed in the WR90 waveguide which provides TE10 mode of angle of incidence for the EM wave propagating between port 1 and port 2 of the VNA [167]. Material intrinsic properties, including complex electrical permittivity (ε^*) and magnetic permeability (μ^*), were extracted from the measured S11 and S21 using Nicholsen-Ross-Weir (NRW) method [168,169]. The extracted intrinsic properties were input into transmission line equations [19,170,171] to simulate the reflection coefficient (Γ) and transmission coefficient (τ) of the material slab in different conditions and modes of propagation.

To validate the extracted material intrinsic properties, complex electrical permittivity (ε^*) and magnetic permeability (μ^*) were input in the set of transmission line equations to back calculate the S11 and S21 and compared with the measurement values.

Finally, the electromagnetic absorption of the fabricated composites can be determined from the reflection loss (RL). The extracted intrinsic properties (ε^*, μ^*) were input in the transmission line equation with PEC load and determined the RL from equation 1.9.

2.5 Results and Discussion

2.5.1 Solution Mixing Composites Characterizations

Each composite system exhibits distinct characteristics that can impact properties related to electromagnetic absorption. Unlike pristine GNPs, rGO undergoes multiple processing steps involving oxidation and reduction. It contains more out-of-plane functional groups that can affect its morphology. Additionally, the presence of residual oxide groups from the reduction process can lead to variations in dispersion quality within the composite. The inclusion of CoFe2O4 magnetic nanoparticles, due to their magnetic properties, further distinguishes composites containing only graphene-based materials (rGO, GNPs). Furthermore, differences in the density and electrical conductivity of each constituent contribute to distinctions in the electrical properties among these composite systems.

The presence of oxide groups on the rGO can also affect the CoFe2O4 decoration process when compared to pristine GNPs. Moreover, CoFe2O4 possesses significantly higher density (5.4 g/cm3) compared to graphene (2.2 g/cm3) and PLA (1.2 g/cm3). To tailor the magnetic properties without affecting conductivity, a larger amount of CoFe2O4 is required to increase the volume fraction of magnetic nanoparticles. As a result, the decoration technique may not be applicable, and the magnetic nanoparticles need to be dispersed separately with the conductive

constituent. To disperse high concentrations of magnetic nanoparticles, the use of OA/PEG surfactants was introduced to prevent magnetic agglomeration. Furthermore, a lack of interaction between graphene-based materials (GNPs, rGO) and CoFe2O4 can also influence the morphology of the composite, which in turn affects the electromagnetic properties.

Table 2.2-1 The nomenclatures and compositions of each fabricated sample

Samples	**wt% GNPs**	**wt% rGO**	**wt% $CoFe_2O_4$**
PLA	-	-	-
Effect of rGO			
5rGO	-	5	-
8rGO	-	8	-
Effect of $CoFe_2O_4$ decorated on rGO			
10rGOCw	-	5	5
15rGOCw	-	7.5	7.5
25rGOC	-	7.5	17.5
Effect of GNPs			
5GN	5	-	-
Effect of $CoFe_2O_4$ decorated on GNPs			
10GC	3	-	7
16.70GC	5	-	11.7
18GC	5.4	-	12.6
20GC	6	-	14
25GC	7.5	-	17.5
33.33GC	10	-	23.33
Effect of GNPs + COE			
2.5GN40COE4	2.5	-	40
2.5GN50COE4	2.5	-	50
3GN40COE4	3	-	40
3GN50COE4	3	-	50
3.5GN40COE4	3.5	-	40
3.5GN50COE4	3.5	-	50

This study was aimed to compare the effect of different kinds of composite systems and their loadings on the properties related to electromagnetic absorption. Table 2.1 shows the loading and fillers used in this study. The nomenclatures start by the loading in wt% and filler type including rGO, $CoFe_2O_4$ decorated on rGO (rGOC), GNPs (GN), $CoFe_2O_4$ decorated on GNPs (GC), and GNPs dispersed separately with OE/PEG treated CoF_2O_4 (GNCOE).

2.5.1.1 Dispersion of CoFe2O4

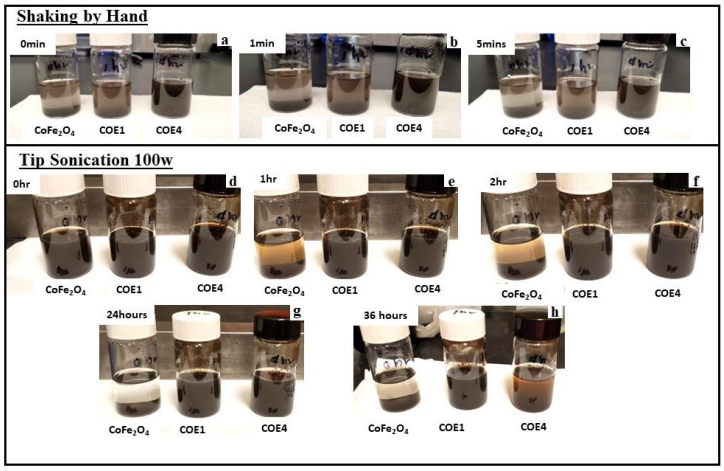

Figure 2-5 The dispersion stability test of $CoFe_2O_4$, COE1, and COE4 by hand shaking and left undisturbed for a. 0 min, b. 1 min, and c. 5 mins, and by 100w Tip sonication and left undisturbed for d. 0 hour, e. 1 hour, f. 2 hours, g. 24 hours, and h. 36 hours

The effect of the OA/PEG treatment on the $CoFe_2O_4$ dispersibility in the matrix were tested by mixing neat $CoFe_2O_4$, COE1, and COE4 in DMF. It can be assumed that the dispersibility of the nanoparticles in DMF is similar to the dispersibility of PLA/DMF solutions. Figure 2.5a – 2.5c shows the suspension of $CoFe_2O_4$/DMF, COE1/DMF, and COE4/DMF after shaking by a hand for 1 minute and left unattended for 0 minutes, 1 minute, and 5 minutes, respectively. Obvious sedimentation can be observed for $CoFe_2O_4$/DMF immediately after shaking, while COE1 started settling down to the bottom of the container after 1 minute. Only COE4/DMF suspension can maintain the homogeneity after being left unattended for 5 minutes. The investigation was further performed by dispersing the magnetic nanoparticles in DMF using ultrasonication at the power of 100 W for 1 minute. The observation took place after the suspensions were left undisturbed for 0 hours, 1 hour, 2 hours, 24 hours, and 36 hours, respectively. Homogeneous phases were obtained for all suspension of the ultrasonication. The neat $CoFe_2O_4$ started to precipitate after being left unattended for 1 hour. After 24 hours, neat $CoFe_2O_4$ nanoparticles completely sedimented to the bottom of the vile, while COE1 and COE4

still maintain the stability until 36 hours. This experiment shows that coating OA/PEG on $CoFe_2O_4$ helps increase the dispersibility in DMF and PLA matrix. The OA molecules may act as a surfactant while the presence of PEG can also contribute to the formation of a protective layer around the nanoparticles. This coating can help to prevent aggregation of the nanoparticles, thereby stabilizing them in solution [159,172–174].

2.5.1.2 Fourier Transform Infrared Spectroscopy Spectra (FTIR)

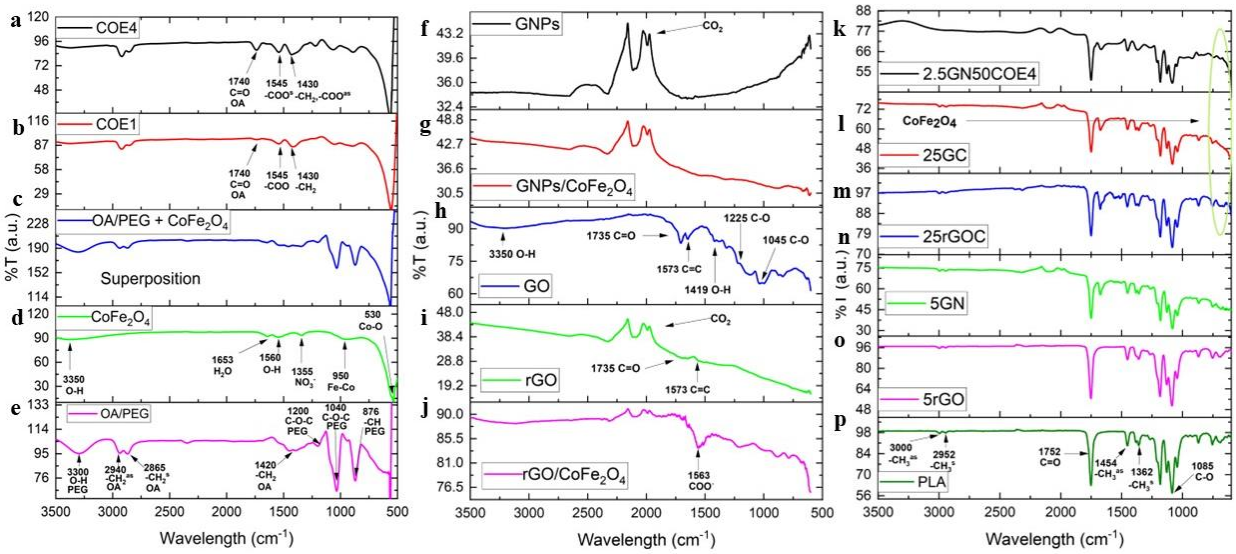

Figure 2-6 FTIR spectra of a. COE4 b. COE1 c. Superposition of the $CoFe_2O_4$ and OA/PEG spectra d. $CoFe_2O_4$ e. OA/PEG f. GNPs g. GNPs/ CoFe2O4 h. GO i. rGO j. rGO/ $CoFe_2O_4$ k. 2.5GN50COE4 l. 25GC m.25rGOC n. 5GN o. 5rGO p. PLA

Figure 2.6 shows the transmission FTIR spectra of the fabricated composites and their constituents. Figure 2.6a – 2.6e represents the spectra of 4 hours treated COE (COE4), 1 hour treated COE (COE1), the superposition of $CoFe_2O_4$ and OA/PEG, $CoFe_2O_4$, and OA/PEG respectively. For OA/PEG (figure 2.6e), the plot shows the combination of the characteristic peaks of both OA and PEG. The characteristic peaks are matched with the reported work [159,173]. The peak at 3300 cm^{-1} and 876 cm^{-1} are attributed to the O-H stretching vibration and out-plane -CH bending of the PEG chain. The peak at 1200 cm^{-1} and 1040 cm^{-1} are assigned to the asymmetric and symmetric stretching C-O-C in PEG. The peaks of -CH

asymmetric/symmetric stretching of OA can be observed at 2940 cm^{-1} and 2865 cm^{-1} band, respectively. The peak at 1455 cm^{-1} can be attributed to the bending vibrations of the hydrophobic chain in OA. Figure 2.6d displays the FTIR spectrum of the synthesized $CoFe_2O_4$. The peak around 530 cm-1 is attributed to the stretching vibrations of Co-O, a characteristic feature observed in spinel ferrite materials. The band at approximately 950 cm-1 corresponds to the Fe-Co alloy system [149,152,175]. The peak at 1355 cm-1 is associated with the symmetric vibration of the residual NO_3^- ions from the precursors. Additionally, the peaks at 1560 and 3350 cm-1 are assigned to O-H stretching vibrations. The presence of the peak at 1653 cm-1 can be attributed to the bending of absorbed water molecules[152,176,177]. These characteristic peaks align with existing reports in the literature [149,152,175–178]. Figure 2.6c is the superposition of spectra from figure 2.6d and figure 2.6e for comparison with the spectra of the OA/PEG treated $CoFe_2O_4$ in figure 2.6a - 2.6b. It can be observed that there are additional peaks representing bonds from the interaction between $CoFe_2O_4$ and OA/PEG in COE1 and COE4 spectra. The peaks of COO^- asymmetric/symmetric stretching vibration can be observed at 1455 cm^{-1} and 1405 cm^{-1}. This carboxyl group exists when the OA has a chemical interaction with $CoFe_2O_4$ nanoparticles [173]. The C = O asymmetric vibration band at 1740 cm^{-1} is attributed to the hydrophilic carboxyl group on OA [173]. It can be observed that the intensity of this peak is higher for COE4 compared with COE1 due to the longer reaction time. The absence of this peak in Figure 2.5e can be explained by the fact that the sample was a liquid mixture of oleic acid (OA) and an excess amount of polyethylene glycol (PEG), as described in section 2.2.5. Consequently, the transmission IR signal of OA may have been overshadowed by the signal from PEG in the mixture.

Figure 2.6f – 2.6j represents the FTIR spectra of graphene-based fillers that were used in this work. No significant characteristic peak can be observed from the neat GNPs spectrum (figure 2.6f) due to the low amount of out-plane functional chemical content. The existence of the peak around 2300 cm^{-1} can possibly be reasoned by the absorption of CO_2 from the environment by the graphene [179]. It can be noticed in GNPs/$CoFe_2O_4$ spectrum (figure 2.6g) that the amount of transmission decreases from the GNPs spectrum in the band around 500 – 1000 cm^{-1}. This is influenced by the presence of $CoFe_2O_4$ which has a very deep peak of Co-O at 530 cm^{-1}. However, other characteristic peaks of $CoFe_2O_4$ were dominated by GNPs spectrum. This is due to a significant lower volume fraction of the magnetic nanoparticles that were distributed non-uniformly on the GNPs surface. Hence, more surface of GNPs was revealed to the IR signal. Figure 2.6h is the FTIR spectrum of GO. There are characteristic peaks due to out-plane functional groups which agree with the existing works [46,180–183]. The bump around 3350 cm^{-1} and the peak at 1419 cm^{-1} represent the O-H stretching vibration and bending from the oxidation, respectively. The peak at 1735 cm^{-1} is assigned to the carboxyl C=O stretching of the carboxylic acid and/or carbonyl moieties. The peak at 1573 cm^{-1} is attributed to the aromatic C=C group. Two characteristic peaks at 1255 cm^{-1} and 1045 cm^{-1} are assigned to the C-O stretching vibration. It can be observed from the spectrum of rGO (figure 2.6i) that most of the functional groups were reduced. However, the peaks around 600 cm^{-1} – 2000 cm^{-1} suggest that there are remaining out-plane chemical contents after the reduction. After the decoration of $CoFe_2O_4$, the spectrum of rGO/ $CoFe_2O_4$ represents the combination of the characteristic peaks of rGO and $CoFe_2O_4$. Nevertheless, the C=O stretching peak of rGO at 1570 cm^{-1} shifts to 1570 cm^{-1} due to the formation COO^- group [184]

Figure 2.6k – 2.6o shows the FTIR spectra of all composite systems in this work. The characteristic peaks of the composite were mostly dominated by the characteristic peaks of PLA which is shown in Figure 2.6p. The peaks at 3000, 2952, 1762, and 1085 cm^{-1} are assigned the C-O stretching, C=O stretching, C-H stretching, $-CH_3$ symmetric stretching, and $-CH_3$ asymmetric stretching, respectively. The dump of the characteristic peaks around 500-600 cm^{-1} of the composites that contain $CoFe_2O_4$ (Figures 2.6k – 2.6m) indicate the influence of sharp peak of Co-O stretching vibration from the magnetic nanoparticles.

2.5.1.3 X-ray Diffraction Microscopy Spectra (XRD)

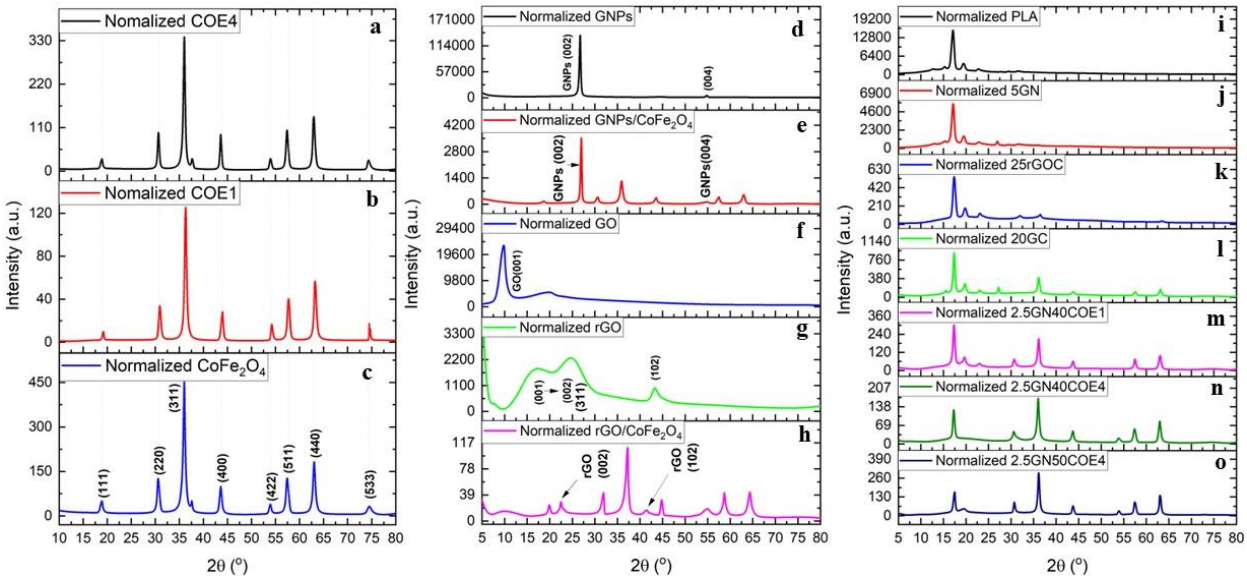

Figure 2-7 Weight normalized XRD spectra of a. COE4 b. COE1 c. $CoFe_2O_4$ d. GNPs e. GNPs/$CoFe_2O_4$ f. GO g. rGO h. rGO/$CoFe_2O_4$ i. PLA j. 5GN k. 25rGOC l. 20GC m. 2.5GN40COE1 n. 2.5GN40COE4 o. 2.5GN50COE4

The weight normalized XRD spectra of the magnetic nano particles COE4, COE1 and neat $CoFe_2O_4$ are shown in figures 2.7a – 2.7c. The characteristic peaks of $CoFe_2O_4$ at 18.79º, 30.61º, 35.99º, 43.55º, 53.91º, 57.41º, 63.13º, and 74.53º are assigned to (111), (220), (311), (400), (422), (511), (440), and (533) crystallographic planes, respectively [148,150,185]. The characteristic peaks of the OA/PET treated $CoFe_2O_4$ match with the original peaks of $CoFe_2O_4$. The peak intensity decreases from neat $CoFe_2O_4$ to COE1 and increases again to COE4. This can

be attributed to the variability of the crystallite size due to the effect of the OA/PET coating which matched with the reported works [160,173,174].

The weight normalized XRD spectra of the conductive fillers are presented in the figure 2.7d – 2.7h. The (002) plane of graphitic peak at 2θ around 26.67° and (004) plane at 54.75° are shown in GNPs spectrum (figure 2.7d) [150,186,187]. Figure 2.7e shows the combination of the characteristic peaks of heterogeneous hybrid materials of $CoFe_2O_4$ and GNPs due to the decoration, and no second phases were detected. For GO spectrum, the broader (002) graphitic peak is fully shifted to (001) plane around 9.19^o (figure 2.7e). After the reduction, the (001) peak is shifted back toward (002) graphitic plane. This indicates that functionalities and the restoration of C=C bonds [186,188] which is resulted by removal of oxygen which leads to the lower parallel stacking of rGO sheets than GO [186]. The small diffraction peak at 43.67° is contributed to (102) plane of rGO structure [189]. The residue of out-plane functional group broadens the peak as a result of the combination of (001) and (002) peaks.

Figure 2.7i -2.7o illustrate the XRD spectra of the neat PLA and the fabricated composites in different methods. The characteristic peaks of semi-crystalline PLA can be observed at 16.81° and 19.11°, 22.77° which are similar with the existing reports for α form of PLA [190–192]. The spectra of all composite systems show the combination of the characteristics peaks of each constituent with matching position of 2θ. It can be noticed that the intensity of the $CoFe_2O_4$ peaks in 2.5GN50COE is higher than the peaks in 2.5GN40COE due to more volume fraction of the COE nanoparticles which increase the crystallinity of the composite.

2.5.1.4 Morphology via Scanning Electron Microscopy (SEM)

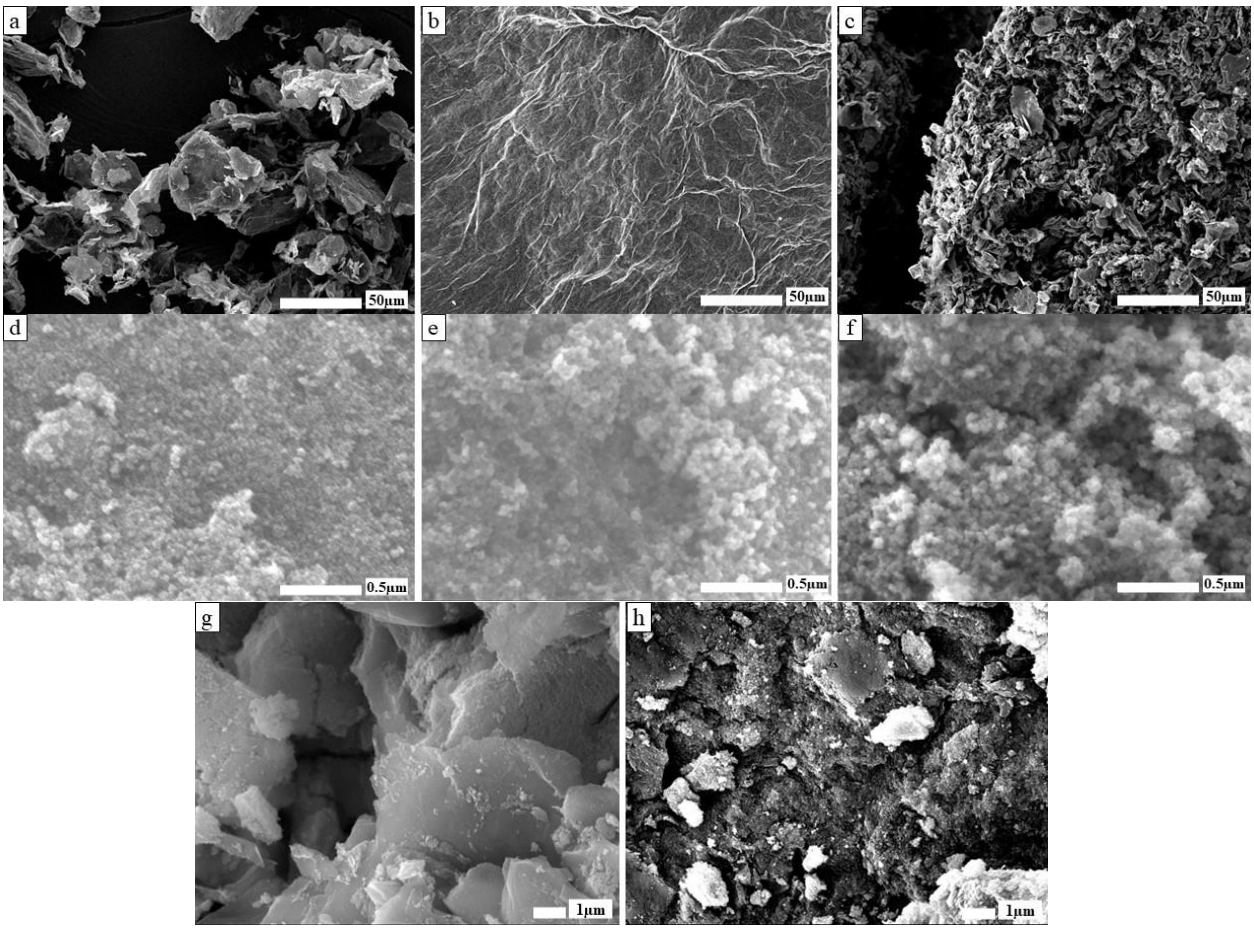

Figure 2-8 SEM images of a. GNPs b. GO c. rGO d. $CoFe_2O_4$ e. COE1 f. COE4 g. GNPs/$CoFe_2O_4$ h. rGO/$CoFe_2O_4$

The SEM micrographs of graphene-based fillers of the composites are illustrated in figure 2.8a-2.8h. From figure 2.8a, the original size of GNPs is approximately around 23 -27 µm, which is matched with the specification provided by the vendor [193]. After the oxidation, the GO sheets agglomerated together due to the introduction of sp^3 hybridized carbon atoms within the GO structure that were caused by the functional groups such as carboxylic (-OOH) group, hydroxyl (-OH) group, and epoxy group (-O-) between graphene surfaces [180]. Figure 2.8c shows the morphology of rGO after the reduction. The approximate diameter of rGO is around 2-5 µm. The oxidation process can introduce defects on the GNPs surfaces by changing the bonding structure in the aromatic ring due to the presence of the functional groups [194]. After

the side groups were removed, the defects remain, which results in the decrease in fracture toughness of the graphitic plane [194–196] Thus, they were easily torn up during the ultrasonication in the reduction process [46].

Figure 2.8d represents the morphologies of $CoFe_2O_4$ nanoparticles, while figure 2.8e – 2.8f shows the morphology of COE1 and COE4, respectively. After the functionalization with OA and PEG for 1 hour, the diameter of CoFe2O4 increased from 28.0 nm ±5 nm to 37 nm ± 8 nm. The final size after the reaction progressed to 4 hours is 42 nm ±12 nm. The size increase observed over time is due to the coating of OA/PEG on the surface of the nanoparticles [159,173,174,197,198]. As the reaction progresses, the OA and PEG molecules continue to attach to the nanoparticles, forming a stable coating. The continued adsorption of molecules on the nanoparticle surface and the formation of a protective layer can lead to a further increase in the effective size of the nanoparticles [159].

Figure 2.8g – 2.8h compare the surface morphologies of GNPs/$CoFe_2O_4$ and rGO/$CoFe_2O_4$. It can be observed that the complete coating of the nanoparticles on the rGO surfaces, while GNPs surfaces are revealed by the non-uniform distribution of the $CoFe_2O_4$ nanoparticles. Similar morphology can be found in Song et al.'s GNPs/Fe_2O_3 [21]. $CoFe_2O_4$ nanoparticles can chemically interact with rGO through the formation of chemical bonds. The out-of-plane functional groups on graphene-based materials serve as anchoring sites for the nanoparticles and can affect their distribution on the graphene surfaces [101,199]. Thus, the presence of these functional groups on the rGO which helps prevent the aggregation of $CoFe_2O_4$ due to the dipolar interaction [200]. Moreover, more interaction between $CoFe_2O_4$ and graphene materials leads to less aggregation of $CoFe_2O_4$ during crystal formation in the synthesis reaction [185,201]. This resulted in the reduction of $CoFe_2O_4$ diameter [46].The diameter of the

nanoparticles on rGO is 17.4 ± 4.3 nm while it is maintained the original size of 30.4 ± 4.3 nm on GNPs. It can also be noted that the original size of GNPs was preserved after $CoFe_2O_4$ addition. This indicates that the decoration process of CoFe2O4 does not affect the intermolecular structure of the GNPs and confirms that the GNPs were not deteriorated by the reduction process which matches with our previous report [46].

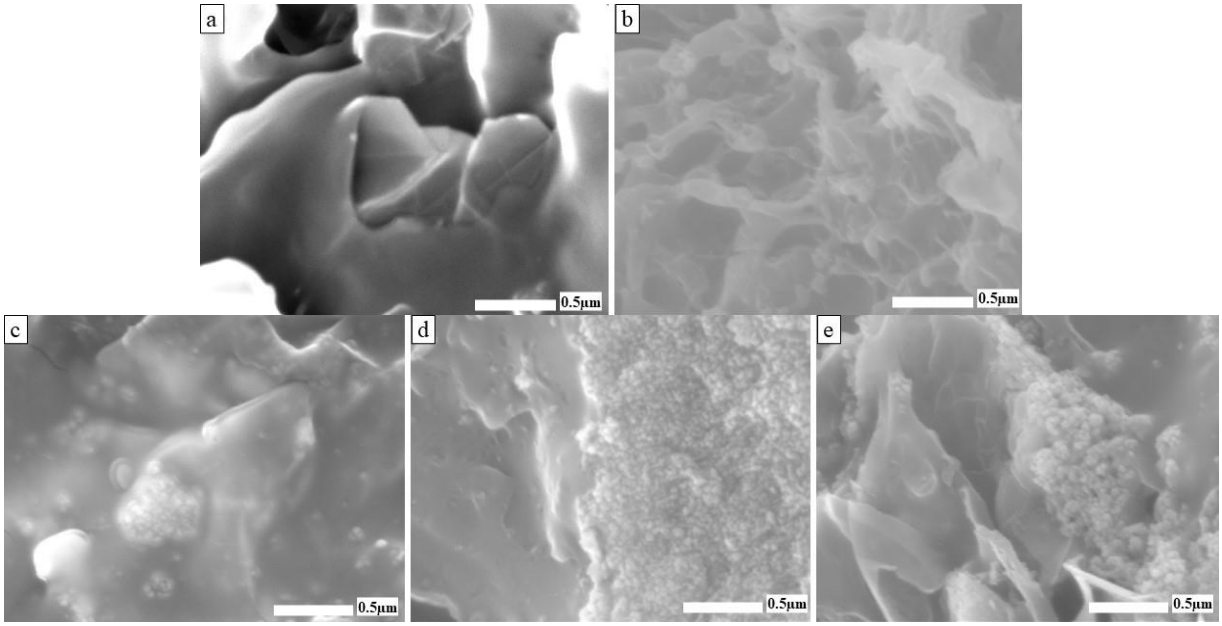

Figure 2-9 SEM images of the cryogenic fracture surface of a. 5GN b. 5rGO c. 20GC d. 25rGOC e. 2.5GN50COE

Figure 2.9a – 2.9e illustrate the SEM images of the cryogenic fracture surface of the composites. Comparing Figure 2.9a and 2.9b, composite containing GNPs exhibits a morphology with larger plate-like particle sizes when compared to the composite incorporating rGO. This size difference can be attributed to the individual sizes of each filler, as previously discussed. The distinction in the distribution of $CoFe_2O_4$ nanoparticles in the GNPs composite and rGO composite also aligns with the characteristics of the respective fillers used. For Figure 2.9e, The COE nanoparticles tend to agglomerate with each other, but they are separate from the GNPs composite plane. This is the result of separately dispersing the GNPs and COE nanoparticles,

without employing a co-precipitation reaction process. Therefore, there is no interaction between the nanoparticles and GNPs.

2.5.1.5 Elemental Analysis via Energy-Dispersive X-ray Spectroscopy EDS

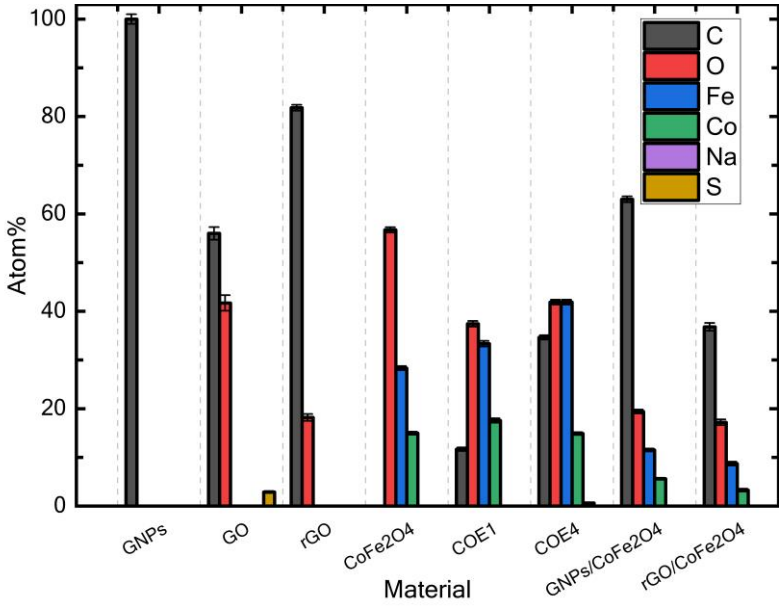

Figure 2-10 EDS analyzed the atomic percentages of each element in the fabricate filler materials for the composites.

The elemental analysis of each constituent element within the fabricated filler materials was carried out through the energy-dispersive X-ray spectroscopy (EDS). The atomic percentages pertaining to these elements are visually represented in Figure 2.10 and comprehensively tabulated in Table 2.2. The initial GNPs consist solely of carbon atoms, accounting for 100% of the elemental composition. Subsequent to the oxidation process, the introduction of oxygen functional groups alters the atom ratio, resulting in a carbon-to-oxygen (C:O) ratio of 1:0.8 in GO. It can be noticed that there is a minor residue impurity of the sulfur (S) content from the reaction which can be eliminated during the reduction process. Subsequent to the reduction process, the removal of oxygen functional groups leads to a decrease in the oxygen content, resulting in a C:O ratio of 1:0.2 in rGO.

Table 2.2-2 Mass percentage and atom percentage of each element in the fabricated fillers obtained from EDS elemental analysis.

Material	Element	Atom%	Ratio
GNPs	C	100 ± 1.0	-
GO	C	56.0 ± 1.3	C:O 1:0.8
	O	41.7 ± 1.6	
	S	2.87 ± 0.2	
rGO	C	81.8 ± 0.6	C:O 1:0.2
	O	18.2 ± 0.7	
$CoFe_2O_4$	O	56.71 ± 0.55	Co:Fe 1:1.9
	Fe	28.33 ± 0.41	
	Co	14.96 ± 0.32	
COE1	C	11.67 ± 0.36	Co:Fe 1:1.9 Co,Fe:C 1:0.2
	O	37.43 ± 0.58	
	Fe	33.34 ± 0.57	
	Co	17.57 ± 0.46	
COE4	C	34.63 ± 0.44	Co:Fe 1:1.7 Co,Fe:C 1:1.5
	O	41.87 ± 0.51	
	Fe	14.88 ± 0.29	
	Co	8.61 ± 0.24	
$GNPs/CoFe_2O_4$ 1:1 by mass	C	63.0 ± 0.6	Atom Ratio Co:Fe 1:2.0 Co,Fe:C 1:3.7
	O	19.4 ± 0.4	
	Fe	11.5 ± 0.3	
	Co	5.6 ± 0.2	
	Na	0.63 ± 0.1	
$rGO/CoFe_2O_4$ 1:1 by mass	C	36.8 ± 0.8	Atom Ratio Co:Fe 1:2.0 Co,Fe:C 1:1.4
	O	34.1 ± 0.8	
	Fe	17.2 ± 0.6	
	Co	8.7 ± 0.4	
	Na	3.25 ± 0.3	

The synthesized $CoFe_2O_4$ exhibits an atom ratio between cobalt (Co) and iron (Fe) of 1:1.9, which is not in accordance with the chemical formula for cobalt ferrite ($CoFe_2O_4$). This can be attributed to the residue unreacted Co which was not removed completely during the fabrication. Carbon atoms (C) were introduced following the coating treatment with oleic acid (OA) and polyethylene glycol (PEG). After the modification period of 1 hour, the atom ratio between the metallic elements (Co, Fe) and C became 1:0.2. After further modification to 4 hours, the additional carbon atoms were introduced making the atom ratio of Co, Fe to C become 1:1.5. From this result, it can be confirmed that prolonging the treatment time leads to an

increase in the content of the coating polymers. Similar results were reported in the previous works [159,173].

The atom ratio of Co:Fe in $CoFe_2O_4$ remains unaffected by the decoration of the nanoparticles on both GNPs and rGO surfaces. However, when $CoFe_2O_4$ nanoparticles are co-precipitated with GNPs and rGO in a 1:1 mass ratio, the atom ratio of carbon to metallic elements in GNPs/$CoFe_2O_4$ is 3.7:1, which is higher than that in rGO/$CoFe_2O_4$, where the ratio is 1.4:1. This observation indicates that GNPs contain more carbon atoms compared to rGO when considering the same mass amount of material. Furthermore, it's important to note that only a minimal amount of sodium (Na) impurity, accounting for up to 3% of the overall composition, is observable from the decoration process. This level of sodium impurity is considered negligible for the purposes of composite fabrication.

Table 2.3 lists the EDS mapping of each element within the fabricated filler materials. It can be observed that $CoFe_2O_4$ distributes uniformly on the material surfaces. Furthermore, the element density from the mapping matches with the results presented previously in Table 2.2.

Table 2.2-3 EDS mapping of each element in the fabricated fillers

Samples	C	O	Fe	Co
GO	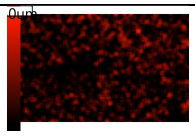	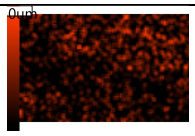	-	-
rGO	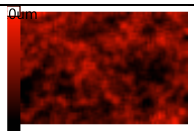	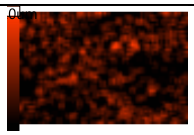	-	-
$CoFe_2O_4$	-	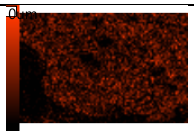	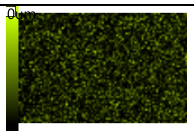	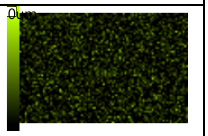
COE1	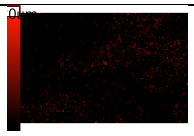	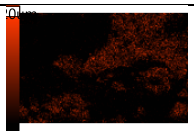	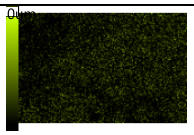	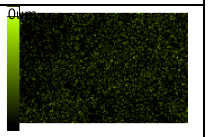
COE4	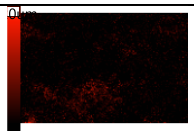	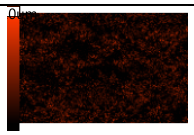	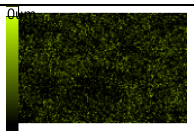	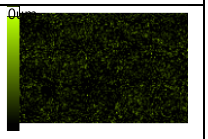
$GNPs/CoFe_2O_4$	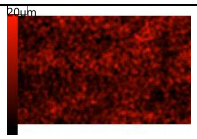	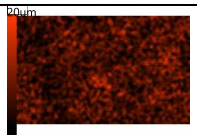	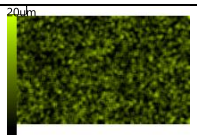	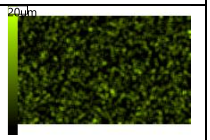
$rGO/CoFe_2O_4$	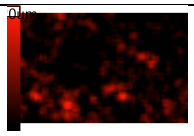	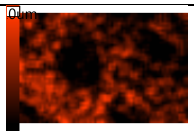	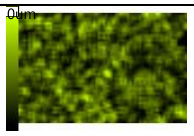	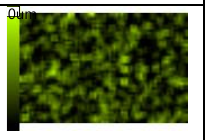

2.5.1.6 Magnetization via Vibrating-Sample Magnetometer (VSM)

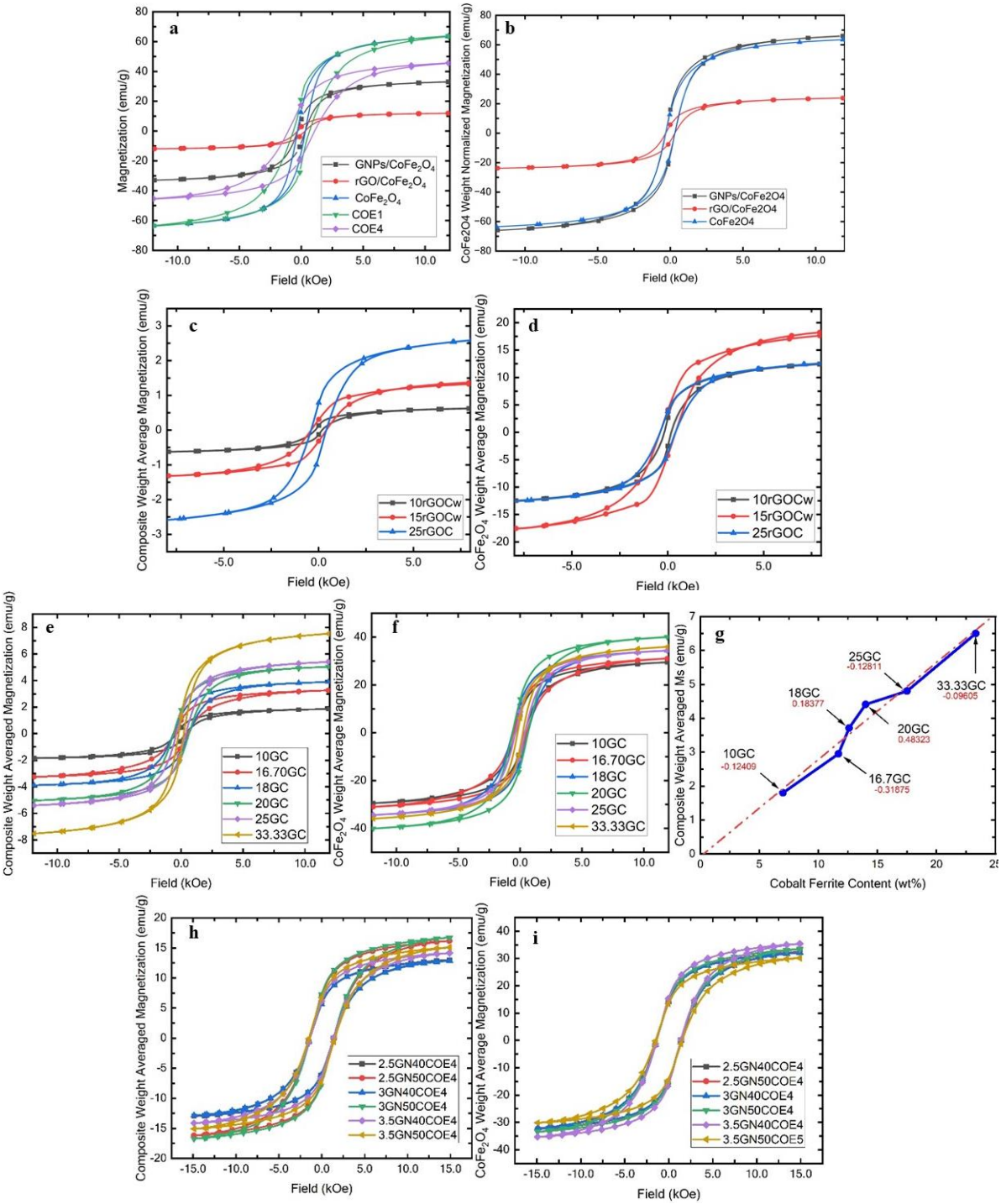

Figure 2-11 a. magnetization of fabricated fillers b. $CoFe_2O_4$ weight normalized magnetization of fabricated fillers c. magnetization of rGOC composite samples d. $CoFe_2O_4$ weight normalized magnetization of rGOC composite samples e. magnetization of GC composite samples f. $CoFe_2O_4$ weight normalized magnetization of GC composite samples g. saturation magnetization of each GC composite sample h. magnetization of COE4 composite samples i. $CoFe_2O_4$ weight normalized magnetization of COE4 composite samples

The magnetization data for the fabricated materials are presented in Figure 2.11. The magnetic moment was measured within a magnetic field range from -12 Oe to 12 Oe. The hysteresis loops of the fabricated materials exhibit ferromagnetic behavior, as noted in reference [58]. In Figure 2.11a, the saturation magnetization (M_s) of pure $CoFe_2O_4$ (Figure 2.9a) is approximately 60.0 emu/g. This value is consistent with previous reports on nanoparticles [48,157,202,203]. However, it is lower than the bulk magnetization of $CoFe_2O_4$, which is 80.8 emu/ g [204]. This difference can be attributed to the smaller size of the magnetic nanoparticles [184]. The reduction in M_s is explained by the surface effect, specifically spin canting, which occurs when the diameter of the nanoparticles is much smaller than the critical single-domain diameter. This phenomenon suppresses the formation of magnetic domain walls [178,202].

From figure 2.11a, the weight normalized M_s experiences a decline when moving from pure $CoFe_2O_4$ and GNPs/$CoFe_2O_4$ (35 emu/g) to rGO/$CoFe_2O_4$ (13.0 emu/g). This can be ascribed to two reasons. First, the reduction in weight fraction of magnetic part in the fillers which follows the rule of mixtures. The second reason can be described by comparing $CoFe_2O_4$ weight normalized M_s of each hybrid filler to the M_s of neat $CoFe_2O_4$ (Figure 2.11b). The values of 60 emu/g are comparable for the GNPs/$CoFe_2O_4$ and $CoFe_2O_4$. However, significant drop can be observed for rGO/$CoFe_2O_4$ hybrid material (20 emu/g) which has also been noted in previous studies by other researchers [201,205,206]. This decrease is consistent with the smaller size of the nanoparticles in the hybrid material, which is approximately 17.4 nm, compared to the roughly 28 nm size of the neat material [46]. In the case of the GNPs hybrid materials, the $CoFe_2O_4$ particles have a diameter of around 30 nm, which is similar to that of the neat material. This reduction could also be attributed to the impact of graphene on the surface properties and microstructure of the CoFe-based material, as reported in reference [137]. These graphene-

induced effects might contribute to the additional drop in Ms. On the other hand, the coercivity (H_c) of $CoFe_2O_4$ was not affected by incorporation with rGO.

Figure 2.11a also displays the hysteresis loops after coating the $CoFe_2O_4$ nanoparticles with OA/PEG. There is no significant drop of M_s after the treatment for 1 hour. Notably, there is no substantial reduction in the M_s observed after this treatment for 1 hour. However, there was a significant drop in the M_s from pure $CoFe_2O_4$ (60 emu/g) after coating the polymers for 4 hours in COE4 (48 emu/g). This can be ascribed to the considerable decrease in the weight fraction of the magnetic component within the coated $CoFe_2O_4$ (COE) nanoparticles as compared to the pristine $CoFe_2O_4$ nanoparticles. These results align with and are consistent with the results of the elemental analysis that were discussed earlier. Moreover, the coercivity (H_c) of the polymer coated $CoFe_2O_4$ (COE) is noticeably higher and shows an increase as the coating reaction time is extended. These results are consistent with the previous reports [207]. The increase in coercivity (H_c) can be reasoned by the reduction of the magnetic dipole coupling interaction between neighboring magnetic nanoparticles that caused by encapsulation of the magnetic nanoparticle [207]. Bertram et al. reported that a strong dipole coupling interaction appears to facilitate magnetization reversal, leading to a decrease in the coercivity value [208].

The composite weight normalized magnetizations of rGOC composites are depicted in Figure 2.11c. The trend in M_s corresponds to the weight fraction of $CoFe_2O_4$ in the composites, following the order of 10rGOCw, 15rGOCw, and 25rGOC, respectively, in line with the rule of mixtures. In the case of GC composites, the M_s increases linearly with the loading of GNPs/$CoFe_2O_4$, as shown in Figure 2.11e and 1.11g. This trend aligns with previous reports [21,64,157,201]. A similar increasing trend in M_s can also be observed for GNCOE composite samples, as seen in Figure 2.11g. However, further investigation is required to confirm the slight

differences in Ms for the composites containing 3.5wt% GNPs (3.5GN40COE4 and 3.5GN50COE4) compared to other GNCOE composites. Considering the $CoFe_2O_4$ weight normalized M_s of rGOC composites (Figure 2.11d), the values align closely with that of the pristine rGO/CoFe2O4 composite, with one exception noted for 15rGOCw. Significant decreases in the $CoFe_2O_4$ weight normalized M_s can be noticed for GC composites (Figure 2.11f) and GNCOE (Figure 2.11i) composites (25-37 emu/g) compared with neat GNPs/$CoFe_2O_4$ (60emu/g). The reduction of $CoFe_2O_4$ weight normalized M_s of $CoFe_2O_4$ after mixing with polymers can also be found in existing reports [205,206,209,210]. Further investigation is needed to understand the deviation in M_s observed in the case of 15rGOCw, GC, and GNCOE composites. The coercivity (H_c) range of all composite materials tends to be matched and scaled with their original fillers.

2.5.1.7 Through Thickness Electrical Conductivity

Table 2.2-4 Through thickness DC electrical conductivity of the fabricated composite samples

Samples	Through Thickness Conductivity (S/m)	Samples	Through Thickness Conductivity (S/m)
PLA	1.16E-09	**2.5GN40COE**	**1.43E-02**
5rGO	7.33E-09	**2.5GN50COE**	**1.19E-03**
8rGO	**8.77E-02**	**3GN40COE**	**3.26E-03**
10rGOCw	1.08E-09	**3GN50COE**	**1.62E-02**
15rGOCw	1.39E-06	**3.5GN40COE**	**5.27E-03**
25rGOC	**2.99E-04**	**3.5GN50COE**	**2.21E-02**
5GN	**7.57E-04**		
10GC	1.17E-09		
16.70GC	4.29E-05		
18GC	**2.16E-04**		
20GC	**2.81E-04**		
25GC	**3.36E-02**		
33.33GC	**8.18E-02**		

The DC electrical conductivity (σ) of the fabricated composites has been measured and is provided in Table 2.4. As anticipated, the conductivity increases as the volume fraction of the conductive fillers (rGO, GNPs) in the composites increases. Furthermore, it is observed that

composites containing GNPs exhibit higher conductivity than those with rGO at the same concentration. This reduction can be attributed to the smaller lateral size of the rGO particles than GNPs particles [46]. This finding aligns with the SEM micrograph analysis discussed earlier. Additionally, the presence of a higher number of out-of-plane functional groups in rGO results in an increased distance between the conductive carbon planes when particles come into contact. This leads to a reduced likelihood of contact between particles and an increase in carrier scattering at the interface due to inter-particle resistance [211].

Moreover, the uniform distribution of the insulated $CoFe_2O_4$ nanoparticles on the rGO/$CoFe_2O_4$ hybrid fillers can block the connection between the conductive fillers in the rGOC composites and reduce the length of the conductive pathways which leads to the tunnelling effect [60,113]. Thus, the GC composites exhibit higher conductivity than rGOC composites. It is evident that GNCOE composites exhibit higher conductivity compared to other filler systems, despite having a significantly lower weight fraction of conductive filler (GNPs). This can be attributed to the higher volume fraction of GNPs, which results from the substantial loading of high-density $CoFe_2O_4$ (COE) nanoparticles. However, it is important to note that the trend in conductivity of GNCOE samples does not strictly follow the rule of mixtures, especially when the GNPs loadings are quite similar in each composite. It is believed that other factors, such as the quality of dispersion of both GNPs and COE within the composites, may lead to different distributions of each constituent, particularly at high COE concentrations (40-50 wt%).

The recommended DC conductivity range for designing materials for EM absorber applications is typically within the range of 10^{-4} – 10^{-2} S/m [36]. The fabricated composites that exhibit conductivities close to this specified range are underlined in Table 2.4. However, it is important to reiterate that DC electrical conductivity serves as a general guideline for

determining the conductive filler loading in composites for EMI shielding applications. This range does not precisely correspond to the ideal absorption range. The primary absorption performance is primarily contingent on whether the absorption resonant peak of reflection loss (RL) occurs within the operational frequency band. This characteristic can be evaluated through the scattering parameters at high frequencies using a vector network analyzer.

2.5.1.8 Electromagnetic Intrinsic Properties

The scattering parameters (S11, S21) obtained from a vector network analyzer (VNA) were utilized as input data for the Nicholsen-Ross-Weir (NRW) calculations [168,169,212] to extract the complex electrical permittivity ($\varepsilon^* = \varepsilon' + \varepsilon''$) and complex magnetic permeability ($\mu^* = \mu' + \mu''$) in the X-frequency band (4-12 GHz). The real parts of both parameters (ε', μ') signify dielectric and magnetic energy storage, respectively. On the other hand, the imaginary parts (ε'', μ'') are associated with the dissipation of energy in terms of dielectric and magnetic losses [17,100,103].

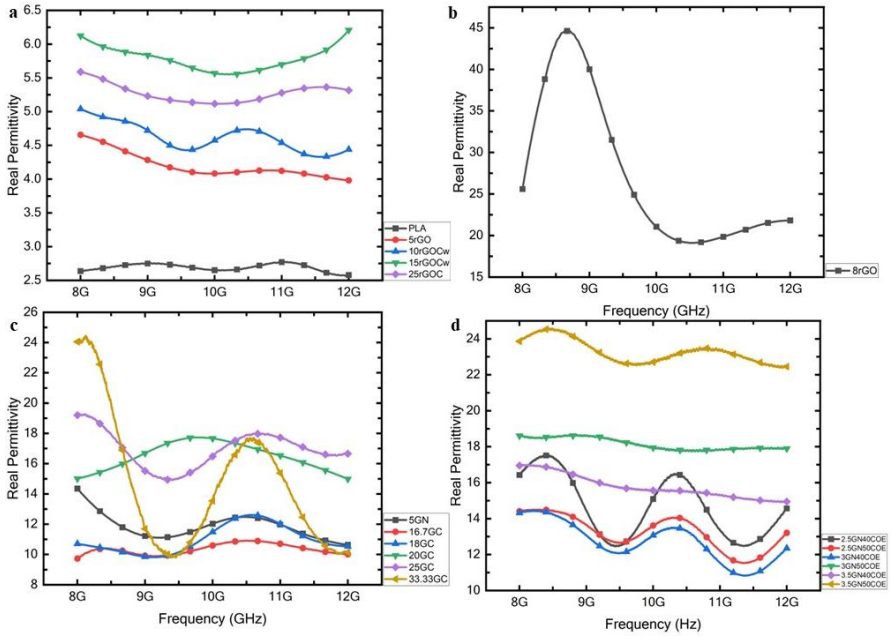

Figure 2-12 Real permittivity of a. neat PLA, rGO composites, and rGOC composites b. 8rGO c. 5GN and GC composites d. GNCOE composites

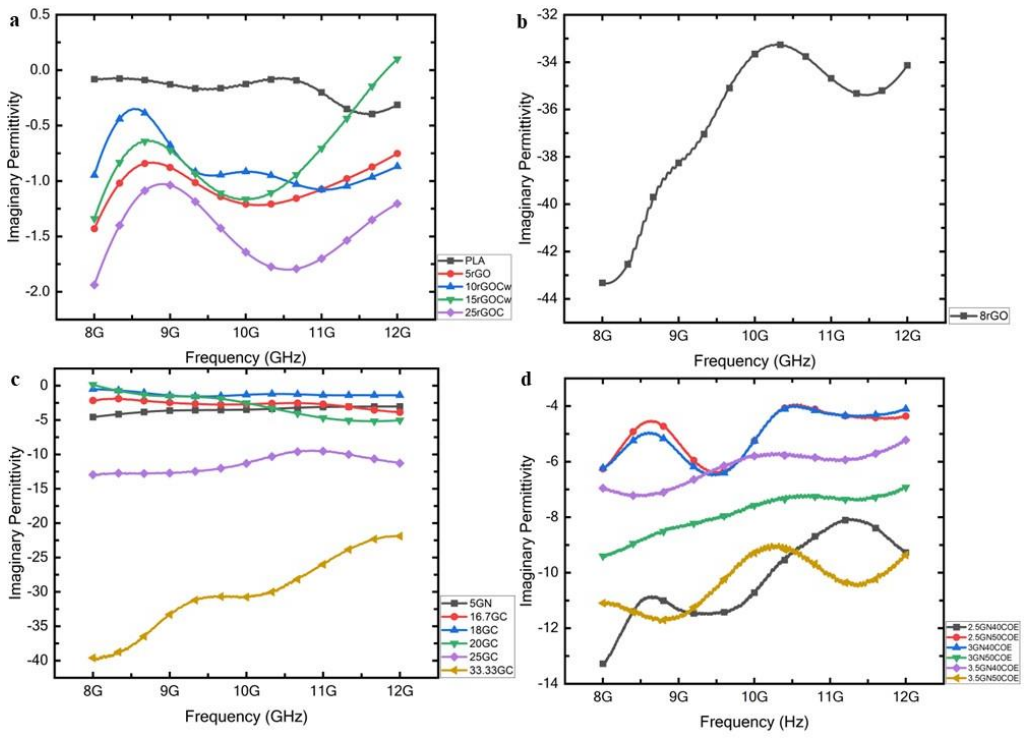

Figure 2-133 Imaginary permittivity of a. neat PLA, rGO composites, and rGOC composites b. 8rGO c. 5GN and GC composites d. GNCOE composites

The real permittivity (ε') is plotted in Figure 1.12. It is evident that the real part of the permittivity of all produced composites show an increase with higher loading of conductive fillers (GNPs, rGO) according to the effective medium theories [20,21,127]. This trend aligns with observations in polymer composites containing conductive fillers [21,46,98,137,157,213–222] and can be attributed to the increase in the number of micro-capacitors and polarization centers within the composites as a result of the conductive filler loading [62,106,112,157,214,223]. These micro-capacitive networks are formed with conductive fillers acting as electrodes, embedded within the insulating constituents which results in more energy storage [106]. This rise in capacitance is likely due to an increase in the conductive network within the composite. With narrow insulative gaps between the conductive layers, high electrical field strength may build up which contributes to the dipolar polarization and electronic polarization of the composites [24,103,223]. Thus, the larger size of conductive fillers (GNPs),

that provide a greater chance for contacting each other, exhibits higher ε' than the smaller one (rGO). This result aligns consistently with the DC conductivity trend. In the case of higher loading of conductive fillers, complex fluctuations in the real permittivity can be observed. These fluctuations indicate the presence of resonance, which can occur when the material becomes highly conductive, and the skin effect becomes a dominant factor in its behavior [216,218,221]. Moreover, the resonance was also possibly due to the matching frequency of electron hopping between the conductive layer to applied EM wave frequency [224]. Similar trends of these fluctuations due to high conductive filler loadings have been documented in previous studies [98,137,157,213–216,218–221].

On the other hand, the imaginary part, which is associated to the EM energy dissipation, primarily contributes to the synergistic effect involving both conduction loss and dipolar relaxation loss, as described by Debey's relaxation [21,62].

The imaginary permittivity (ε") of the manufactured composites also shows consistent increases with the loading of the conductive fillers (GNPs, rGO) of the composite (Figure 1.13). The observed overlap between each concentration is due to two reasons. First, the volume fraction of the conductive fillers in the same system in each plot are very close to each other. Thus, the values of each loading are close to each other. Second, the fluctuation in the imaginary permittivity (ε") over the frequency band is caused by the dielectric resonance that occurs when the frequency of electron hopping between conductive fillers matches with of the EM wave [127,224].

The conduction loss is directly related to the conductive filler concentrations when comparing the composites with the same filler system. Additionally, the conductivity of the composites is also dependent on the size of the conductive filler and the dispersion quality that

affect the ability to construct the conductive network inside the composite as described previously. Consequently, electrons in the composite have a greater mean free path for transfer, enabling them to dissipate more electrical energy [21,24]. Therefore, the composites consist of GNPs fillers provide higher ε" than the ones with rGO. Additionally, the increase in conductivity also causes the shift in dipole polarization [213,219]. The relaxation loss is mainly correlated with the delay of dipolar polarization and electric polarization with respect to a changing electrical field within the material [21,62,103,223]. Moreover, the structural defects in the fillers such as the out-of-plane functional group create polarization centers in the composites [62,106,214]. Furthermore, the increase in filler loading, and the presence of the insulated magnetic $CoFe_2O_4$ nanoparticles also results in enhancement of the Maxwell-Wagner interfacial polarization due to charge accumulations at the interface between each constituent [215,220]. Thus, the loading of both conductive fillers (GNPs, rGO) and insulated magnetic constituents ($CoFe_2O_4$, COE) influence the imaginary permittivity of the fabricated composite.

As depicted in Figure 2.14 and Figure 2.15, the complex permeability (μ*) of the composites shows values close to 1 for the real part (μ') and around 0 for the imaginary part (μ''). Only the 33.33GC and GNCOE samples, which have extremely high loading of magnetic nanoparticles (CoFe2O4, COE), exhibit a slight increase in both these values. This behavior is consistent with existing reports on polymer composites filled with magnetic nanoparticles, which also show complex permeabilities (μ*) hovering around the same range, even at high loading levels [21,52,62,101,134,137,145,157,213,217,220,225–227]. All these reported magnetic materials have saturation magnetization (M_s) comparable to CoFe2O4. However, the complex permeabilities of their composites remain within the same range as observed in this work. The fluctuations in both the real (μ') and imaginary (μ'') parts of the complex permeability are

attributed to the higher M_s associated with higher loading of magnetic constituents in the composites, a phenomenon also observed in previous studies [52,62,103,134,145,156].

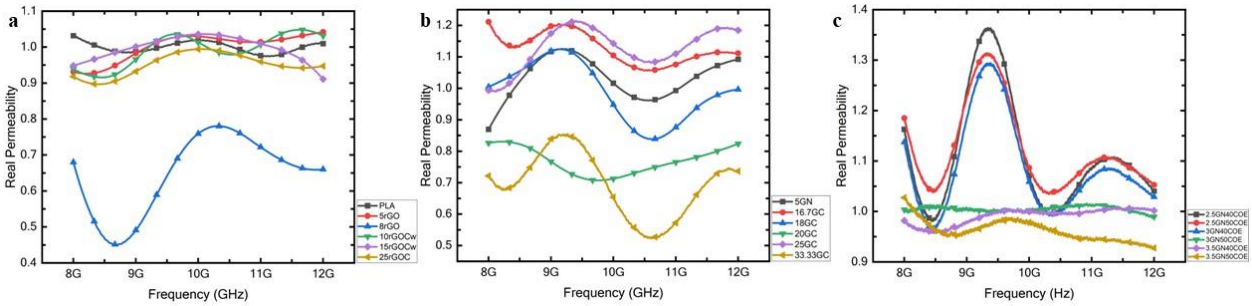

Figure 2-144 Real permeability of a. neat PLA, rGO composites, and rGOC composites b. 5GN and GC composites c. GNCOE composites

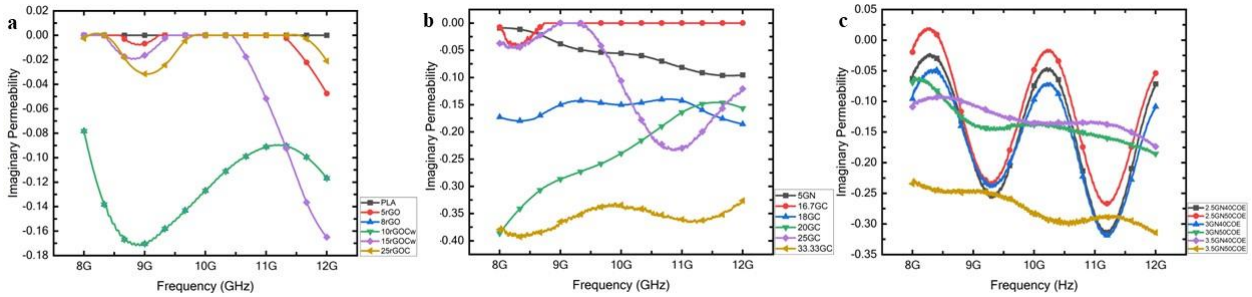

Figure 2-155 Imaginary permeability of a. neat PLA, rGO composites, and rGOC composites b. 5GN and GC composites c. GNCOE composites

Typically, the magnetic loss in ferromagnetic materials results from various factors, including magnetic hysteresis, domain wall motion, eddy current effects, and ferromagnetic resonance. [137,217]. In this case, hysteresis loss can be considered negligible due to the application of a weak magnetic field [137,217,228]. Moreover, the domain wall motion usually affects the magnetic loss in the MHz range [137,217]. Likewise, the magnetic resonance loss of ferromagnetic material usually occurs in the frequency less than 6 GHz [21,137,217]. Therefore, the main mechanism for magnetic loss in the X-band frequency range for this material is the eddy current effect. However, the eddy current effect may not significantly impact magnetic loss due to the insulating behavior of $CoFe_2O_4$. This could explain the low permeability observed in the fabricated composites. Nevertheless, the presence of CoFe2O4 can still contribute to

electromagnetic absorption by manipulating both complex permittivity and permeability through other mechanisms, such as polarization and internal scattering effects, resulting from impedance mismatches at the interface [21,137,217].

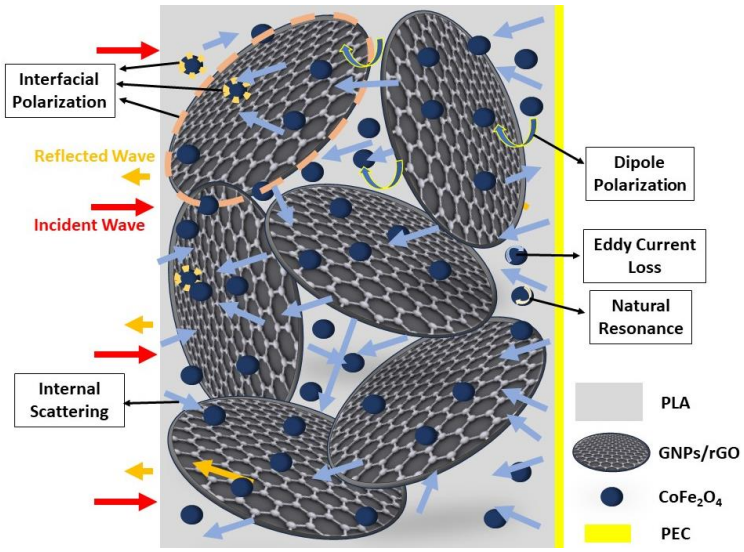

Figure 2-16 Schematic of EM absorbing mechanism for hybrid composites presented in this work.

As shown in figure 2.16, incorporating graphene-based conductive materials $CoFe_2O_4$ nanoparticles in the polymer composites does not only help absorb EM energy via tuning the intrinsic properties through the rule of mixtures, but also exhibits other loss mechanisms as discussed previously in this section.

2.5.1.9 Electromagnetic Absorption in X-Band

The reflection loss (RL) can be utilized as a figure of merit to determine the absorption of the fabricated composites. The extracted complex electrical permittivity (ε*) and magnetic permeability (μ*) of each fabricated composite were put in the transmission line equations from chapter 1 to simulate the reflection loss (RL) at the normal incidence on the front face of the materials. The parametric sweep was set for the thicknesses of the material from 1 mm to 10 mm with 1 mm step. The maximum RL and the operation frequency bandwidth (BW) at the RL at -

20 dB are focused as the performance of the absorber in this work, since the RL at -20 dB meets the minimum requirement for most of the commercial applications [1–6].

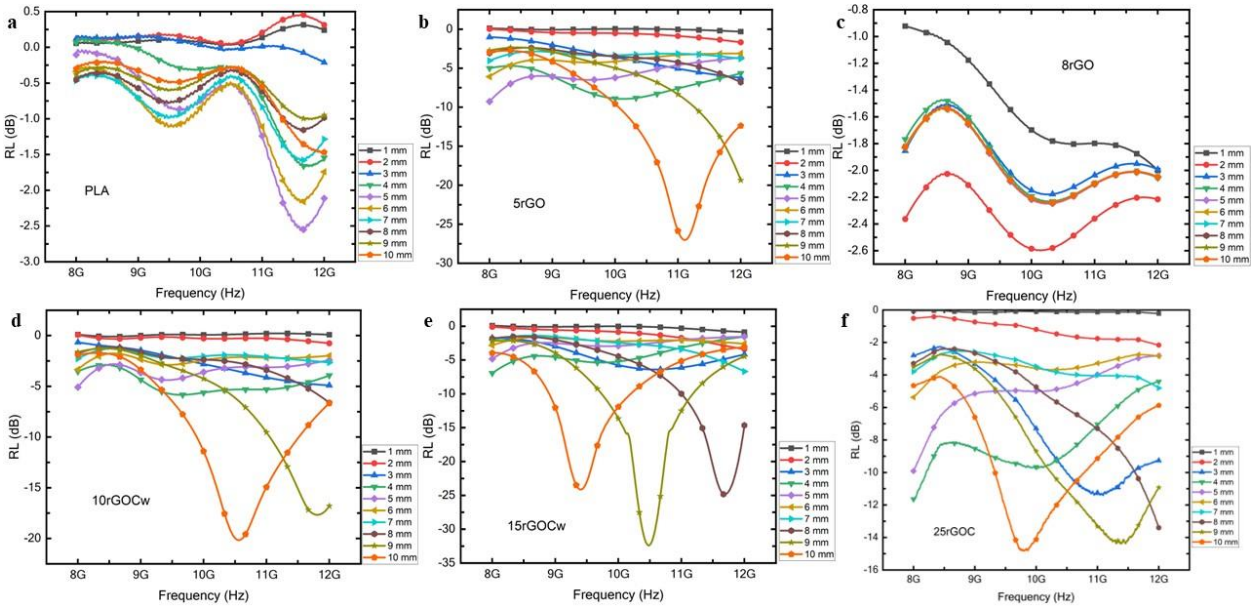

Figure 2-17 Reflection loss of composites with 1-10 mm thickness a. PLA b. 5rGO c. 8rGO d. 10rGOCw e. 15rGOCw f. 25rGOC

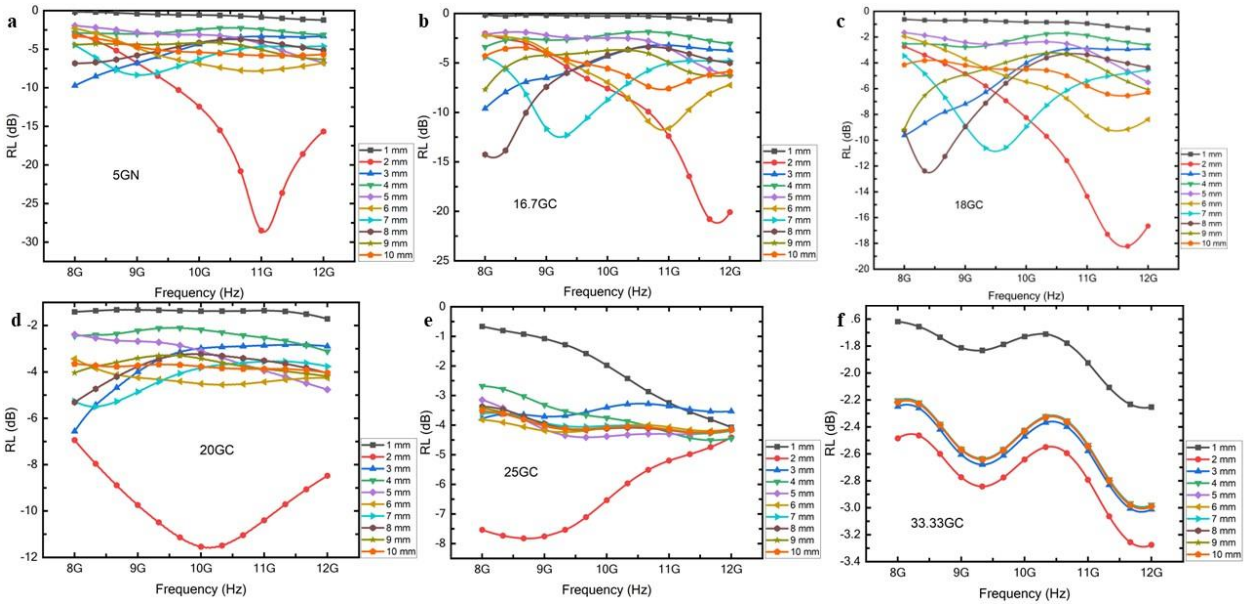

Figure 2-18 Reflection loss of composites with 1-10 mm thickness a. 5GN b. 16.7GC [ASC cited] c. 18GC d. 20GC e. 25GC [ASC cited] f. 33.33GC [ASC cited]

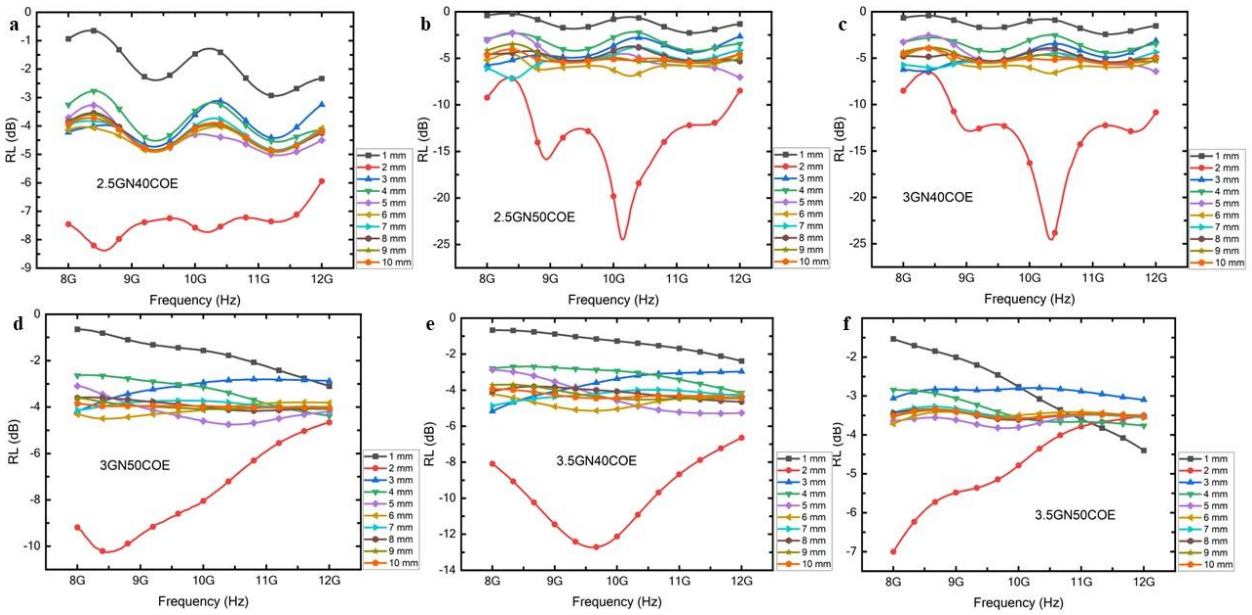

Figure 2-19 Reflection loss of composites with 1-10 mm thickness a. 2.5GN40COE b. 2.5GN50COE c. 3GN40COE d. 3GN50COE e. 3.5GN40COE f. 3.5GN50COE

The simulated reflection losses (RL) for the fabricated composites are illustrated in Figure 1.16, Figure 1.17, and Figure 1.18. As expected, neat PLA (Figure 1.16a) displayed a low RL with a maximum value of -2.5 dB, owing to its insulating and non-magnetic properties, making it transparent to electromagnetic (EM) energy. Similarly, composites such as 8rGO, 25GC, 33.33GC, 2.5GN40COE, 3GN50COE, and 3.5GN50COE, which exhibit high conductivity and become highly reflective to EM energy in the X-band, also show the RL values that do not exceed -20 dB. This can be attributed to the significant impedance mismatch between these composites and free space, resulting in high reflection at the front face of the materials. The high conductivity in these composites can be explained by two factors. First, they contain high concentrations of conductive fillers (rGO, GNPs) that exceed the conductive percolation threshold. Second, the interconnection of conductive filler morphologies forms a conductive network within the composite, which is influenced by the types of fillers and their dispersion quality, impacting the overall conductivity of the bulk composites, as discussed in the previous section on DC conductivity.

The composites consist of 5rGO, 10rGOCw, 15rGOCw, 25rGOC, 20GC and 3.5GN40COE have DC conductivity close to the recommended range [36]. However, there is no absorption peak in the focused frequency band (8-12 GHz) for 25rGOC, 20GC, and 3.5GN40COE. This can be ascribed to the intrinsic impedance, that are acquired from the intrinsic properties (ε*, μ*), does not provide the standing wave condition that can match with the design thicknesses within the frequency range [20,21,170]. Normally, the attenuation can be enhanced if the thickness of the material matches with the sequence of a quarter wavelength of the standing wave [170]. Furthermore, the maximum absorption peaks above -20 dB for 5rGO, 10rGOCw, 15rGOC exist at the composite thickness of 8 mm or above due to the same reason. Therefore, these composites may not be appropriate for applications that have size limitations.

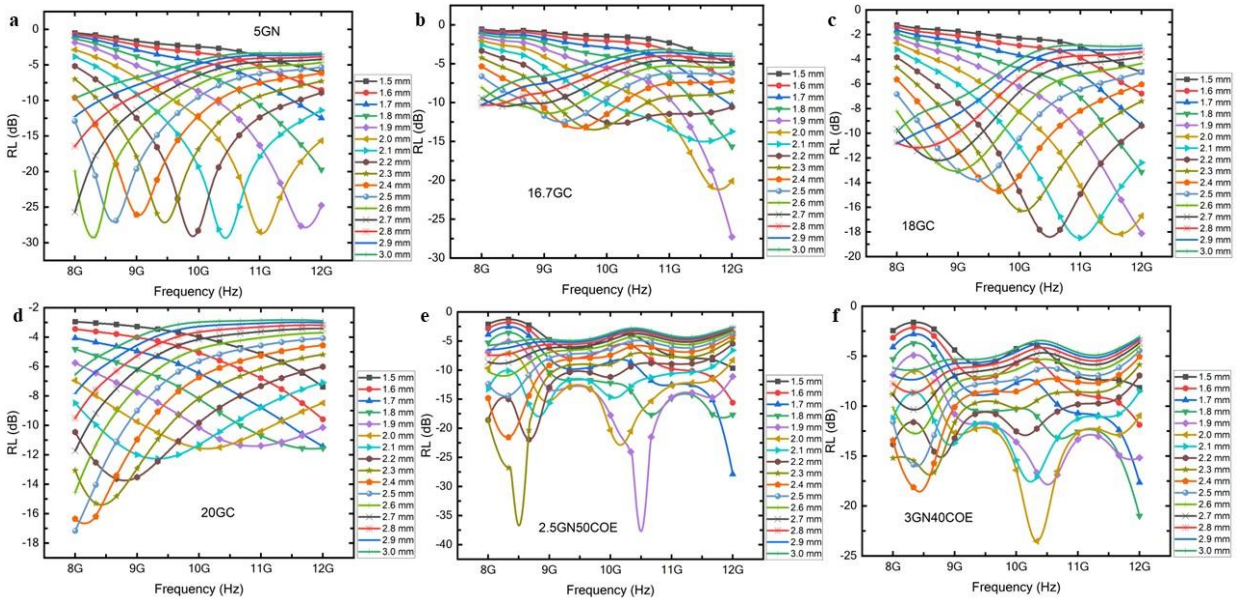

Figure 2.20 Reflection loss of composites with 1.5 – 3.0 mm thickness a. 5GN b. 16.7GC c. 18GC d. 20GC e. 2.5GN50COE f. 3GN40COE

The composites exhibiting absorption peaks around -20 dB or greater within the frequency band include 5GN 16.7GC, 18GC, 2.5GN50COE, and 3GN40COE. These peaks occur at a thickness of approximately 2 mm for all these composites. Further analysis of the

reflection loss (RL) for these composites was carried out at thicknesses ranging from 1.5 mm to 3 mm, with a sweep resolution of 0.1 mm.

In the case of the 5GN composite (Figure 2.20a), the maximum RL ranges from -25 dB to -30 dB within thicknesses ranging from 1.9 mm to 2.6 mm. Notably, there is an observable trend where the peak shifts towards lower frequencies as the thickness of the composite increases. This phenomenon can be ascribed to the matching between the propagation distance and the sequence of quarter wavelengths of the electromagnetic (EM) wave inside the material the material, while the wavelength of the EM wave for 8-12 GHz frequency band is ranging from 37.5 – 25.0 mm. Consequently, resonance occurs, leading to the attenuation of EM energy at a specific frequency where the wavelength equals the mentioned distances. Therefore, the thicker composite leads to longer propagation distance that matches with the quarter wavelength, which lowers the frequency at the peak. The effective operation bandwidths (BW) within the -20 dB range span from 600 MHz to 930 MHz. Notably, there is an observed trend where the peaks at higher reflection loss (RL) also correspond to wider bandwidths.

The 16.7GC composite (Figure 2.20b) exhibits a similar pattern to the 5GN composite, with the peak shifting towards lower frequencies as the thickness increases. However, this composite only features two peaks achieving absorptions greater than -20 dB. The maximum absorption is noted at -27 dB for a thickness of 1.9 mm, with a corresponding bandwidth of 280 MHz. It is noteworthy that the peak primarily exists around 12 GHz, indicating that the effective bandwidth is mainly accounted for in the X-band. Similarly, the 18GC composite (Figure 2.20c) follows the same trend in peak positions. Notably, lower RL is observed as the thickness decreases. This behavior can be attributed to the onset of phase mismatch occurring as the thickness decreases, particularly at the 1 mm step. The difference between the quarter-

wavelength distance and the thickness becomes more pronounced with increasing thinning in each step. The highest RL peak is at -19dB. The significant deep peaks can be achieved from 2.5GN50COE composite (Figure 2.20d). The absorption at -37 dB and -38 dB are attributed to the thickness of 2.3 mm and 1.9 mm, respectively. The corresponding BW for these peaks are 630 MHz and 610 MHz, respectively. The final effective composite is 3.5GN40COE (Figure 2.20e). The maximum RL -23.5 dB with BW of 400 MHz was achieved.

Table 2-5 The comparison of EM absorption and BW with other reported absorbers

Reports	**Materials**	**Thickness (mm)**	**Max RL (dB)**	**Max BW (GHz) @-10dB**
This Work	GNPs/$CoFe_2O_4$ in PLA	1.9	-38.0	3.21@-10dB 0.36@-20dB
Zong et al. [213]	rGO/$CoFe_2O_4$ in Paraffin	2.0	-47.9	4.9
Fu et al [153]	PVP/rGO/$CoFe_2O_4$ in Paraffin	2.0	-18.5	3.7
Song et al. [21]	Paraffin/GN/$CoFe_2O_4$	1.5	-28.5	1.1
Min et al.[49]	SBA-15/$CoFe_2O_4$	2.0	-18.0	4.5
Li et al. [62]	Nickel-N@carbon in Paraffin	3.0	-32.3	5.0
[101]	FeCo/rGO in Paraffin	2.5	-40.2	3.2
Kong et al.[223]	rGO/CNTs in poly(dimethyl siloxane)	2.75	-55	3.5
Fu et al. [59]	$NiFe_2O_4$ nanorod/rGO in Paraffin	2.0	-29.2	4.5
Cui et al. [229]	MXene/rGO/Nb2CTx/Fe_3O_4 in Paraffin	2.5	-59.17	6.8
Bi et al. [136]	Ni@Co/Carbon@polypyrrole in Paraffin	2.0	-48.76	5.10
Hou et al.[225]	NiSe2-$CoSe_2$@C/$Ti_3C_2T_x$ in Paraffin	2.6	-60.46	5.7
Ran et al.[226]	$BaTiO_3$ nanotubes/rGO in Paraffin	2.5	-44.9	5.4
Wang et al. [52]	Ti3C2/Fe3O4 in PANI	1.9	-40.3	5.2
Zhang et al.[50]	NiCo2S4@C/Porous Carbon in Paraffin	2.1	-59.36	6.8

The example of the published reports on the composites consisting of polymers, conductive materials, and magnetic materials at thickness around 2 mm are listed in Table 5. It can be noticed that this work can compete with other works that contain materials with similar production complexity. The literatures that provide higher performance of the absorber require higher effort to overcome the production complexity, as well as higher cost on the precursor materials. This can imply that our work provides guidelines for composite absorber fabrication that are cheap and simple but can achieve the performance that meets most application requirements.

2.5.2 Electrical Conductivity and Electromagnetic Absorption of Twin-Screw Compounding PLA/GNPs

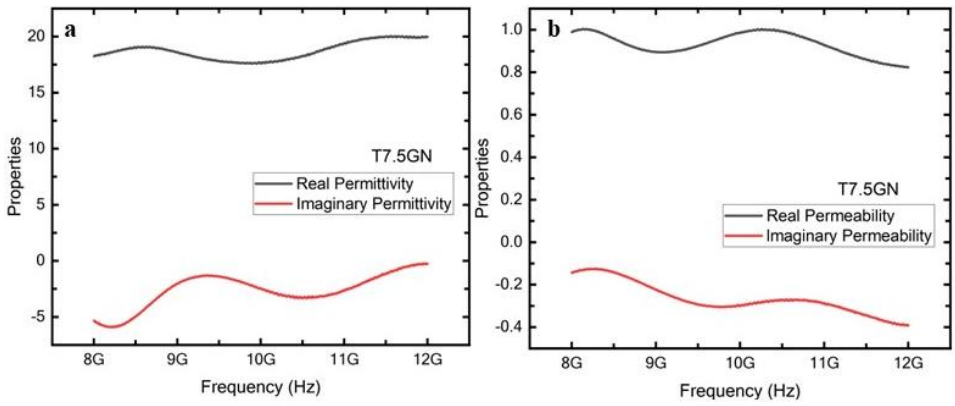

Figure 2.21 Intrinsic properties of T7.5GN a. electrical permittivity b. magnetic permeability

In order to expedite the production rate and achieve the requirement of economical scalable method. The PLA/GNPs composite with the concentration of 7.5wt% were also manufactured by twin screw compounding method. The electrical conductivity, intrinsic properties, and EM absorption of the fabricated composite were characterized similarly to the composites fabricated from solution mixing method. The DC electrical conductivity of the composite was achieved at 1.0 S/m which is higher than the recommended range for EM

absorber applications. However, the characterized intrinsic properties (Figure 2.21) provide the absorption peak of -21 dB within 8 – 12 GHz band (Figure 2.22) with the BW at -20 dB of 0.2 GHz at the thickness of 2.0 mm. Thus, this composite can also be a good candidate for a baseline material used to design and fabricate the periodic porous EM metamaterial absorbers. The difference between composites produced by solution mixing and twin-screw compounding methods in the morphologies and their effect on electrical conductivity were already reported in our previous work [230].

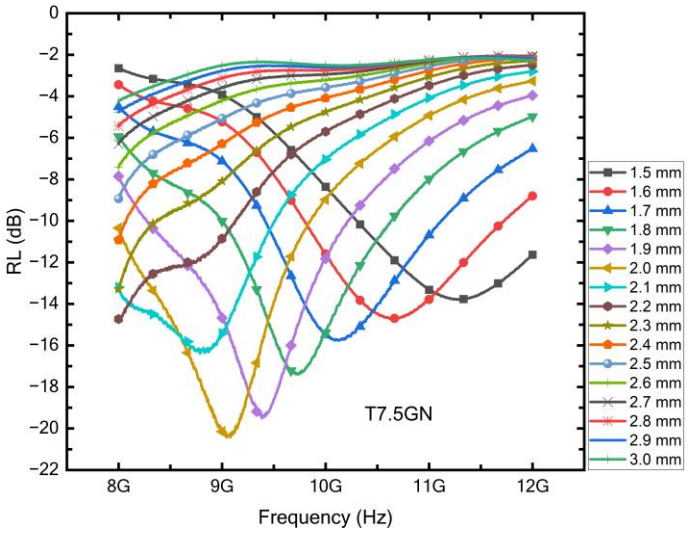

Figure 2-22 Reflection loss of T7.5GN at 1.5 - 3.5 mm with 0.1 mm step

2.6 Conclusions

In summary, the hybrid fillers composites consist of conductive fillers (rGO, GNPs) and magnetic nanoparticles ($CoFe_2O_4$) in PLA matrix were prepared and characterized. The comparative study in the effects of graphene types, the incorporation with $CoFe_2O_4$, concentration, dispersion quality, and production technique on the EM absorption performance at 8-12 GHz band were performed. Moreover, this work also proposes the technique to disperse high concentration of $CoFe_2O_4$ in the composites by introducing the stabilizer OA/PEG on the surface of $CoFe_2O_4$ nanoparticles. Unlike the decoration on graphene technique, this method was

used to avoid an effect on the concentration of the conductive fillers. The results show an enhancement in magnetic permeability with the increments of $CoFe_2O_4$. Moreover, the electrical permittivity can also be improved by tuning the concentration of conductive fillers. Furthermore, the designing of the micro morphologies of the composite systems also affects the EM absorption performance through other loss mechanisms such as polarization and internal scattering. Thus, the desired absorption and operation bandwidth can be achieved. The maximum RL achieved is -38 dB with the operation BW at -20dB of 630 MHz. This absorption level can compete with previous works that require similar production complexity and cost effectiveness. Moreover, the composites manufactured by twin screw extruder, which is economical scalable than solution mixing, also provide the RL that meets the minimum requirement for commercial applications. It is believed that the reported composites from both methods can be great potential baseline material for periodic porous EM metamaterial absorber design.

Chapter 3 Electromagnetic Field – Based Computational Modelling for Periodic Porous Structure Metamaterial EM Absorbers

3.1 Related Publication

1. Kanat Anurakparadorn, Alan Taub EM. Design and Optimization of the Porous Metamaterial EM Absorbers in X-band. in 2023 IEEE Symposium on Electromagnetic Compatibility & Signal/Power Integrity (EMC+ SIPI), IEEE, 2023. Grand rapids, Michigan, USA pp. 218-218.

3.2 Introduction

In the first chapter, it is discussed that incorporating porous structures into polymer EM absorbers offers several advantages for improving absorption. This improvement occurs through multiple mechanisms, including heightened internal scattering, enhanced impedance matching, and increased filler concentration on the cell wall. Additionally, the introduction of pores serves to decrease the density of the absorbers, making them well-suited for applications where lightweight materials are preferred [36,55,67–71,74,79,80,191,231–236]. The most straightforward method for incorporating a porous structure into the material involves foaming. Nevertheless, the characteristics of the resulting foams, including pore size, cell wall thickness, and pore distribution, heavily rely on the conditions during the foaming process [71,98,99,237,238]. This dependence poses challenges in precisely controlling these conditions to achieve the desired porous structures. The range of processing parameters that can be adjusted for varied morphologies includes foaming methods, temperature, pressure, time, foaming agent,

and pressurizing rate. Furthermore, the resulted morphologies are random and not repeated. Therefore, experimenting with parameter variations to identify an optimal morphology for EM absorption is not feasible in practical design scenarios.

In addition, alternative methods for incorporating macro pores into absorbers, such as 3D printing or machining of scaffolds and honeycombs [75,78,79,234,235,239–242], can demand substantial effort to attain the desired morphologies for EM absorption. Given these challenges and limitations in experimental approaches, computational modeling methods emerge as a more practical and cost-effective means to predict EM absorption performance. These modeling techniques offer the advantage of forecasting absorption outcomes before the actual fabrication of samples for experimental testing. There are existing reports on structure design for porous EM absorbers that utilized computational modelling to predict their absorption performance. For instance, Luo et al. [241] designed the gradient porous structures for broadband microwave absorbing applications using finite element integral technique (CST Microwave Studio). The study varied the parameters including the number of layers, layer height, apertures of square holes and the wall thickness, and simulated the scattering parameters (S11, S21) for absorption prediction. The optimal geometry provided a match between simulation results and experimental measurements of the absorber with BW@10 of 14.06 GHz. Méjean et al. also combined computational simulations and prototyping to design pyramidal absorbers from carbon fibers loaded with epoxy foam. The resulted RL of -30 dB was achieved which is 10 dB higher than the commercial pyramidal absorbers (APM12 from SIEPEL).

Furthermore, the metamaterial concept which is based on the interactions between the repeated units in periodic structures provides opportunities to enhance absorptivity through resonance, as well as to obtain the multi-resonance modes which result in broader operational

bandwidths [15,83–85]. The structural design for metamaterial absorber can also be performed via computational modelling. For example, Ren et al. [94] utilized numerical simulation to design the meta-structure of carbon/ABS composites. The structures contain repeated arrays of cylinder pillars on the flat surface. The simulation was used to predict the dielectric resonant modes of electric field at each frequency which cause the attenuation based on metamaterial concept. The 3D-printed samples were fabricated for validation and showed good agreement with the modelling results. The produced absorber provided an absorptivity higher than 90% over the whole operating band from 3.9 to 12 GHz. Ding et al. [14] also employed the computation simulation to design the absorbers composed of a periodic array of metal-dielectric multilayered quadrangular frustum pyramids. The pyramids provide resonant absorption modes at multi-frequencies which overlap with each other resulting in a wide band of absorption. The simulation agreed with the experimental results which produced the absorption at normal incidence above 90% in the frequency range of 7.8–14.7 GHz. Similar works on using computational modelling for designing the metamaterial absorbers are reported for both on traditional metamaterials that consisted of metallic structures on the dielectric slabs [15,85,90,243–245] and metamaterials that contain complex porous structures [80,87,92,93,95,96].

Table 3-1 EM intrinsic properties of 30 wt% Fe_2O_3/GNPs in paraffin wax extracted from Song et al. [21] by Bregman et al. [99]

Frequency (GHz)	**ε'**	**ε"**	**μ'**	**μ"**
8	14.40	10.21	1.18	0.04
9	10.68	8.40	1.19	0.06
10	9.19	5.56	1.17	0.07
11	10.34	4.21	1.15	0.14
12	11.41	3.99	2.00	0.16

By combining the advantages of porosity of foams and the periodicity of metamaterial, the novel periodic porous structured EM absorbers were designed to satisfy multi-objective characteristics (high absorption, wide operation bands, multi-incidence angles, polarization independence). Recently, a previous member in our group, Bregman et al. [97–99], proposed the ability to investigate the EM absorption responses of periodic porous structure via EM field-based computational method. The simulation was performed using finite element analysis for the complex porous meta-structures. The simple geometries (cubic, sphere, cylinder) of air pores were introduced to the periodic unit cell (Figure 3-1a). The input material intrinsic properties were obtained from Song et al. [21] for rGO/Fe_3O_4/Paraffin composite which are listed in Table 3-1. The result shows the improvement of RL with the shift of the peak frequencies when the different geometries of air pores were input (Figure 3-1b). The electric field distribution plot in Figure 3-1c reveals notable enhancements at specific positions on the cell wall, corresponding to the frequency peak of RL. These enhancements stem from the interaction among periodic pores, inducing resonance within the absorber structure and showcasing metamaterial behavior. However, the improvement trend is not consistently increasing with pore geometry. This suggests that only specific geometries can be optimized to achieve the highest absorption performance, highlighting the challenge in predicting structures for optimal design using a parametric sweep method that addresses the multi-objectives of the absorbers.

Given this complexity, it is proposed that an optimizer program be applied. Such a program could determine the maximum RL while simultaneously identifying the optimal point for multi-objective design. This approach is anticipated to provide a more systematic and efficient means of achieving the desired absorber performance by addressing the intricate relationships between pore geometry and electromagnetic absorption characteristics.

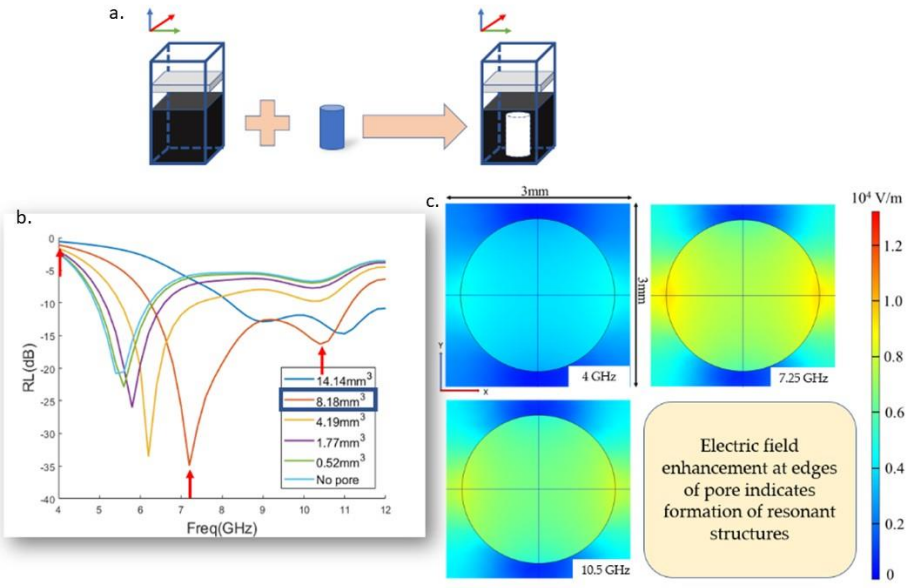

Figure 3-1 Computational modelling periodic sphere void metamaterial structure reported by Bregman et al. [99] a. Concept of Modelling b. RL of the reported absorbers with different size of sphere void c. electric field distribution from X-Y direction (top-view) at different frequencies of the model with 8.18 mm^3 sphere void size.

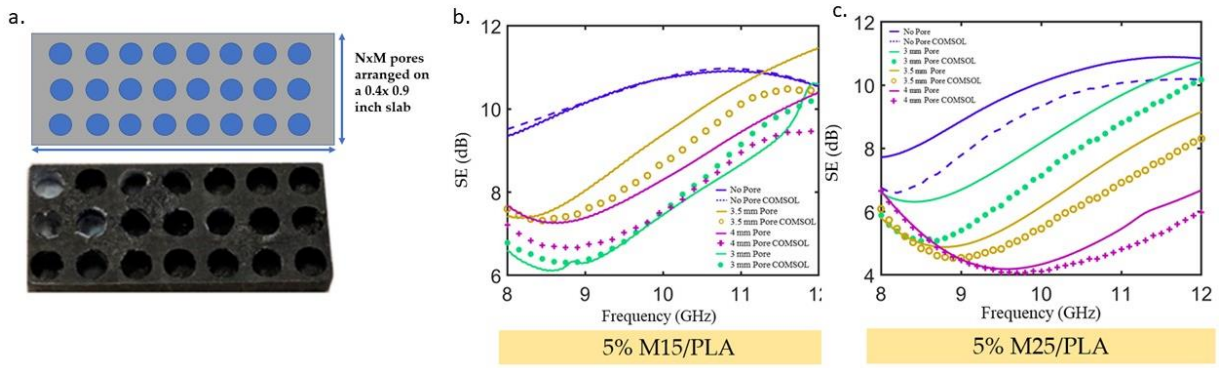

Figure 3-2 Validation of computational model with scattering measurement in TE10 mode provided by Bregman et al. [98] a. the geometry consists of arrays of cylinder pores that is used for the validation b. validated SE results of 5wt% M15-grade GNPs c. validated SE of 5 wt% M25-grade GNPs

Furthermore, Bregman et al. [98] conducted experiments to validate the accuracy of their models by fabricating real absorber samples. Figure 3-2a displays Bregman et al.'s GNPs/PLA composites, created through compression molding and machining periodic arrays of cylinder holes on the top surface. EMI SE was measured using a Vector Network Analyzer (VNA) with a WR-90 waveguide in TE10 mode, and the results were compared with simulation outcomes. The measured SE trends closely matched the modeling at each frequency point, with slight

differences in magnitude. This alignment suggests that the author's modeling method is reliable for designing periodic porous metamaterials.

Building on this validation, the chapter identifies opportunities for further exploration of periodic porous structures and emphasizes the potential for optimization to achieve a multi-objective design for EM absorbers. Utilizing material intrinsic properties from Chapter 2 as inputs, computational models were developed based on Bregman et al.'s method [97–99]. The exploration extended to higher levels of complex structures, and a Monte-Carlo algorithm was developed and applied to identify the optimal structure for multi-objective design, considering both RL and BW. The results indicated that enhanced RL and broadened BW could be achieved beyond baseline composites, meeting the absorption requirements demanded at a military level for EM absorbers.

3.3 Computational of Periodic Porous Structure

3.3.1 Model Construction

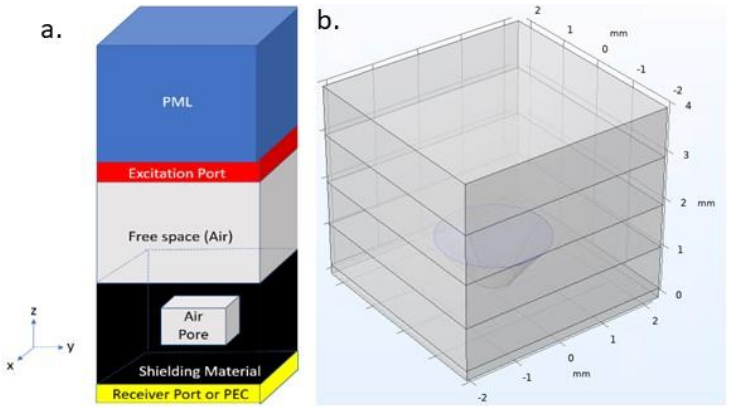

Figure 3-3 a. Schematic showing a unit cell of EM metamaterial absorber which is used in this work. b. Example of single cone void geometry generated in COMSOL.

The computational modeling methodology was based on the approach proposed by Bregman et al. [98,99]. Finite Element Analysis (FEA) was conducted using COMSOL

Multiphysics 5.6 with the Radio Frequency (RF) module [246]. The models comprised 3D periodic cuboid lattice in Cartesian coordinates, serving as unit cells with layers of materials. These models aimed to determine scattering parameters responsive to input EM radiation. The simulation was performed in the X-band frequency ranging from 8-12 GHz corresponding to the wavelength of 25.0 – 37.5 cm in free space.

The unit cell's top surface, representing the absorber layer, had an excitation port boundary condition with periodic reference points and 1W input power in transverse electric polarization mode (TE). The angle of incidence can be defined as input conditions as normal incidence, oblique incidence, or TE10 mode. To prevent secondary effects from surface reflections, domain-backed slit conditions combined with a perfectly matched layer (PML) were applied to the top air layer. Periodic boundary conditions were used in both x and y directions.

For SE simulations, a receiver port boundary condition was applied at the bottom of the absorber. The simulated S21, representing the transmission coefficient (τ), was used to calculate SE based on Equation 1.10. For RL simulations, a perfect electrical conductor (PEC) surface boundary condition was applied at the absorber's bottom. The simulated S11, representing the reflection coefficient (Γ), was used to determine RL using Equation 1.2.

In cases involving metamaterial structures, air pores or material pillars were introduced into the material layer. Figure 3-3b illustrates an instance of the model generated in COMSOL, featuring a conical air pore within the unit cell.

3.3.2 Mesh Discretization and Elemental Order Tests

Figure 3-4 depicts the mesh refinement analysis conducted for the model. According to the COMSOL RF module user guide [246], the criteria for defining mesh size constraints are

based on being less than 1/10 of the wavelength (λ) and 1/2 of the skin depth (δ), the latter of which is determined by the equation:

$$\delta = \sqrt{\frac{2\rho}{2\pi f \mu_o |\mu^*|}} \tag{3.1}$$

Here, ρ represents the bulk resistivity of the material, f is the frequency, μ_0 is the magnetic permeability of free space, and μ* is the magnetic permeability of the material. The simulation employed the auto-meshing option in COMSOL with size constraints. A rectangular sweep was utilized in the PML layer, while free triangular meshes were applied to the surfaces, and free tetrahedral meshes were employed for the internal 3D structures. Mesh sizes were finer in smaller parts of the geometry.

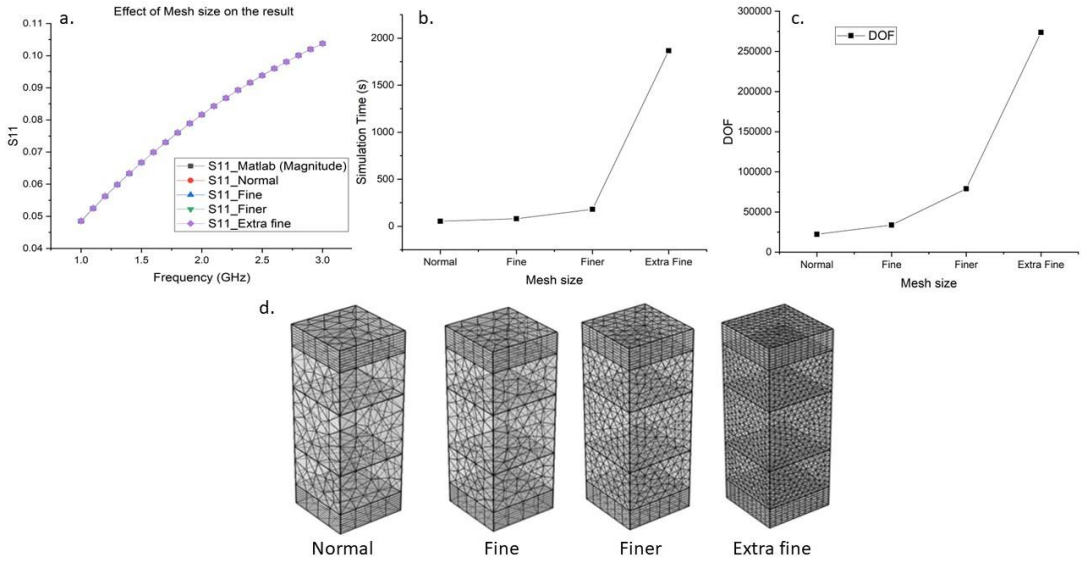

Figure 3-4 Mesh discretization sensitivity test of a single slab absorber a. comparing the solutions between each mesh size and analytical solution from transmission line equation (MATLAB) b. Simulation time of models with different mesh sizes. c. Degree of freedom of the models with different mesh sizes. d. Example of mesh sizes defined in COMSOL [246].

Various mesh size options, including Normal, Fine, Finer, and Extra Fine, were tested with a bulk material. FEA solutions were compared with analytical solutions calculated from the transmission line equation from Chapter 1 using MATLAB. As depicted in Figure 3-4a, the

solutions from each mesh size setting closely matched the analytical solutions, with less than a 0.1% error.

Figure 3-4b and 3-4c illustrate the simulation time and the degree of freedom (DOF), which increase as smaller meshes are selected. Slight increases were observed from Normal to Fine to Finer before a sharp rise with the selection of the Extra Fine mesh. Consequently, a finer mesh was deemed the optimal setting for this study.

Figure 3-5 displays plots of the elemental order test in both the transverse electric polarization mode (TE) and transverse magnetic polarization mode (TM). The simulation results were compared with analytical results. Notably, it is evident that the linear elemental order yields the highest error when compared to the analytical solution. While the cubic order demonstrates an overlap with the analytical solution for TE, errors persist in the TM mode. Consequently, the quadratic elemental order is identified as the most suitable choice for this study.

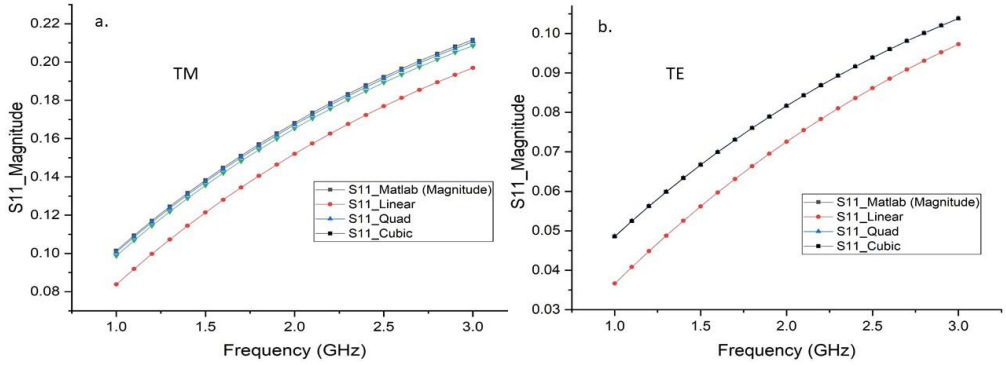

Figure 3-5 Elemental order analysis that compared each elemental order with analytical solution from transmission line equations (MATLAB) a. for transverse magnetic field mode b. for transverse electric field mode.

3.3.3 Model Validation

After mesh discretization and elemental order optimization, the model was validated by inputting material intrinsic properties from Song et al. [21] as shown in Table 3-1. RL was simulated (figure 3-6a) and compared the value with experimental reported by Song el al. (figure 3-6 b). The results shows agreement in the trend and position of the absorption peak around 4.7

GHz. The reported maximum RL from the experiment was -27.5 dB while the simulated result from our model was -24 dB which is still lower than the experimental result. Combined with the validation performed by Bregman et al [98], it can implies that this model can be used to predicted the EM absorption of periodic porous structure metamaterial EM absorber.

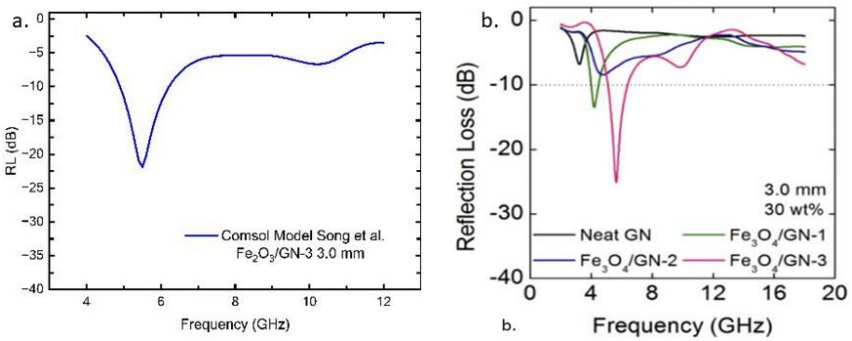

Figure 3-6 The validation of modelling result a. in this work compared with experimental result from b. Song et al. [21] for Fe_2O_3/GN-3 sample.

3.4 Monte-Carlo Optimization

3.4.1 Optimizer Construction

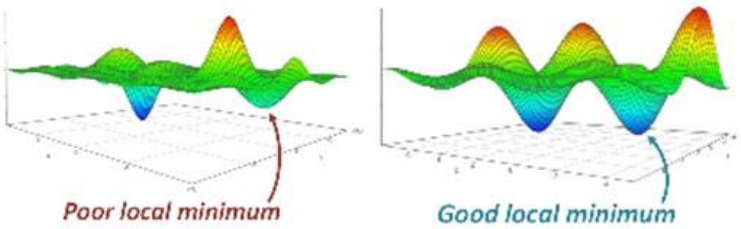

Figure 3-7 Concept of global solution and local solution adapted from COMSOL Radio Frequency Module user guide [246].

As mentioned in the introduction of this chapter, the parametric sweep method typically involves systematically varying parameters within a specified range to explore the design space. However, when the parameter space is large or the relationship between parameters and objectives is not straightforward, this approach may become impractical or inefficient. In such cases, an optimization algorithm can be employed to intelligently search for the optimal set of parameters that satisfy multiple design objectives [247]. By using an optimizer program, the

process of finding the best configuration for your meta-structure EM absorber can be automated, taking into account multiple objectives. This can save time and resources compared to exhaustive parametric sweeps. Additionally, it allows for a more systematic and intelligent exploration of the design space, leading to improved performance in terms of the specified criteria.

The choice of the optimization algorithm must be selected carefully so that the optimized solution can reach the global solution in the parameter space. Figure 3-7 illustrates the concept of local minimum solution and global minimum solution. Some optimization algorithms such as Nelder-Mead method [248,249] or particle swarm [13,250] provide the optimized solution by improving the objective function from the initial point. However, such algorithms provide a chance to achieve the solution at the local point which may not be the global point in the parameter space. Therefore, the algorithms that are able to search the solution distributionally all over the parameter space are more applicable.

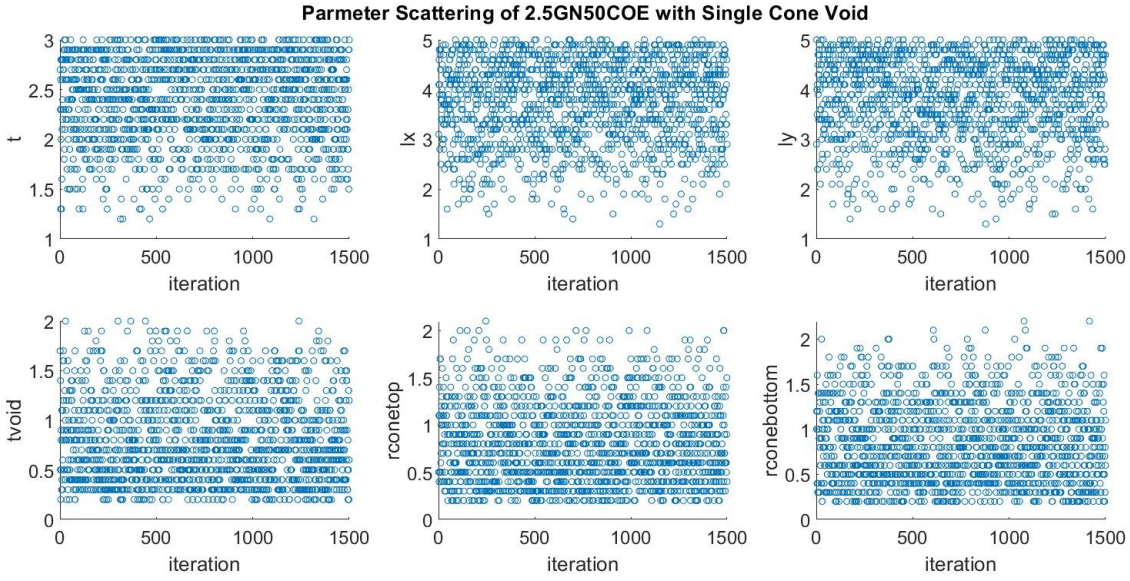

Figure 3-8 Example of parameter scattering in the parameter space showing the control variables of 2.5GN50COE with single cone void that include t: thickness of the absorber, lx: x-length of the unit cell, ly: y-length of the unit cell, tvoid: thickness of the cone, rconetop: radius of the cone at the top surface, and rconebottom: radius of the cone at the bottom surface.

The Monte-Carlo method [251,252] which performs randomized searching all over the parameter space with uniform distribution of parameter points in the space, is one of the algorithms that can provide the optimized solution closest to the global point. The inputs of this method include the iteration number and the initial seed for generating randomized points in the parameters space. In this study, the random number generator U16807 [252] was used to generate the random number between 0 to 1 and scaled up to the range of each parameter to select the random points based on the input iteration number. The constraints such as upper bound, lower bound, and manufacturing resolution were added to the selection criteria to avoid generating the points in the undesired space.

The optimizer was generated in MATLAB and communicated with COMSOL FEA model though Livelink to MATLAB module [253,254]. The generated set of parameters from the optimizer was input in the model automatically and solved for the RL result. The result was analyzed in the same program for maximum RL and BW in each case. These processes were run into the loop with the defined iteration times. The objective functions were compared with the previous solutions and the set of parameters that provide global maxima was selected as the optimized case of the absorber structure. Figure 3-8 visualizes the example of selected points in the space for a single layer structure with conical void inside the absorber slab. The control variables, encompassing parameters like absorber thickness (t), unit cell dimensions (lx and ly), cone thickness (tvoid), and cone radii (rconetop and rconebottom), are subject to this optimization. It can be observed that the iteration point distributes uniformly over the parameter spaces while adhering to the specified constraints.

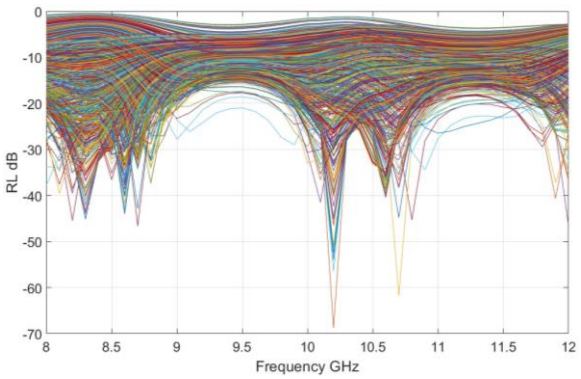

Figure 3-9 Example of the solution from the optimizer for 2.5GN50COE with single cone.

The solutions based on the example case for conical void in an absorber slab are plotted in Figure 3-9. It can be observed that each control variable set provided a different RL to the input EM radiation. The proposed optimizer selects the parameter set that most benefits the provided objective functions. The examples of objective functions include maximizing the RL, maximizing the BW, minimizing the effect of polarization, minimizing the effect of angle of incidence change. In this study, the objective function for maximizing the RL and maximizing the BW at -20 dB were input in the weighting ratio of 1:19 which more focus on broadening the BW.

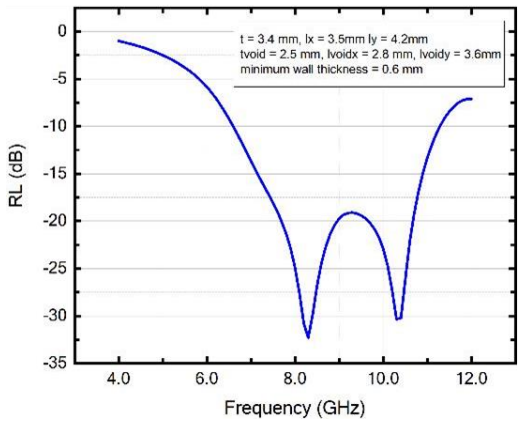

Figure 3-10 RL of the optimized structure taking material intrinsic properties from Song et al. [21] The structure contains a cuboid void inside a unit cell. Parameters in the legend include t: thickness of the absorber, lx: a unit cell lenght in x direction, ly: a unit cell length in y direction, tvoid: void height, lvoidx: void length in x direction, lvoidy: void length in y direction.

The generated optimizer testing results are shown in Figure 3-10. Material intrinsic properties from Song et al. [21] were input into the FEA model of an absorber slab with a single cuboid void in a unit cell. The control variables include t: thickness of the absorber, lx: a unit cell lenght in x direction, ly: a unit cell length in y direction, tvoid: void height, lvoidx: void length in x direction, lvoidy: void length in y direction. The optimized result shows the RL with two combined absorption peaks at -36 dB and -31 dB corresponding to the frequency at 8.2 GHz and 10.3 GHz respectively. This peak combination yields the BW at -18 dB around 2 GHz while BW@10 around 5 GHz at the thickness of 3.4 mm. This result shows a significant improvement from the original material slab reported by Song et. al. [21] as shown in Figure 3-6b.

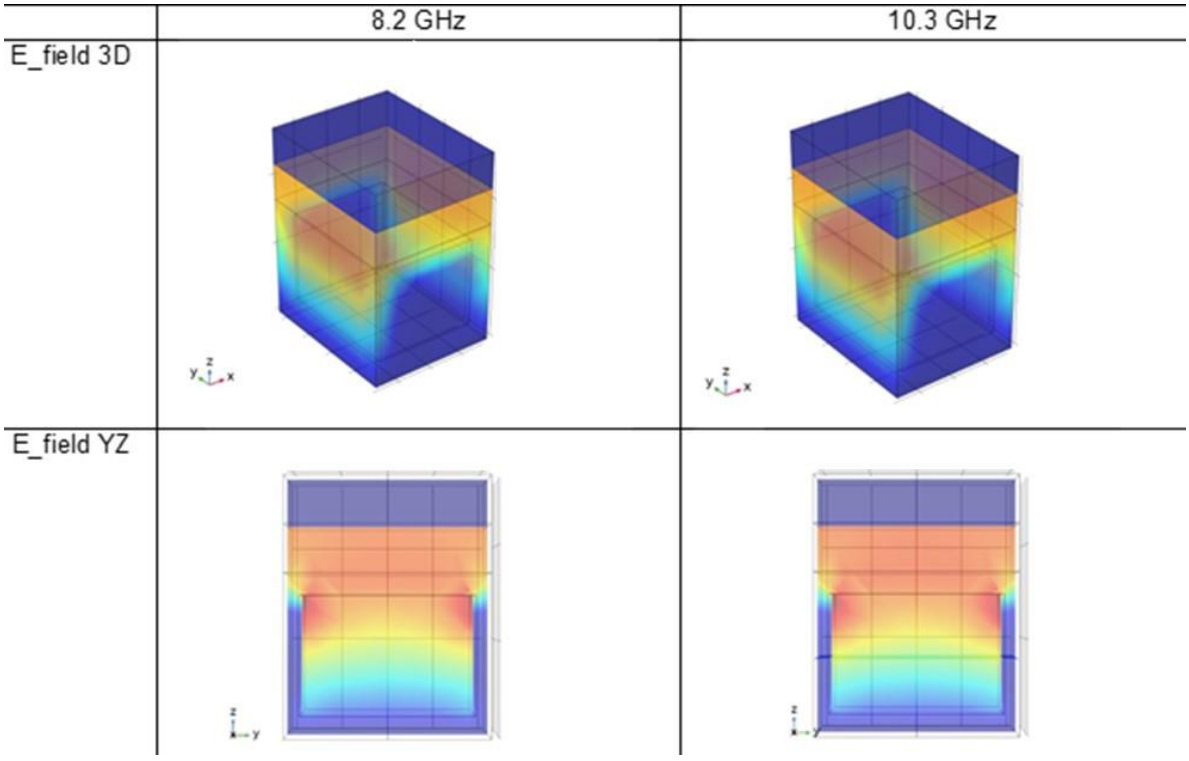

Figure 3-11 Electric Field distribution of the optimized structure taking material from Song et al. at the absorption peak frequencies showing in figure 3-10.

Figure 3-11 illustrates the electric field distribution of the optimized structures at the resonant peaks. It can be observed at both resonant frequencies that there are the electric field enrichments at the top edges of the pore along the x axis which confirms that the resonances

from the void are the main absorption mechanism of this structure as a concept of the metamaterial absorbers. This confirms that applying Monte Carlo approach offers a systematic and randomized exploration, aiming to identify optimized solutions for the electromagnetic absorber design, especially in scenarios involving intricate and non-linear optimization challenges.

3.4.2 Meta-structures Optimization for Solution Mixed 5 wt% PLA/GNPs (5GN)

After the model and optimizer were generated and proved to be applicable for designing the EM metamaterial absorber, they were applied to design various pore structures with the input intrinsic material properties from chapter 2.

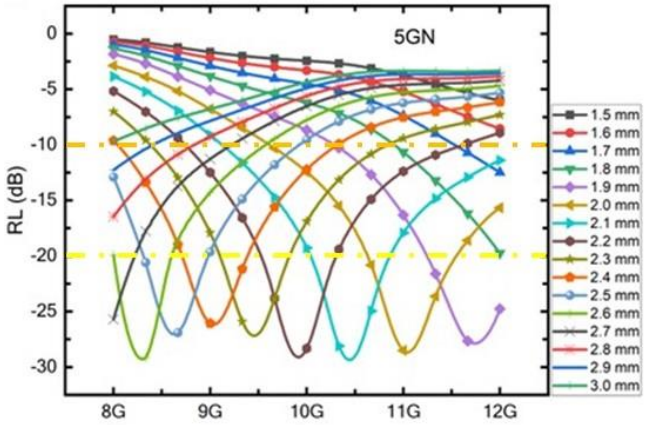

Figure 3-12 RL of 5GN with different thicknesses ranging from 1.5 mm to 3.0 mm.

Figure 3-13 visualizes the optimized RL of each designed structure that was input in the model and optimizer for the material 5GN. Figure 3-13a shows the RL of the single-void structures in a unit cell. In the legend, pillar geometry means geometry is the inversed void, which is material instead of free space and vice versa for the spaces between each pillar. The “Z” symbol in the legend means the pore structure stack on each other in z direction. Figure 3-13b illustrates the RL of the structures that include multiple voids with different pore sizes in a unit

cell. Similar to the single void structure, the “X, Y, Z” represent the direction of the multiple pore alignment in the unit cell.

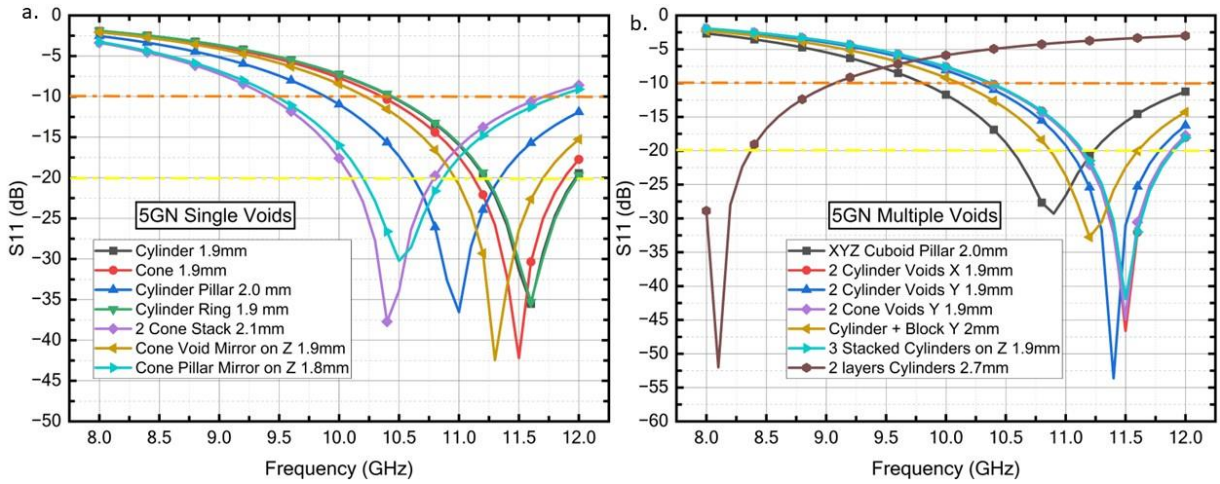

Figure 3-13 RL of the optimized geometries for 5GN containing a. single void in a unit cell b. multiple voids in a unit cell. The legends indicate the pore geometries and thickness of the absorbers.

Compared with the original RL of the bulk absorber shown in figure 3-12, most of the designed meta-structures provide improvement in maximum RL. The highest increase can be observed from -29 dB up to -54 dB for the absorber thickness around 2 mm when adding 2-cylinder voids in the unit cell in y direction. The maximum BW@20 was also broadened from approximately 0.8 GHz to 1 GHz when adding a cylinder pillar inside the unit cell.

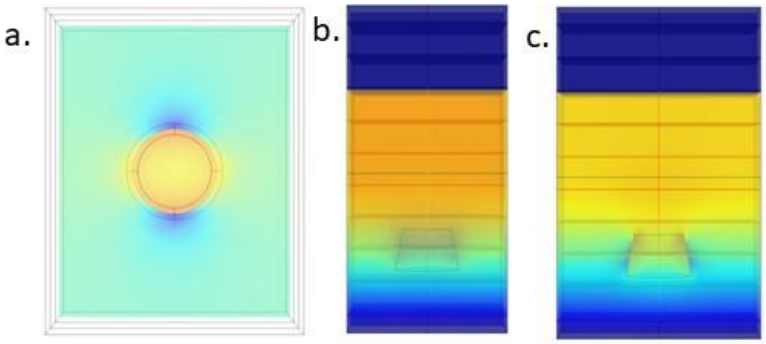

Figure 3-14 Electric field distribution at the resonant frequency for 5GN with optimized single cone void geometry in a. x-y plane b. y-z plane c. x-z plane.

Figure 3-14 visualizes the example of the electric field distribution of the optimized structure which includes one conical void in the absorber slab positioning at the absorption peak

at 11.5 GHz. I can also detect that the electric field was enhanced around the pore interface within the material along the y direction. This enrichment is the result of the resonance from the interactions between repeated structures that provide the absorption as the metamaterial behavior [85,92,94,243]. This non-uniform distribution of the electric field leads to the formation of the dipolar relaxation which enhances the absorption through dielectric loss, ohmic loss, interference, and impedance matching mechanisms [15,85]. Thus, the RL level can be enhanced.

3.4.3 Meta-structures Optimization for Twin Screw Compounded 7.5 wt% PLA/GNPs (T7.5GN)

From chapter 2, T7.5GN is more economical scalable and faster to be fabricated than solution mixing composites due to the twin screw extrusion process. It is also worthy to use this composite for the production of periodic porous metamaterial absorbers.

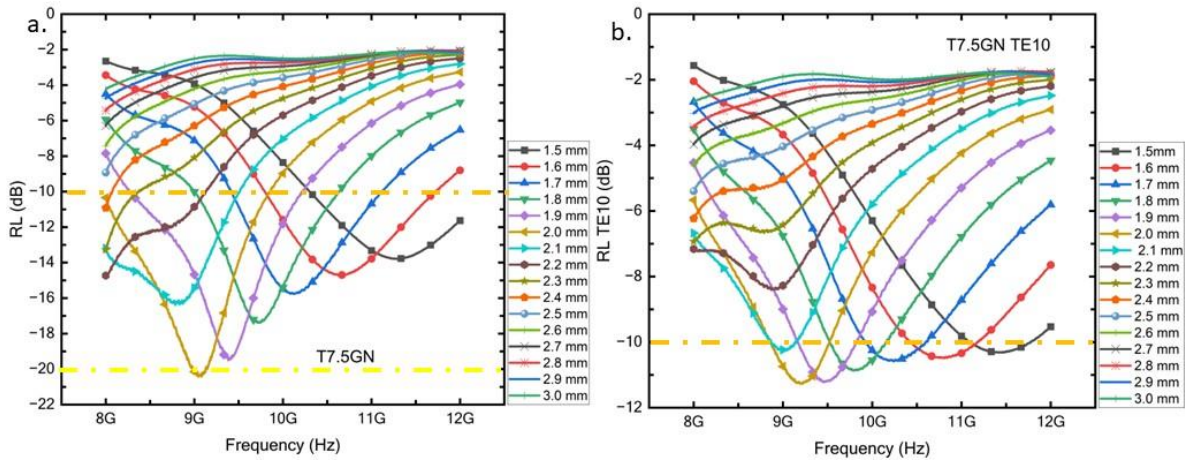

Figure 3-15 RL of T7.5GN with different thicknesses ranging from 1.5 mm to 3.0 mm a. normal incidence b. TE10 mode.

Figure 3-15 displays the RL of the baseline T7.5GN plaque in different thicknesses for both normal incidence (Figure 3-15a) and TE10 mode (Figure 3-15b) as references for comparison with the absorbers containing meta-structures. It can be noted that the highest RL

attained by the bulk composite under normal incidence is -21 dB at a thickness of 2.0 mm with BW@20 of 0.2 GHz, while under oblique incidence, it is -11.3 dB at the same thickness.

Figure 3-16a and 3-16b shows the RL results of the T7.5GN with different meta-structures introduced to the baseline material slab for normal incidence case. The thickness of the optimized structures absorber ranges from 1.9mm to 2.5mm. From Figure 3-16a, the maximum RL can be enhanced up to -67 dB when a single cylinder pore was introduced to the 2.3 mm thick absorber with the BW@20 enhanced to 0.8 GHz. Similar RL improvements from the plaque can be obtained from other pore structures including multiple pores in a unit cell as shown in Figure 3-16b. Moreover, the RL was also enhanced significantly for TE10 mode after adding pore into the unit cell from -11.3 dB to -27 dB with the BW@20 of 0.4 GHz. The outcomes obtained for the TE10 mode can be applied in the fabrication of absorbers. These absorbers, once created, can then be utilized for the purpose of validating measurements in a WR-90 waveguide setup. These results indicate that even the baseline materials that do not provide efficient absorption for the commercial requirements (-20 dB) can also be improved by introducing the porous meta-structure to the material.

Figure 3-17 also shows the example of the electric field distribution of two-cylinder voids structure positioned at the absorption peak at 8.75 GHz. It can be noticed that the electric field enrichment is along x direction which due to the interaction between the unit cell structures while there is no interaction between each void within a unit cell can be observed. Moreover, the resonance density is different between both pores in the unit cell which can be related to the pore size. This result implies that there is a wide space of geometry that can be explored for different resonant modes which results in different absorption behavior depending on the desired objective functions.

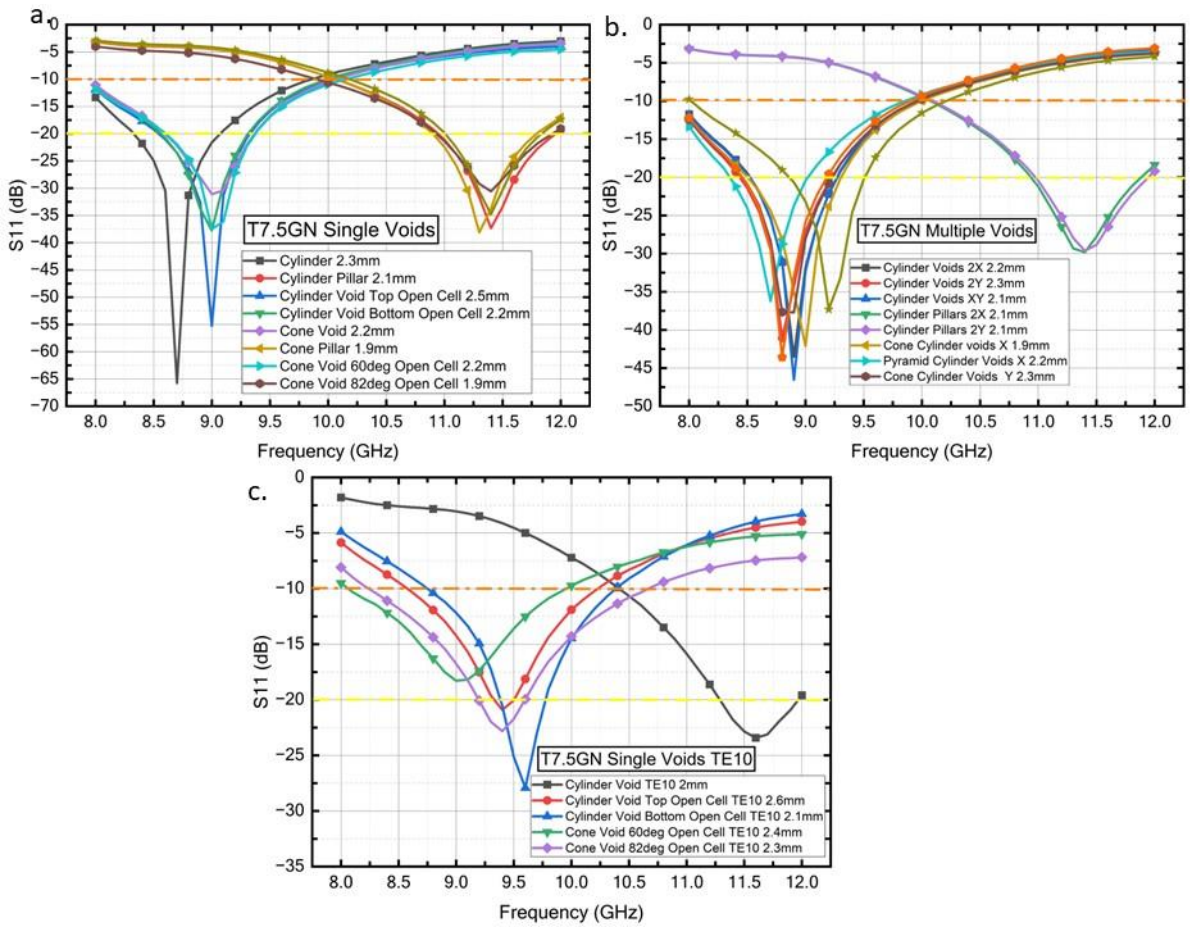

Figure 3-16 RL of the optimized geometries for T7.5GN containing a. single void in a unit cell b. multiple voids in a unit cell c. single void in a unit cell for TE10 mode. The legends indicate the pore geometries and thickness of the absorbers.

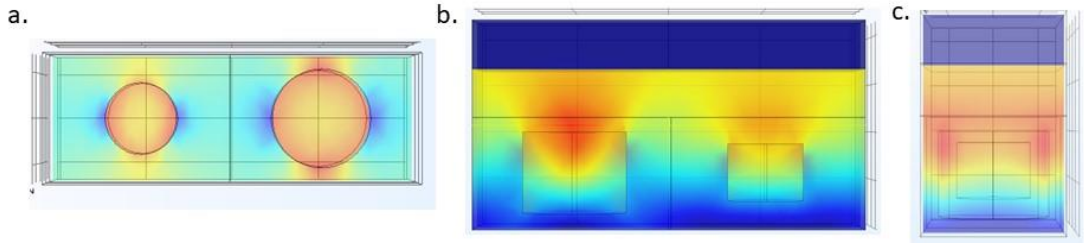

Figure 3-17 Electric field distribution at the resonant frequency for 7.5GN with optimized two-cylinder voids geometry along y direction in a. x-y plane b. y-z plane c. x-z plane.

3.4.4 Meta-structures Optimization for Solution Mixed 2.5 wt% GNPs 50 wt% COE in PLA (2.5GN50COE)

Finally, the meta-structure design technique was applied to the most efficient baseline composite material 2.5GN50COE obtained from chapter 2 which provide absorption peak of -38

dB in normal incidence mode with BW@20 around 0.61 GHz at the thickness of 1.9mm (Figure 3-18a). The maximum RL for TE10 was also obtained from the 1.9 mm thick composite at -19.5 dB with no BW@20 presented (Figure 3-18b).

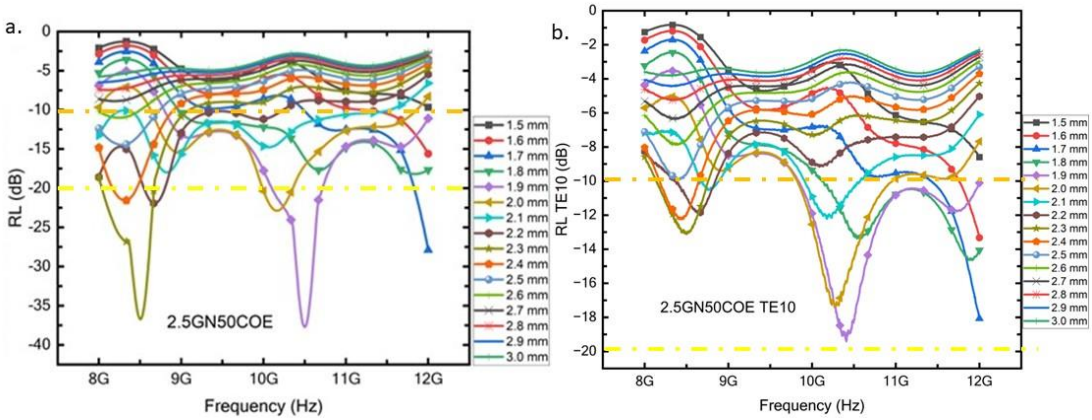

Figure 3-18 RL of 2.5GN50COE with different thicknesses ranging from 1.5 mm to 3.0 mm a. normal incidence b. TE10 mode.

Figure 3-19a shows the RL of the 2.5GN50COE composite after introducing porous structures in the unit cell. The maximum RL can be enhanced to -59 dB after adding a single cuboid void to the 2.0 mm thick slab while the BW@20 can be significantly enhanced to 1.1 GHz or almost twice the value obtained from the bulk material.

Since the introduction of periodic pores in the absorbers provides efficient benefits on the absorption level and bandwidth, further exploration on more complex structures was performed. Inspired from the traditional metamaterial absorbers that consisted of the metallic resonant unit on top of the dielectric materials [15,84,85,88–91,243], the PEC boundary condition was applied on the pore (or pillar) geometries to study the effect of the conductive layer. The results are presented in Figure 3-19b and 3-19c. For normal incidence, the BW@20 can be further enhanced by this method up to 1.5 GHz with the maximum RL of -37dB when the meta-structure consists of truncated cone pillars that contain larger diameter on the top surface with PEC boundary condition was added to 2.2 mm thick absorber. Figure 3-19d shows the RL result for truncated

cone pillars with PEC on top that the cone angles are equal to the countersinking drill bits which are designed for manufacturing capability reason. The example of this kind of structure is shown in figure 3-20 while the PEC layer is highlighted in blue. The most efficient structured found was the truncated cone with the angle of 100° that have the PEC on top surface with 2.3 mm thickness. The BW@20 can be broadened to 1.8 GHz with the maximum RL of -37dB. The meta-structure also benefits the absorption band for TE10 mode of this composite. The BW@20 can be enhanced to 1.5 GHz with the maximum RL of -32 dB. None of the proposed results from meta-structures shows the decrease in maximum RL from the bulk material while the BW@20 was widely improved. This improvement indicates the potential for further improvement of the performance of the EM absorber when metallic layer is introduced in the meta-structure.

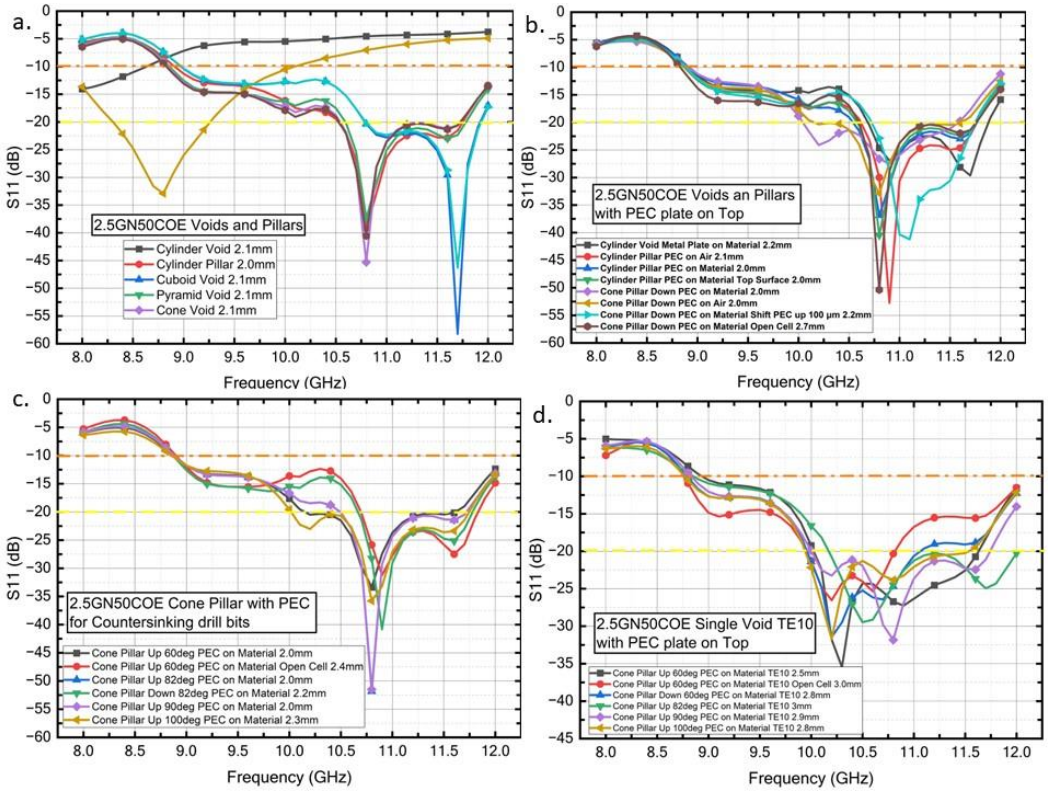

Figure 3-19 RL of the optimized geometries for 2.5GN50COE containing a. simple void in a unit cell b. a void in a unit cell with PEC plate on the top of the geometries c. single cone pillar with PEC on top surface of the cones using the geometries of the countersinking drill bits. d. single cone pillar with PEC on top surface of the cones using the geometries of the countersinking drill bits for TE10 mode. The legends indicate the pore geometry thickness of the absorbers.

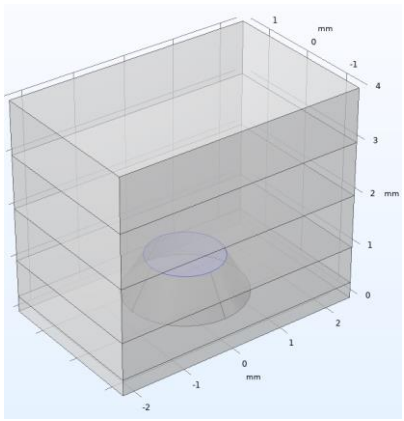

Figure 3-20 The PEC position for PEC on top surface models

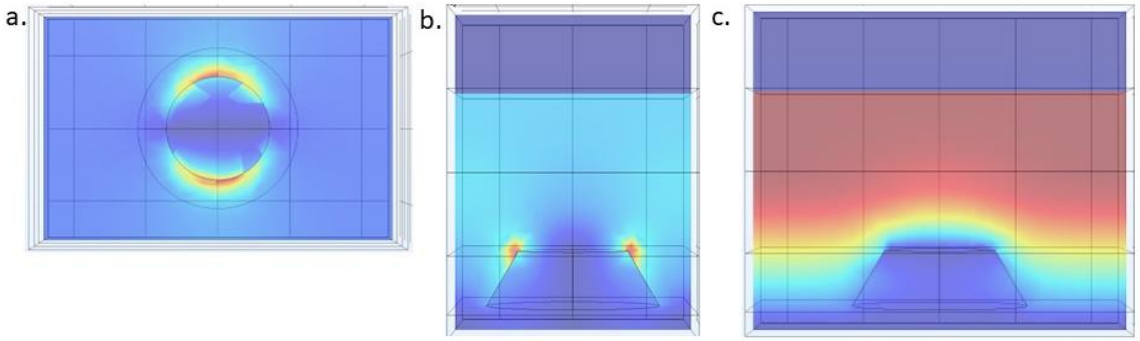

Figure 3-21 Electric field distribution at the resonant frequency for 2.5GN50COE with optimized 60◦ cone pillar geometry with PEC on top surface of the cone. in a. x-y plane b. y-z plane c. x-z plane.

The electric field enhancement is obviously observed around the additional PEC layer on top of the pillar structure as shown in Figure 3-21. The introduction that PEC layer results in charge accumulation around the PEC which acts as the secondary resonant source additionally from the interaction of the periodic meta-structure. Thus, the combination of the resonance peaks extends the absorption bandwidth significantly.

3.5 Conclusions

In this chapter, the computational modelling and optimization techniques were introduced to further enhance the EM absorption of the polymer-based composite based on the design criteria of periodic porous metamaterial structures. The FEA model was constructed based on the method proposed by Bregman et al. [99] . The accuracy of the model was investigated by mesh

refinement and elemental order tests. The model was validated with the existing reported experimental result from Song et al. [255] which providing agreement in trend and peak position while the magnitude of RL is slightly different. Monte-Carlo optimizer was generated to help explore the parameter spaces for meta-structure design with constraints for manufacturing capabilities. The simulation results show the improvement in both maximum RL and operation bandwidth after adding the periodic pores in to the material. The most efficient structure for broadened operation bandwidth obtained in this study is the truncated cone pillar with PEC on the top surface for the 2.3 mm thick 2.5GN50COE that provides BW@20 of 1.8 GHz while the maximum RL is maintained as the original bulk material at -37 dB. This study also provides an efficient method to enhance the RL of the poor absorption composite as T7.5GN from -21 dB to -67 dB for the thickness around 2 mm. The enhancement in both absorption level and operational bandwidth was benefited from the metamaterial behavior that induced from the resonance caused by the interaction between the repeated pores. This resonance can be achieved by tuning the pore size and geometry as well as the unit cell size by using the optimizer. The outlined strategy offers the capability to design and manufacture metamaterial absorbers with superior performance. These absorbers not only demonstrate high RL but also incorporate additional advantages as specified by user-defined weighted objective functions.

Chapter 4 Progress in Manufacturing of Periodic Porous Structure Metamaterial EM Absorbers

4.1 Introduction

In the second chapter of this investigation, polymer-based composites were systematically tailored to exhibit intrinsic properties aligned with the commercial requirement of the RL of -20 dB. This achievement underscores their foundational role as essential materials in the realm of EM metamaterial absorbers. Subsequently, the intrinsic properties from Chapter 2 were leveraged in the computational modeling conducted in Chapter 3. An optimization process was subsequently implemented to ascertain the geometries of periodic porous meta-structures, thereby enhancing overall absorbing performance. The production of physical products for the metamaterial absorbers constituted the next step, involving the integration of the designed composite materials with the optimized periodic porous structures. Different manufacturing techniques were applied to the pre-engineered composite materials discussed in Chapter 2, facilitating a comprehensive comparative analysis.

Numerous existing reports detail various manufacturing techniques for the production of periodic porous structures absorbers. For instance, one approach involves pre-manufacturing bulk composites as the initial material, followed by machining through conventional Computer Numerical Control (CNC) machines to create arrays of repeated pores [98]. Additionally, additive manufacturing techniques, derived from pre-compounded composites, have been employed to design intricate repeated structures [77,78,95,241,242]. Integrated techniques have also been proposed, such as the pre-printing of honeycomb structures from baseline polymers,

followed by the coating of conductive constituents [87,93]. Furthermore, Yuan et al. [79] introduced a complex manufacturing technique where the commercial Nomex honeycomb precursor, comprising poly(m-phenylene isophthalamide) (PMIA), was pyrolyzed into conductive carbon fibers/polymer composites before depositing reduced graphene oxide on the surfaces. Each of these examples presents conductive porous structures suitable for EM absorber applications.

This chapter provides a summary of our advancements in manufacturing techniques for the fabrication of periodic porous structures using the designed baseline composites. The discussion unfolds in three main sections. Firstly, the simplest technique involving material subtraction from molded bulk composites utilizing a conventional CNC machine is explored. Secondly, an examination of additive manufacturing, specifically in terms of Fused Deposition Modelling (FDM), is presented. This section delves into the production of filaments and investigates the properties of the printed products. Lastly, the chapter reports on the compression molding of meta-structures using pre-manufactured molds.

The evaluation of these manufacturing techniques incorporates optical observations to assess accuracy and resolution. These observations serve as crucial benchmarks for establishing constraints in the optimization process and guiding future work in composite design.

4.2 Meta-Structures Manufactured by CNC Machining

4.2.1 Experimental

The primary method employed for manufacturing the meta-structures involves the subtraction of material from pre-molded bulk composites. In this investigation, the T7.5GN composite served as the baseline material, chosen for its advantages in the twin-screw extrusion technique, which offers a higher production rate compared to the solution mixing method. The

compression molding method applied to these composites has been previously detailed in Chapter 2.

To create the desired structures, bulk samples, sized to WR-90 waveguide dimensions (22.86 mm x 10.14 mm), were ground to the specified thickness. Subsequently, cylindrical pores were machined into the samples using a CNC machine. The machining parameters, including a spindle speed of 2000 rpm, peck machining at 0.5 mm/step, a feed rate of 50 mm/min, and the array size, were established using the array program. For cylindrical pores exceeding a diameter of 2.5 mm, a milling program was applied to generate a flat bottom hole. For pores with a diameter less than 2.5 mm, drill bits were utilized to create holes of specific sizes. In instances requiring closed-cell structures, a composite slab was applied to seal the cylinder cell atop the sample using Chloroform (Sigma-Aldrich, Inc., USA) for material bonding. The resulting structures underwent optical observation using an Olympus optical microscope.

4.2.2 Resulted Structures

Table 4-1 Geometrical parameters of the fabricated T7.5GN metamaterial structures from CNC machine

Parameters (mm)	**Sample 1**	**Sample 2**	**Sample 3**	**Sample 4**
X Array	5.7	4.5	1.6	4.6
Y Array	5.1	3.4	1.5	5.0
Pore Dept	1.4	2.0	1.2	1.5
Pore Diameter	4.6	2.8	1.0	2.0
Thickness	2.5	3.0	2.3	2.5

In this investigation, four distinct cylindrical meta-structures, as detailed in Table 4-1, were manufactured for comprehensive characterization. Each of these structures was derived from the optimization process elucidated in Chapter 3. Specifically:

Sample 1: This structure features open cylinder cells on the bottom surface of the composite slab and was optimized for TE10 mode.

Sample 2: Characterized by open cylinder cells on the top surface of the composite slab, this structure was designed to operate in TE10 mode.

Sample 3: This structure comprises cylinder pores situated in the middle of the slab and was optimized for normal incidence.

Sample 4: Featuring cylinder pores in the middle of the slab, this structure was optimized for TE10 mode.

The optimized RL responses for each of these structures can be referenced in Chapter 3 for a comprehensive understanding of their electromagnetic absorption properties.

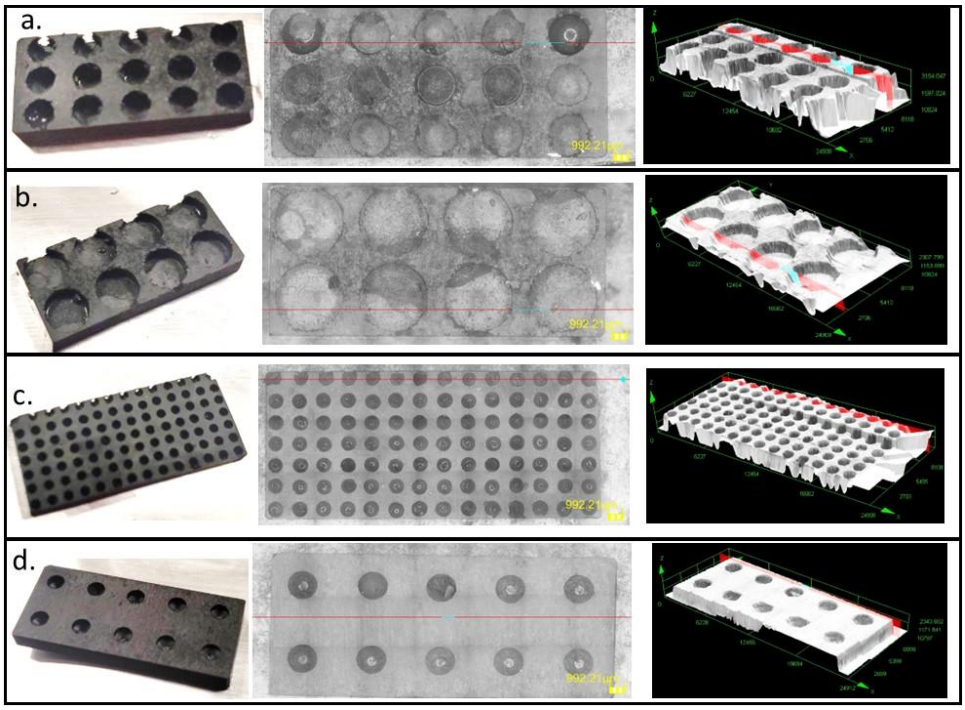

Figure 4-1 The produced meta-structure from T7.5GN with Cylinder pores a. Sample 1 b. Sample 2 c. Sample 3 d. Sample 4

Figure 4-1 provides visual representations of the resulting samples. The first column showcases photographs of the manufactured samples, offering a macroscopic view of their physical appearance. The second column displays top surface images captured through an

Olympus optical microscope. The last column depicts 3D scans of the structures obtained using the Olympus optical microscope.

Upon analysis of the results, several defects become apparent across all manufactured samples. Notably, crack formations in the cell walls on the side surfaces of the samples are observed, attributed to misaligned surfaces during the manufacturing process. The CNC machine movement deviated from the designed positions of the pore arrays, leading to errors in pore alignment. In the case of sample 3 and sample 4, discrepancies in hole depths were noted, caused by non-flat drill bit heads that resulted in the formation of conical shapes at the bottom of the holes. Additionally, a step on the top surface of material was detected in the 3D scanning of sample 3, potentially attributed to measurement errors. It is noteworthy, however, that this step is not visually apparent in the samples themselves.

Importantly, these observed defects are on the order of magnitude comparable to the wavelength (30mm at 10GHz), suggesting a potential impact on the RL response. Further investigation into these defects and their implications on EM properties is warranted.

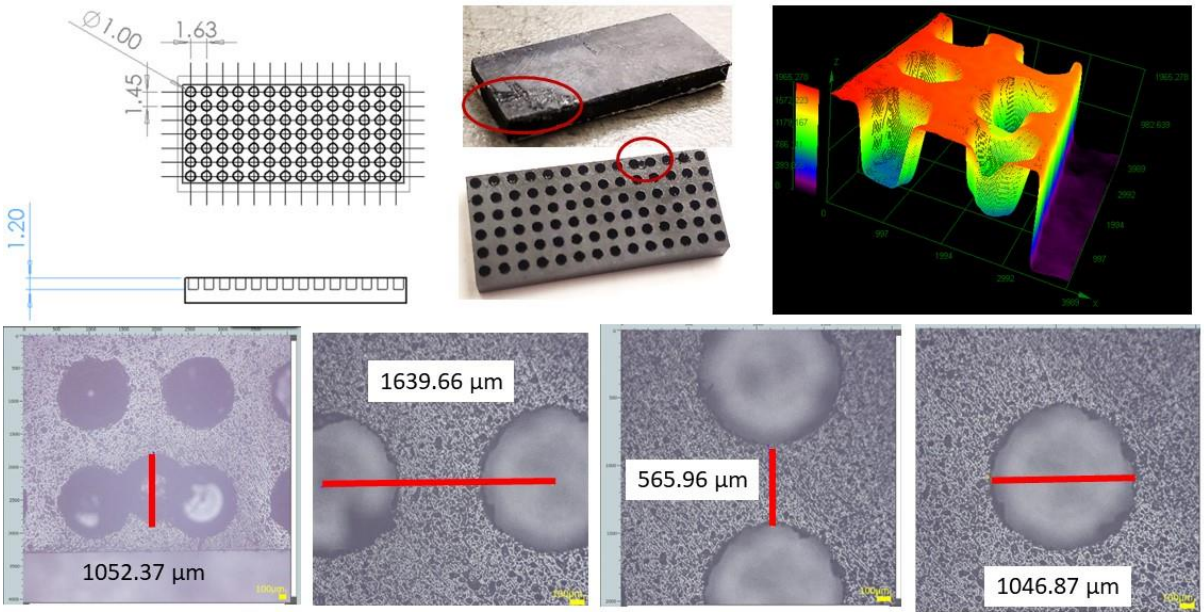

Figure 4-2 The fabricated sample 5 for T7.5GN close cell cylinder pores optimized for normal incidence.

To investigate the sensitivity of manufacturing errors on the absorption performance, a meticulous remanufacturing process was employed for Sample 3, resulting in the creation of Sample 5. Notably, the diameter of the pore, pore depth, and array sizes were accurately reproduced, maintaining a tolerance within 0.2 mm of the design specifications. Additionally, careful attention ensured that the cell walls remained undamaged in this remanufactured sample.

Despite these efforts, a persistent defect within the structure, identified within the red circle in Figure 4-2, was still detected. This flaw necessitates further consideration in understanding its potential impact on the electromagnetic properties of the structure. Sample 5, with its refined manufacturing precision, was subsequently utilized for characterizing the scattering parameters. This characterization serves as a basis for comparing modeling results with the corresponding measurement outcomes, facilitating a comprehensive evaluation of the structure's electromagnetic shielding performance.

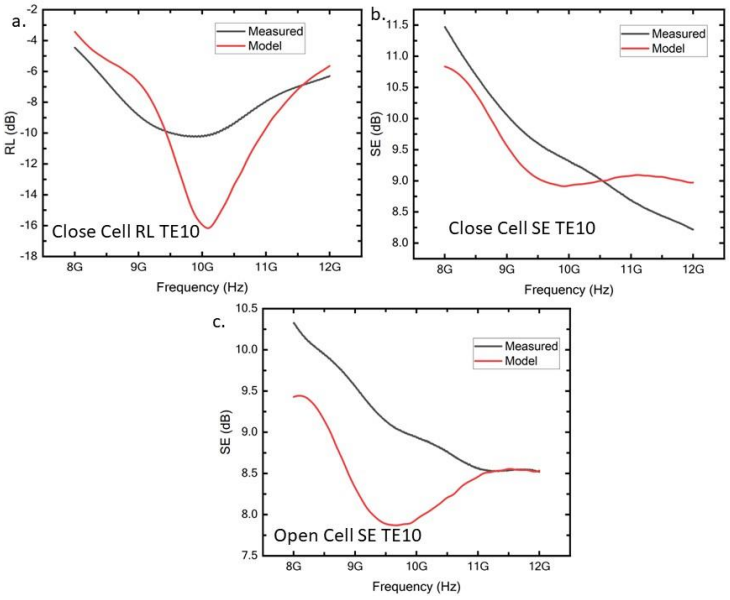

Figure 4-3 Comparison of the scattering parameters between measurement and modelling of Sample 5 in term of RL and SE of the fabricated Sample 3 structure in TE10 mode a. RL of the of the close cell b. SE of the close cell c. SE of the open cell.

In order to ascertain the congruence between the manufactured Sample 5 and modeling outcomes, the VNA was employed to measure the scattering parameters, specifically S11 and S21, for subsequent comparison with the modeling results. Reflecting the model's configuration, silver paint was applied to the back of the absorber to represent the PEC layer in the experimental setup. For the SE results, the material slab was directly introduced into the VNA. Notably, "open cell" denotes the manufactured meta-structures without bonding the top slab to close the pores.

Figure 4-3 depicts the comparative analysis between the measured RL and SE, juxtaposed against the modeled results. Evidently, discrepancies are observed, which can be attributed to the manufacturing errors delineated earlier. Nevertheless, noteworthy trends in both measured SE and RL exhibit a general alignment with the modeling outcomes, albeit with discernible variations.

These findings not only underscore the significance of addressing manufacturing errors but also provide crucial insights for future endeavors. The observed trends furnish valuable guidance for optimizing manufacturing parameters and constraints during computational modeling, necessitating a nuanced consideration of potential errors in the manufacturing process.

4.3 Fused Deposition Modelling (FDM)

Additive manufacturing has emerged as a promising technique, offering swift adaptability to design modifications by enabling the creation of intricate topological architectures without the need for pre-molding. Among these additive manufacturing methods, fused deposition modeling (FDM), commonly known as 3D printing, stands out as a straightforward yet powerful approach. This method involves the melt extrusion of filament materials through a

heated nozzle, facilitating layer-by-layer deposition on a platform. Consequently, FDM proves to be a versatile method for the production of complex metamaterial structures in our study.

However, to harness the full potential of FDM for the fabrication of metamaterial absorbers, a thorough exploration and optimization of processing parameters are imperative. This research delves into the FDM fabrication of conductive composites as a foundational material, aiming to elucidate the factors influencing the conductivity of these composites. The insights gleaned from this study serve as valuable guidelines, paving the way for the future production of periodic structure metamaterial absorbers utilizing the FDM technique. This exploration contributes not only to the advancement of FDM-based manufacturing processes but also to the broader landscape of metamaterial research and design.

4.3.1 Experimental

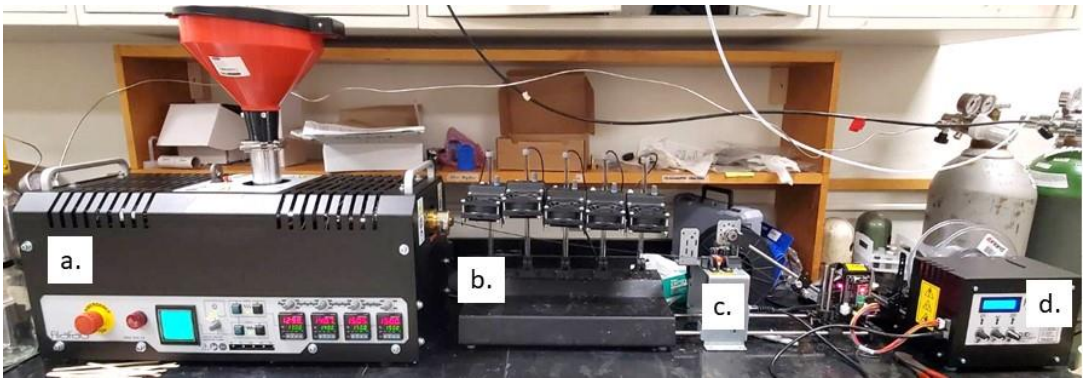

Figure 4-4 Filament Extruder set up a. the extruder b. the cooling station c. pulling station d. spooling station.

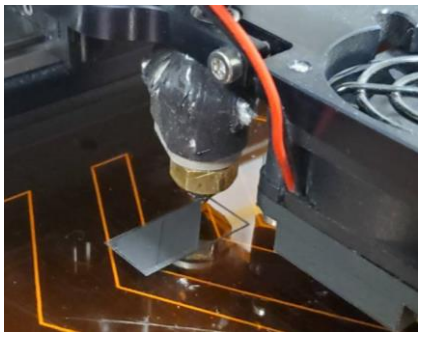

Figure 4-5 FDM of the fabricated PLA/GNPs filament.

The fabrication process commenced by obtaining composite pellets through the twin-screw extruder, utilizing the processing parameters detailed in Chapter 2. Following the twin-screw compounding process, the resulting strand exhibited a diameter of approximately 2.6 ± 0.4 mm, subsequently cut into pellets with a length of 2.8 ± 0.1 mm. The composite pellets, comprising Poly(lactic acid) (PLA) and Graphene Nanoplatelets (GNPs) at concentrations of 5 wt%, 7.5 wt%, and 10 wt%, were then introduced into a single-screw extruder (Filafab).

The extrusion process utilized two temperature stages in the extruder: 145 ◦C followed by 155 ◦C, as depicted in Figure 4-4a. The extruded strand, emerging from the pulling station (Figure 4-4c), traversed through the cooling stage (Figure 4-4b) to solidify the filament and regulate the diameter of the extruded strand. Subsequently, the filaments underwent measurement using a laser sensor, providing feedback to control the spooling speed in the spooling station (Figure 4-4d). This control and monitoring of the extrusion process contributes to the precision and quality of the resulting filaments, ensuring consistency in diameter and overall material characteristics.

The resultant filament underwent a pulling and winding process before being fed into the 3D printer, specifically the MakerGear M2, as delineated in Figure 4-5. The printer's nozzle size was set at 2.5 mm. Uniform printing conditions were maintained across all concentrations, encompassing a printing temperature of 230 ◦C, a printing speed of 1000 mm/min, an extrusion flow rate multiplier of 1.2, a line width of 0.2 mm, and a layer thickness of 0.1 mm. This standardized printing protocol ensures consistency and comparability across the fabricated specimens, facilitating an accurate assessment of the impact of graphene nanoplatelet concentrations on the printed structures.

The extruded filaments from the single-screw extruder exhibited a diameter of approximately 1.4 ± 0.3 mm, subsequently cut into 30 mm lengths for density and DC electrical conductivity assessments. For these measurements, all plaque specimens were uniformly cut to dimensions of 22.9 mm x 10.1 mm x 3 mm.

Density determination was executed by measuring the specimen's dimensions and weight, allowing for the precise calculation of density. The DC conductivity measurement adhered to the methodology expounded in Chapter 2, ensuring consistency and comparability with previously established parameters. These measurements contribute to a comprehensive understanding of the material properties, crucial for evaluating the effectiveness of the fabricated composite filaments for subsequent applications.

4.3.2 Experimental Results

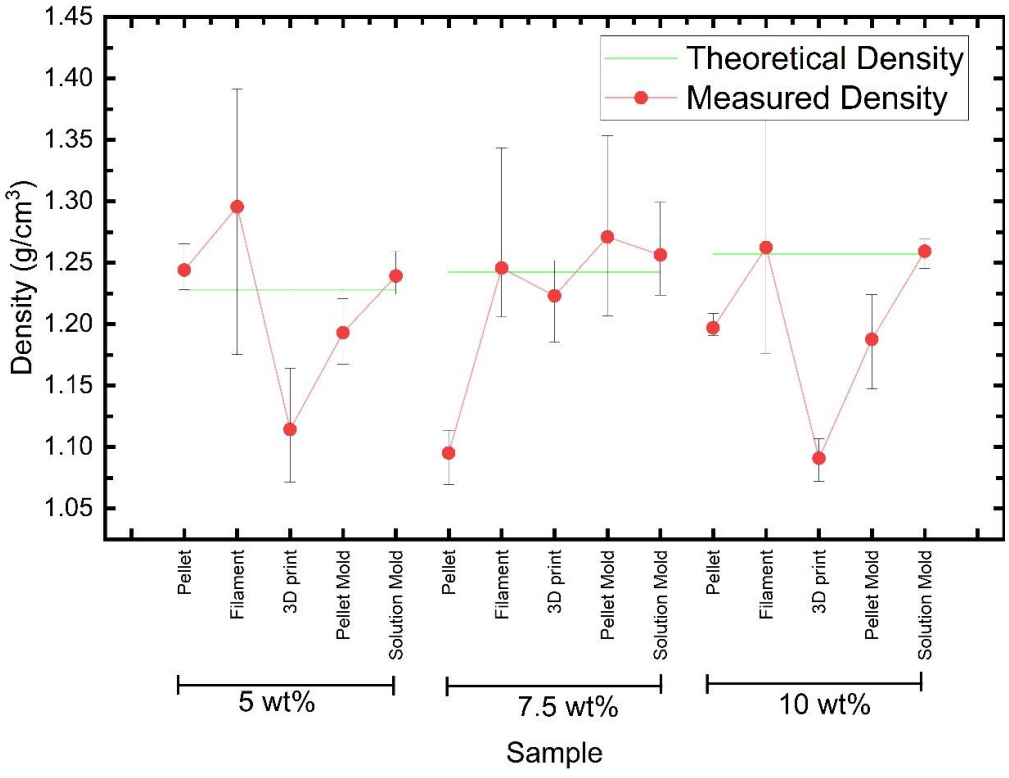

Figure 4-6 The density of the fabricated composites in different phases including pellets, filament, and 3D printed parts compared with compression molded composites and solution mixed composites adapted from [230].

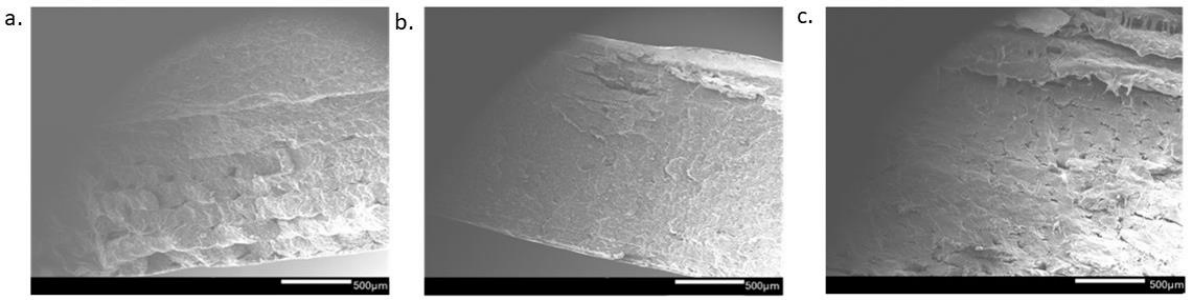

Figure 4-7 SEM micrograph of the 3D printed PLA/GNPs composite a. 5wt% b. 7.5wt% c. 10wt% adapted from [230].

The resulting densities are shown in figure 4-6. The densities of pellets, filaments, and 3D printed composites were compared with the compression molded composites from grounded pellets (Pellet mold) and solution mixing powders (solution mold). The processing parameters for pellet mold and solution mold composites were already discussed in Chapter 2. The flat green lines represent the theoretically calculated densities, determined using the rule of mixture. A consistent density trend is evident across all concentrations, with the exception of 7.5 wt%. Notably, there is a discernible increase in filament density compared to the starting pellets for all loadings. This observed phenomenon is attributable to the heightened crystallinity of the PLA, induced by the shear stress encountered during the thermal extrusion process [256–258]. The augmentation in crystallinity is a key factor contributing to the observed density variations in the fabricated filaments across different concentrations. The density of the 3D printed plaque decreases from the filament. This is due to the porosity gaps between printing lines and layers [259–262].

Figure 4-7 depicts SEM micrographs of the printed composites. Notably, gaps resulting from unfused material between layers are observable. It is essential to highlight that all printed samples were produced under the same printing conditions, which were not optimized for achieving the most effective bonding between the extruded lines. Consequently, the observed gaps between layers underscore the need for further refinement and optimization of the printing

parameters to enhance the overall structural integrity and cohesion of the printed composite materials. Thus, the 3D-printed composites show significantly lower density than the compression molded samples represented in pellet mold and solution mold samples. The optimal printing parameters will be determined in future work. The discussion for the density trend for pellet mold and solution mold composites were already presented in the published work [230].

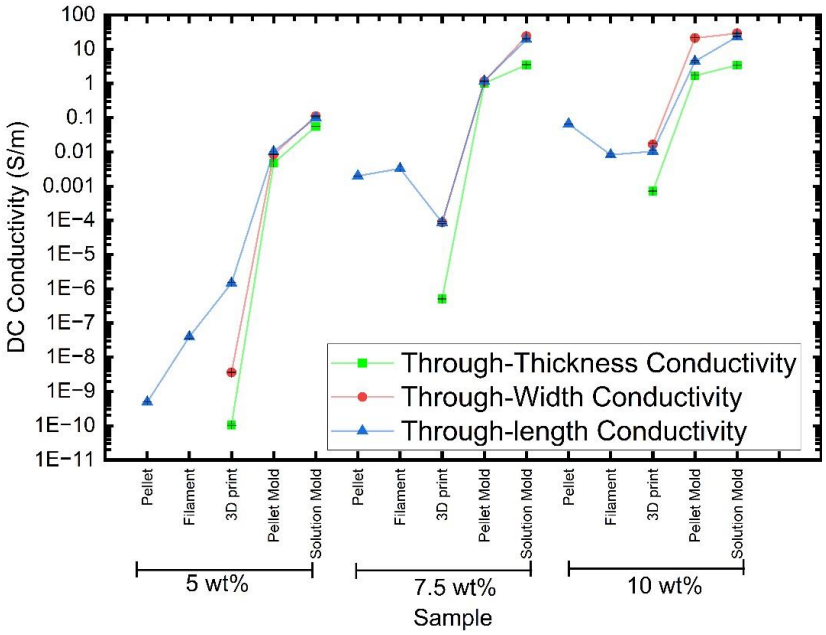

Figure 4-8 The DC conductivity of the fabricated composites in different phases including pellets, filament, and 3D printed parts compared with compression molded composites and solution mixed composites adapted from [229].

Figure 4-8 illustrates the measured DC conductivity of the produced composite in each direction. Consistently, with the same fabrication method, the conductivity exhibits an ascending trend from 5 wt% GNPs to 7.5 wt% GNPs to 10 wt% GNPs, aligning with the rule of mixture. Furthermore, each loading demonstrates a conductivity trend that correlates with the density, except for the pellet and filament of 10 wt% GNPs. The observed drop in conductivity of the filament compared to the pellets presents an intriguing reverse which can be attributed to the agglomeration which occurs at higher concentration. In contrast, for the remaining concentrations, the increase in conductivity is attributed to the shear alignment facilitated by the

extrusion process. This alignment enhances the contact area between GNPs flakes within the composite, contributing to the overall conductivity improvement [256,263]. The nuanced relationship between fabrication processes, material morphology, and resulting electrical properties underscores the complexity of optimizing composite materials for specific applications. Further studies will be instrumental in elucidating the underlying mechanisms and refining the understanding of these intricate interactions.

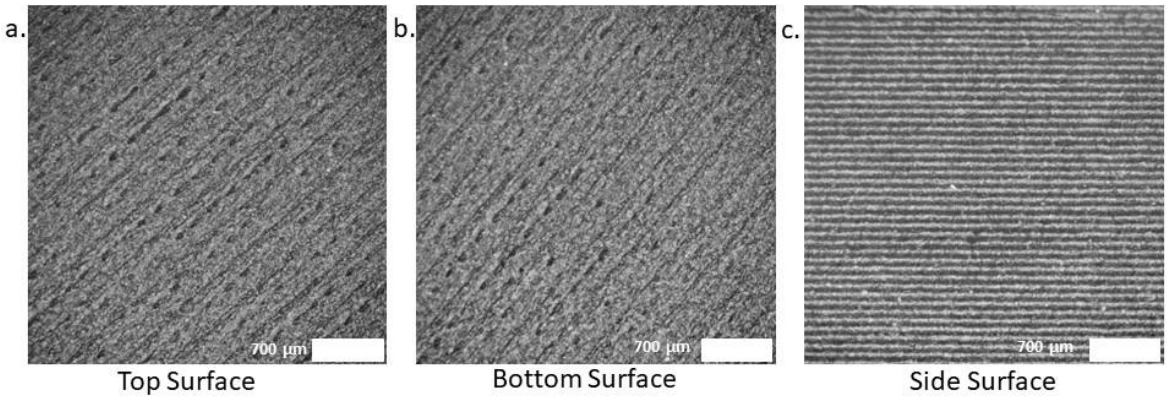

Figure 4-9 Optical microscopic images for the 3D printed 10wt% GNPs/PLA composites a. on the top surface b. on the bottom surface which was contacted with the printer bed c. on the side surface

The observed differences in conductivity along each direction are ascribed to the anisotropic effect induced by FDM. Notably, a substantial increase in conductivity is evident from the through-thickness to through-width to through-length directions in 3D printed samples as depicted in Figure 4-9. This phenomenon is attributed to the shear-force alignment of graphene along the printing path, as discussed in prior studies [264]. Moreover, the presence of air spaces and pure polymer layers between the printed layers emerges as a primary factor contributing to the comparatively lower through-thickness conductivity, as illustrated in Figure 4-7 and Figure 4-9c. These interactions emphasize the multifaceted nature of electrical conductivity in composite materials, emphasizing the importance of considering fabrication processes and material morphology for achieving desired anisotropic properties. The discussion

about the comparison of the DC conductivity of the compression molding composites were already report in the published work [230].

From the results, it can be concluded that there is room for processing parameter optimization to achieve the desired level of conductivity suitable for EM absorption applications in the future works.

4.4 Meta-Structures Manufactured by Compression Molding

4.4.1 Experimental

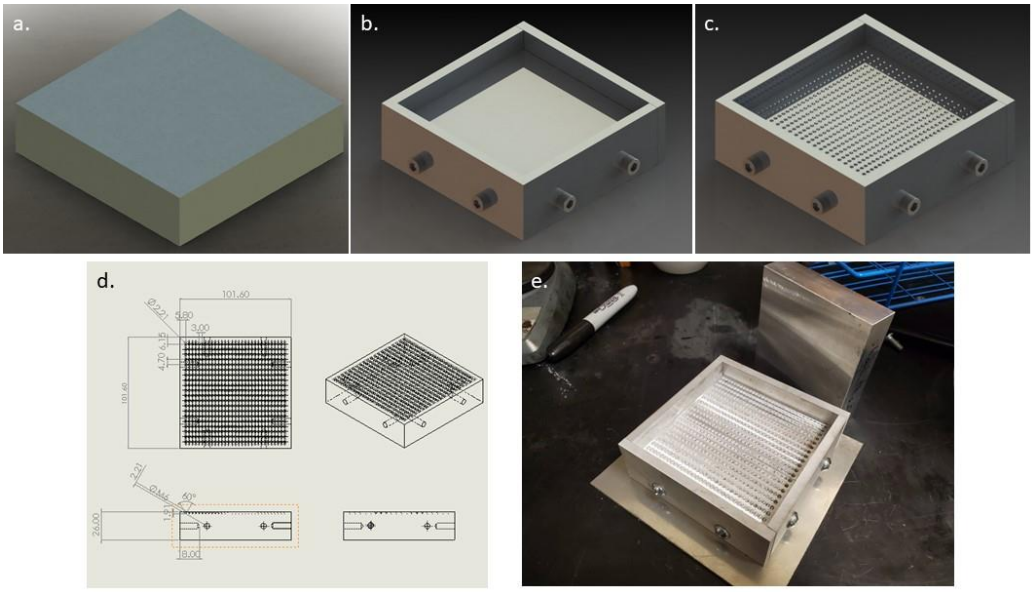

Figure 4-10 Mold components and design a. the top plunger part, the bottom part assembly c. the meta-structure machined on the bottom part surface d. the CAD design of the mold e. the physical fabricated mold.

The third method for fabricating periodic porous metamaterial absorbers, utilizing the composites detailed in Chapter 2, involves the application of compression molding with pre-designed structural molds. This technique enables the replication of intricate and predefined structures, ensuring the production of metamaterial absorbers with specific geometric configurations.

In this study, the optimized structures of periodic truncated cone pillars derived from computational modeling results (Chapter 3) were manufactured. These structures were specifically crafted from the baseline composite 2.5GN50COE. The design of the truncated cone structures was informed by the angles associated with commercially available countersinking drill bits. Notably, this chapter employs the optimized structures for tools with angles of 60° for normal incidence and 82° for TE10 mode to design the molds, aligning with the specific requirements dictated by the EM angle of incidence modes under consideration.

The process of mold fabrication commenced with the design of a 4" x 4" mold, featuring arrays of conical holes with countersinking angles, using Computer-Aided Design (CAD) software (SolidWorks). The spacing between these holes corresponds to the optimized structures obtained from Chapter 3. Subsequently, the mold was meticulously machined using a CNC system on raw aluminum materials. This mold comprises a bottom part housing the machined meta-structures, a top part functioning as plungers, and four side panels securely fastened to the bottom part. The machined patterns of the meta-structures were subject to thorough inspection through the lens of an Olympus optical microscope, ensuring precision and fidelity to the intended design. This quality control step is imperative to validate the accuracy and integrity of the fabricated molds, essential for producing metamaterial absorbers with the desired EM absorption.

The compression molding process was carried out using a hot press (Carver). Teflon mold release (3M) was pre-applied to the mold before the operation. The sequence of operations involved loading the composite powders into the mold, followed by the assembly of the mold components. A vacuum bag was placed over the mold set up which was connected to the vacuum pump to remove the porosity during the compression molding. The mold assembly was

prepressed at 1.5 MPa for 20 minutes to densify the powders before releasing the pressure. The pressure was applied in a step of 0.2 MPa gradually starting when the temperature reached 150˚C. The set up was dwelled at 160˚C for 15 minutes before cooling down automatically to the room temperature. The samples were demolded and cut into the WR-90 sample size for characterization.

4.4.2 Manufacturing Results

Table 4-2 The optimized geometries obtained from the optimizer for each case.

Parameters (mm)	**60˚ Normal Incidence**	**82˚ TE10**
X Array	4.7	21.5
Y Array	3.0	9.5
Cone Dept in the Mold	1.9	3.3
Truncated Cone Thickness	0.7	1.6
Cone Radius on the Bottom	1.1	2.9
Base Thickness	0.3	1.0
Top Slab Thickness	1.1	0.4

Table 4-2 lists the geometrical parameters of the optimized meta-structures for the absorber contain 60˚ truncated cones for normal incidence and 82˚ truncated cones for TE10 modes that were obtained from chapter 3. This data was used as the reference for the fabricated molds and absorber samples.

The dimensions of the meta-structures machined mold of 60˚ truncated cones for normal incidence are shown in Figure 4-11. It can be observed that the spacing between the unit cells in both X and Y directions are close to the design values within 0.05 mm tolerance. However, the depth and the diameter of the holes contain large errors from the design parameters. Further optimizations of the CNC machining operation and manufacturing parameters are needed to improve the mold geometries with tighter tolerance.

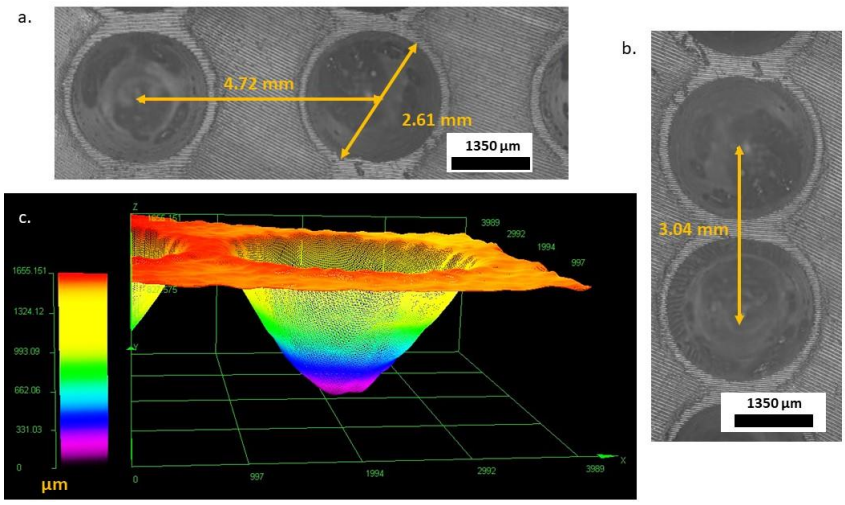

Figure 4-11 The measured mold geometry for optimized meta-structure consist of periodic arrays of 60° truncated cone for normal incidence absorption mode a. X spacing between unit cells b. y spacing between unit cells c. the dept of the cone hole drilled by CNC machine.

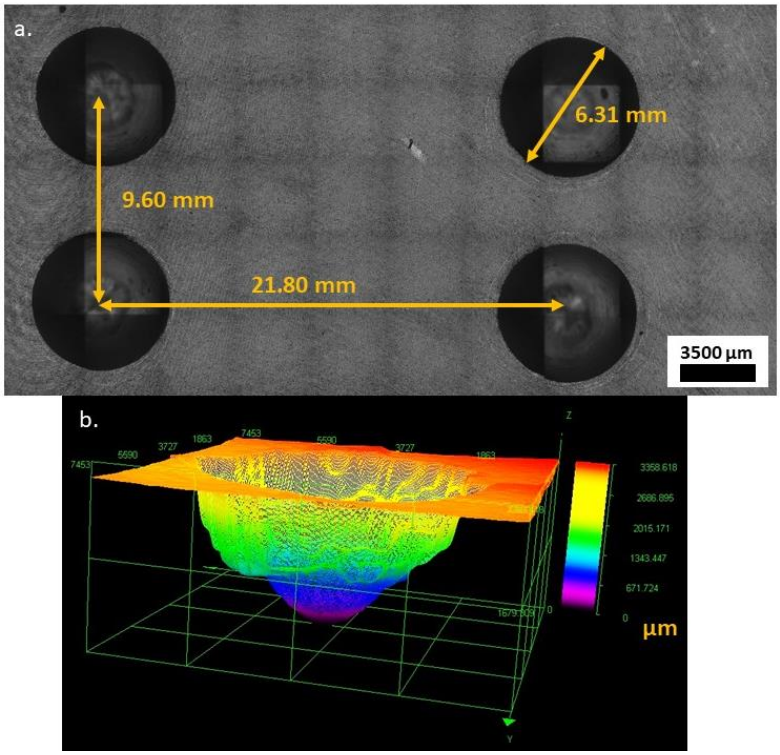

Figure 4-12 The measured mold geometry for optimized meta-structure consist of periodic arrays of 82◦ truncated cone for normal incidence absorption mode a. X spacing between unit cells and y spacing between unit cells b. the dept of the cone hole drilled by CNC machine.

The dimensions of the meta-structures machined mold of 82° truncated cones for TE10 are shown in Figure 4-12. All dimensions obtained from the fabrication shows close tolerances

with the design value with the largest difference of 0.3 mm. However, the optimization of the CNC machining operation and manufacturing parameters is still needed to improve the mold geometries with tighter tolerance.

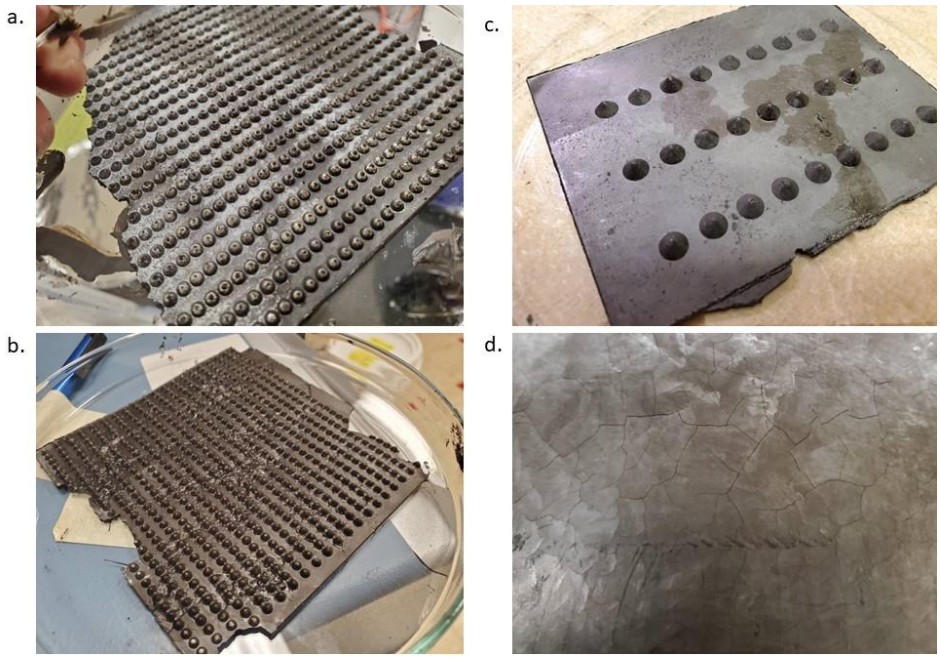

Figure 4-13 Fabricate 2.5GN50COE composites from the manufactured molds a. sample1: 60° truncated cone for normal incidence b. solvent bonded cracks of sample1 c. sample2: 82° truncated cone for TE10 mode d. back of sample1.

Figure 4-13 illustrates the compression molded composites from the fabricated molds. Sample1 represents the composite with the meta-structure of 60° truncated cone for normal incidence while Sample2 represents the composite with the meta-structure of 82° truncated cone for TE10 mode. Sample1 shows excessive cracks after demolding which are distributed all over the samples (Figure 4-13a and 4-13d). All cracks are located on the flat area between the cones. It can be assumed that the cracks are caused by the residue stress during the cooling process induced by the meta-structure. The pulling force from the contraction was applied to the composite in the flat area between the cones which are constrained by the mold. Further investigation is needed to evaluate the reason for the fracture. It can also be noted that bonding the crack by solvent (Chloroform) does not fuse the material completely and cracks still occur

(Figure 4-13b). Only a part of Sample2 was eligible to be used for further EM absorption characterization in the future work. However, minor porosities can still be observed on the surface of Sample2. This result indicates that compression molding process optimization is still needed to achieve the higher quality of the EM absorber samples.

4.5 Conclusions

This chapter has presented advancements in exploring potential composite manufacturing techniques applicable to the fabrication of periodic porous metamaterial absorbers. The first technique involves post-processing through CNC machining of pre-molded bulk composites. Results indicate the method's capacity for high precision and operational simplicity, with potential for future refinement through adjustment of a few CNC machining parameters to attain high-quality samples. However, the method's capability to accommodate complex meta-structures may be limited. In contrast, the second method, utilizing FDM additive manufacturing, offers an avenue to tailor the complexity of structures. Yet, optimization of processing parameters for both filament extrusion and FDM is essential to achieve desired material properties suitable for EM absorber applications. The third method demonstrates potential for large-scale production of metamaterial absorbers. Tolerances in the fabricated absorber dimensions primarily depend on CNC machining during mold fabrication. However, optimization of the compression molding process is still required to mitigate potential fractures. In summary, while each proposed method shows promise, further enhancements are crucial to achieve the desired properties of the designed absorbers. Adjustments and optimizations in processing parameters, mold fabrication, and compression molding are imperative for the successful realization of high-quality metamaterial absorbers.

Chapter 5 Conclusion and Future Works

5.1 Conclusion

The rapid expansion of high-speed electronic and wireless technologies necessitates the development of high-quality electromagnetic (EM) absorbing materials. These materials are crucial for filtering out undesirable radiation and protecting sensitive objects. The requirements for these filters extend beyond absorbing EM energy; they must also offer protection across a wide operation bandwidth (BW), various angles of incidence, and different polarizations. The objective of the research is to design, fabricate, and optimize composite materials with a periodic porous structure for EM absorption. The approach involves leveraging the concept of metamaterials to achieve multiple goals in absorption performance in the frequency range of 8-12 GHz (X-band). This entails creating materials that not only absorb a significant amount of EM energy but also exhibit effectiveness across a broad spectrum of operational parameters, making them versatile and efficient in shielding against electromagnetic radiation.

In the initial research phase, fundamental polymer-based composites are designed to meet commercial application requirements, ensuring a minimum absorption level of -20 dB [22]. These composites serve as a baseline for later metamaterial design, with a focus on careful consideration of composition, dispersion, and micromorphology for specific intrinsic properties. Chapter 2 concentrates on designing graphene-based composites, comparing electrical permittivity. Larger lateral size of graphene nanoplatelets (GNPs) show potential for higher electrical conductivity, related to permittivity, but may compromise homogeneity due to

dispersion challenges compared with reduced graphene oxide (rGO). Incorporating $CoFe_2O_4$ magnetic nanoparticles allows customizable magnetic permeability as well as manipulation of the micromorphology of the composites resulting internal interaction with the EM wave. However, their natural agglomeration prompts surface modification with oleic acid and polyethylene glycol to enhance dispersion, especially at higher loading fractions. Different compounding techniques are compared, with solution mixing (2.5GN50COE) achieving -38 dB RL and 0.63 GHz BW at -20 dB for the absorber thickness of 2.3 mm, while twin-screw extruder (T7.5GN) offers higher production but maxes at -21 dB RL with the BW at -20 dB of 0.2 GHz at the absorber thickness of 2.0 mm. These baseline materials set the reference for subsequent metamaterial-enhanced absorption performance.

The subsequent phase of the study involves designing and optimizing meta-structures using the fabricated baseline materials to achieve multiple design objectives. Computational modeling and optimization, detailed in Chapter 3, are employed to simplify the complex design process. The chapter outlines the construction of EM-field-based finite element models for simulating the RL response of periodic porous structures. The Monte-Carlo optimizer is introduced to tailor the selection of structures based on a multi-objective function, including maximizing RL and operation bandwidth. The most efficient structure identified by the optimizer is the truncated cone pillar with PEC on the top surface, achieved from the 2.3 mm thick solution-mixed 2.5GN50COE. This structure provides a broadened operation bandwidth at -20 dB of 1.8 GHz. The optimizer enhances the RL of the poorly absorbing composite material (T7.5GN) from -21 dB to -67 dB for a thickness of around 2 mm. This improvement results from metamaterial behavior induced by resonance from the interaction between repeated pores, confirmed by electric field distribution analysis.

In addition to the design and optimization of the periodic porous structure metamaterial absorbers, this research also provided the guidelines to produce the meta-structure absorbers from the prefabricated composite material. The first manufacturing technique utilized the traditional material subtraction method for the pre-molded composites using CNC machining. The second method contributed to the extrusion-based additive manufacturing as FDM technique. The final method presented in this work is the compression molding of the pre-engineered mold assembly. However, there is room to improve the processing parameters of each technique to achieve the desired composite intrinsic properties and structural accuracy and precision.

In summary, the approach outlined in this study presents the capacity to design and produce metamaterial absorbers that enhance absorption performance. These absorbers not only showcase elevated RL but also encompass added benefits aligned with user-defined multiple objective functions.

5.2 Future Work

Envisaging prospective avenues for research development stemming from this study, several areas warrant thorough investigation to refine and augment the initially outlined outcomes. Within the foundational phase of the composite material, opportunities exist to optimize its electromagnetic (EM) absorption performance. Delving into the intricacies of micromorphology, dispersion, and constituent elements is imperative for enhancing absorption capabilities and expanding the operational bandwidth. A systematic exploration of alternative conductive and magnetic fillers is indispensable, considering the promising attributes of advanced materials such as MXene [87,92,229] and carbon nanotubes (CNTs) [22,36,66,72,147,265] documented in prior research. Simultaneously, the integration of

alternative advanced magnetic constituents presents a pivotal avenue for further absorption enhancement, aligning with findings in existing literature [43,52,57,59,62,117,136,224,266]. The mechanical attributes of the composites, crucial for feasibility and manufacturability, necessitate a discerning approach. The prevailing brittleness, attributed to the heightened volume fraction of ceramic $CoFe_2O_4$, underscores the exigency of investigating alternative matrices, constituents, ternary systems, and compositions. These strategic considerations transcend the refinement of this research's objectives, bearing significance for the broader landscape of materials science and electromagnetic applications.

In the realm of computational modeling and the optimization of meta-structures, there exists the prospect of elevating the performance of metamaterial absorbers through the incorporation of additional objective functions. Parameters such as wide-angle incidence, polarization independence, and insensitivity to manufacturing errors can be integrated into the optimizer to attain superior outcomes. Acknowledging the constraints imposed by manufacturing limitations, particularly pertaining to the baseline composite design, a judicious modification of constraints in the optimization analysis becomes imperative. Furthermore, considerations encompassing mechanical properties, aesthetic attributes, thickness variations, and environmental resistances must be factored into the computational modeling for meta-structures and the experimental design for baseline composites, aligning with the specific requirements of diverse applications. Notably, the current optimizer employs the Monte-Carlo method, which involves testing objective functions at randomly defined iteration points within uniformly distributed parameter spaces. While this approach facilitates proximity to the global optimized solution, it may fall short of reaching the pinnacle of optimization performance if the iteration count is insufficient. Exploring alternative algorithms grounded in improvement concepts, such

as particle swarm [248–250], Nelder-Meads [248,249], or Broyden, in conjunction with the established Monte-Carlo optimizer presents a promising avenue for enhancing global solutions. By initializing from the solution obtained through the Monte-Carlo method, these alternative algorithms offer the potential to further refine and maximize the global solution. It is crucial, however, to opt for gradient-free methods, given the inherent challenges in deriving derivatives for the objective functions within our computational modeling framework.

As outlined in Chapter 4, the presented results serve as guiding principles for the production of periodic porous metamaterial absorbers. However, several facets in the realm of manufacturing demand further refinement to achieve successful production with the desired properties. Firstly, in the context of CNC machining, critical processing parameters such as spindle speed, feed rate, and tool selection necessitate meticulous optimization tailored to the designed composite systems, post-processing requirements, and meta-structure designs. Additionally, the processing parameters for composites, particularly in compression molding, including molding temperature, pressure, heating and cooling rates, and dwell time at each step, remain subject to optimization for attaining the desired structures and mechanical properties of absorbers without compromising the micromorphology of the composites. Furthermore, additive manufacturing techniques, considered as potential methods for rapid prototyping during the design and optimization phase, require precise tuning of parameters for successful production of absorber prototypes through Fused Deposition Modeling (FDM). Parameters such as printing speed, temperature, cooling rate, pattern, linewidth, layer thickness, and the quality of the input filament, including uniform diameter, well-dispersed fillers, and suitable mechanical properties, demand optimization to ensure the efficacy of the printing process. These refinements in

manufacturing parameters are essential steps towards the realization of metamaterial absorbers with the intended properties.

As emphasized earlier, the enhancement of periodic porous structure metamaterial absorbers requires a comprehensive and simultaneous integration of efforts across multiple facets. It is imperative to synchronize advancements in material design, structural design, and production methodologies to collectively elevate the overall performance of these absorbers. Recognizing the interdependence of these elements, a holistic approach that addresses each aspect concurrently is essential for achieving optimal outcomes in the development of metamaterial absorbers with improved periodic porous structures. This integrated strategy ensures that material properties, structural configurations, and production processes are mutually aligned, thereby contributing synergistically to the overarching objective of enhancing absorber performance.

Bibliography

[1] Zhang, Liying, Shuguang Bi and MLiu. Lightweight Electromagnetic Interference Shielding Materials and Their Mechanisms. Electromagnetic Materials and Devices, 2018, p. 1. https://doi.org/http://dx.doi.org/10.5772/57353.

[2] Jagadeesh Chandra RB, Shivamurthy B, Kulkarni SD, Kumar MS. Hybrid polymer composites for EMI shielding application- a review. Mater Res Express 2019;6. https://doi.org/10.1088/2053-1591/aaff00.

[3] Chakradhary VK, Bhusan Baskey HB, Roshan R, Akhtar MJ. Thin, lightweight and high EMI shielding efficiency CNF/Epoxy nanocomposite for civil and military application. 2019 IEEE MTT-S International Microwave and RF Conference, IMARC 2019 2019:1–4. https://doi.org/10.1109/IMaRC45935.2019.9118710.

[4] Winterhalter CA, Teverovsky J, Wilson P, Slade J, Farell B, Horowitz W, et al. Development of electronic textiles to transport data and power in future U.S. military protective clothing systems. ASTM Special Technical Publication 2005;9:15–23. https://doi.org/10.1520/stp12594s.

[5] Klemperer CJ von, Maharaj D. Composite electromagnetic interference shielding materials for aerospace applications. Compos Struct 2009;91:467–72. https://doi.org/10.1016/j.compstruct.2009.04.013.

[6] Jayalakshmi CG, Inamdar A, Anand A, Kandasubramanian B. Polymer matrix composites as broadband radar absorbing structures for stealth aircrafts. J Appl Polym Sci 2019;136:1–21. https://doi.org/10.1002/app.47241.

[7] Kong LB, Li ZW, Liu L, Huang R, Abshinova M, Yang ZH, et al. Recent progress in some composite materials and structures for specific electromagnetic applications Recent progress in some composite materials and structures for specific electromagnetic applications 2013;6608. https://doi.org/10.1179/1743280412Y.0000000011.

[8] Jahn O. Electromagnetic fields: Low dose exposure, current update. Int Arch Occup Environ Health 2000;73:18–20. https://doi.org/10.1007/pl00014617.

[9] Ziegelberger G, Croft R, Feychting M, Green AC, Hirata A, d'Inzeo G, et al. Guidelines for limiting exposure to electromagnetic fields (100 kHz to 300 GHz). vol. 118. 2020. https://doi.org/10.1097/HP.0000000000001210.

[10] Tirkey MM, Gupta N. Electromagnetic absorber design challenges. IEEE Electromagn Compat Mag 2019;8:59–65. https://doi.org/10.1109/MEMC.2019.8681370.

[11] Cao M, Han C, Wang X, Zhang M, Zhang Y, Shu J, et al. Graphene nanohybrids: Excellent electromagnetic properties for the absorbing and shielding of electromagnetic waves. J Mater Chem C Mater 2018;6:4586–602. https://doi.org/10.1039/c7tc05869a.

[12] Ranjan P, Choubey A, Mahto SK. A novel approach for optimal design of multilayer wideband microwave absorber using wind driven optimization technique. AEU - International Journal of Electronics and Communications 2018;83:81–7. https://doi.org/10.1016/j.aeue.2017.08.039.

[13] Mouna H, Mekaladevi V, Nirmala Devi M. Design of microwave absorbers using improvised particle swarm optimization algorithm. Journal of Microwaves,

Optoelectronics and Electromagnetic Applications 2018;17:188–200. https://doi.org/10.1590/2179-10742018v17i2836.

[14] Ding F, Cui Y, Ge X, Jin Y, He S. Ultra-broadband microwave metamaterial absorber. Appl Phys Lett 2012;100:1–5. https://doi.org/10.1063/1.3692178.

[15] Xiaopeng Shen, Tie Jun Cui, Junming Zhao, Hui Feng Ma, Wei Xiang Jiang and HL. Polarization-independent wide-angle triple-band metamaterial absorber. Opt Express 2011;19:9401–7.

[16] Hill MJ. The microwave palaeointensity technique and its application to lava. PhD Dissertation. Liverpool University, United Kingdom, 2000.

[17] Kim SS, Jo SB, Gueon KI, Choi KK, Kim JM, Churn KS. Complex Permeability and Permittivity and Microwave Absorption of Ferrite-Rubber Composite in X-band Frequencies. IEEE Trans Magn 1991;27:5462–4. https://doi.org/10.1109/20.278872.

[18] Ulaby FT, Michielssen E, Ravaioli U. Fundamentals of Applied Electromagnetics 6e by Fawwaz T . Ulaby , Eric Michielssen , and Umberto Ravaioli 2010.

[19] Baker-Jarvis J. Transmission/reflection and short-circuit line permittivity measurements. Unknown 1990:148. https://doi.org/Technical Note 1355-R.

[20] Song W li, Cao M sheng, Hou Z ling, Yuan J, Fang X yong. High-temperature microwave absorption and evolutionary behavior of multiwalled carbon nanotube nanocomposite. Scr Mater 2009;61:201–4. https://doi.org/10.1016/j.scriptamat.2009.03.048.

[21] Song W, Guan X, Fan L, Cao W, Zhao Q, Wang C, et al. Tuning broadband microwave absorption via highly conductive Fe 3 O 4 / graphene heterostructural nanofillers. Mater Res Bull 2015;72:316–23. https://doi.org/10.1016/j.materresbull.2015.07.028.

[22] Al-saleh MH, Sundararaj U. Electromagnetic interference shielding mechanisms of CNT / polymer composites. Carbon N Y 2009;47:1738–46. https://doi.org/10.1016/j.carbon.2009.02.030.

[23] Guo Z, Park S, Hahn HT, Wei S, Moldovan M, Karki AB, et al. Magnetic and electromagnetic evaluation of the magnetic nanoparticle filled polyurethane nanocomposites. J Appl Phys 2007;101. https://doi.org/10.1063/1.2711074.

[24] Arjmand M, Apperley T, Okoniewski M, Sundararaj U. Comparative study of electromagnetic interference shielding properties of injection molded versus compression molded multi-walled carbon nanotube/polystyrene composites. Carbon N Y 2012;50:5126–34. https://doi.org/10.1016/j.carbon.2012.06.053.

[25] Clark DEWHS. MICROWAVE PROCESSING OF MATERIALS. Annual Review of Materials Science 1996;26:299–331.

[26] Meng F, Wei W, Chen X, Xu X, Jiang M, Jun L, et al. Design of porous C@Fe3O4 hybrid nanotubes with excellent microwave absorption. Physical Chemistry Chemical Physics 2016;18:2510–6. https://doi.org/10.1039/c5cp06687e.

[27] Du Y, Liu W, Qiang R, Wang Y, Han X, Ma J, et al. Shell Thickness-Dependent Microwave Absorption of Core–Shell Fe 3 O 4 @C Composites. ACS Appl Mater Interfaces 2014;6:12997–3006. https://doi.org/10.1021/am502910d.

[28] S. Geetha, K. K. Satheesh Kumar, Chepuri R. K. Rao, M. Vijayan DCT. EMI Shielding: Methods and Materials—A Review S. J Appl Polym Sci 2009;112:2073–2086.

[29] Devender, Ramasamy SR. Review of EMI shielding and suppression materials. Proceedings of the International Conference on Electromagnetic Interference and Compatibility, 1997, p. 459–66. https://doi.org/10.1109/icemic.1997.669850.

[30] Thomassin JM, Jérôme C, Pardoen T, Bailly C, Huynen I, Detrembleur C. Polymer/carbon based composites as electromagnetic interference (EMI) shielding materials. Materials Science and Engineering R: Reports 2013;74:211–32. https://doi.org/10.1016/j.mser.2013.06.001.

[31] Qin F, Brosseau C. A review and analysis of microwave absorption in polymer composites filled with carbonaceous particles. J Appl Phys 2012;111. https://doi.org/10.1063/1.3688435.

[32] Chen Y, Wang Y, Zhang H Bin, Li X, Gui CX, Yu ZZ. Enhanced electromagnetic interference shielding efficiency of polystyrene/graphene composites with magnetic Fe3O4 nanoparticles. Carbon N Y 2015;82:67–76. https://doi.org/10.1016/j.carbon.2014.10.031.

[33] Gholampoor M, Movassagh-Alanagh F, Salimkhani H. Fabrication of nano-Fe3O4 3D structure on carbon fibers as a microwave absorber and EMI shielding composite by modified EPD method. Solid State Sci 2017;64:51–61. https://doi.org/10.1016/j.solidstatesciences.2016.12.005.

[34] Liu Y, Lu M, Wu K, Yao S, Du X, Chen G, et al. Anisotropic thermal conductivity and electromagnetic interference shielding of epoxy nanocomposites based on magnetic driving reduced graphene oxide@Fe 3 O 4. Compos Sci Technol 2019;174:1–10. https://doi.org/10.1016/j.compscitech.2019.02.005.

[35] Kumar R, Choudhary HK, Pawar SP, Bose S, Sahoo B. Carbon encapsulated nanoscale iron/iron-carbide/graphite particles for EMI shielding and microwave absorption. Physical Chemistry Chemical Physics 2017;19:23268–79. https://doi.org/10.1039/c7cp03175k.

[36] Dhakate SR, Subhedar KM, Singh BP. Polymer nanocomposite foam filled with carbon nanomaterials as an efficient electromagnetic interference shielding material. RSC Adv 2015;5:43036–57. https://doi.org/10.1039/c5ra03409d.

[37] Chung DDL. Materials for Electromagnetic Interference Shielding. J Mater Eng Perform 2000;9:350–4.

[38] Sankaran S, Deshmukh K, Ahamed MB, Pasha SKK. Recent advances in electromagnetic interference shielding properties of metal and carbon fi ller reinforced fl exible polymer composites : A review. Composites Part A 2018;114:49–71. https://doi.org/10.1016/j.compositesa.2018.08.006.

[39] Joshi A, Datar S. Carbon nanostructure composite for electromagnetic interference shielding. Pramana - Journal of Physics 2015;84:1099–116. https://doi.org/10.1007/s12043-015-1005-9.

[40] Al-Saleh MH, Gelves GA, Sundararaj U. Copper nanowire/polystyrene nanocomposites: Lower percolation threshold and higher EMI shielding. Compos Part A Appl Sci Manuf 2011;42:92–7. https://doi.org/10.1016/j.compositesa.2010.10.003.

[41] Joshi A, Bajaj A, Singh R, Alegaonkar PS, Balasubramanian K, Datar S. Graphene nanoribbon-PVA composite as EMI shielding material in the X band (Nanotechnology (2013) 24 (455705)). Nanotechnology 2014;25. https://doi.org/10.1088/0957-4484/25/23/239501.

[42] Goyal RK, Sulakhe R. Study on poly(vinylidene fluoride)/nickel composites with low percolation. Adv Mater Lett 2015;6:309–17. https://doi.org/10.5185/amlett.2015.5627.

[43] Panda M, Srinivas V, Thakur AK. On the question of percolation threshold in polyvinylidene fluoride/nanocrystalline nickel composites. Appl Phys Lett 2008;92:10–3. https://doi.org/10.1063/1.2900710.

[44] Panda M, Srinivas V, Thakur AK. Surface and interfacial effect of filler particle on electrical properties of polyvinyledene fluoride/nickel composites. Appl Phys Lett 2008;93:242908. https://doi.org/10.1063/1.3054163.

[45] Al-Saleh MH, Saadeh WH, Sundararaj U. EMI shielding effectiveness of carbon based nanostructured polymeric materials: A comparative study. Carbon N Y 2013;60:146–56. https://doi.org/10.1016/j.carbon.2013.04.008.

[46] Kanat Anurakparadorn, Alan Taub EM. Dispersion of Cobalt Ferrite Functionalized Graphene Nanoplatelets in PLA for EMI Shielding Applications. Proceedings of the American Society of Composite the 36th technical conference, Virtual Conference, Texas A&M University, College Station, Texas, USA: 2021, p. 2163–92.

[47] Zhao B, Park CB. conductive poly (vinylidene fluoride)/ Ni chain 2017:6954–61. https://doi.org/10.1039/c7tc01865g.

[48] Fu M, Jiao Q, Zhao Y, Li H. Vapor diffusion synthesis of CoFe2O4 hollow sphere/graphene composites as absorbing materials. J Mater Chem A Mater 2014;2:735–44. https://doi.org/10.1039/c3ta14050d.

[49] Li GM, Wang LC, Xu Y. Templated synthesis of highly ordered mesoporous cobalt ferrite and its microwave absorption properties. Chinese Physics B 2014;23. https://doi.org/10.1088/1674-1056/23/8/088105.

[50] Zhang F, Jia Z, Wang Z, Zhang C, Wang B, Xu B, et al. Tailoring nanoparticles composites derived from metal-organic framework as electromagnetic wave absorber. Materials Today Physics 2021;20. https://doi.org/10.1016/j.mtphys.2021.100475.

[51] Hossein S, Mohseni SH, Asadnia A, Kerdari H. Synthesis and microwave absorbing properties of polyaniline / MnFe 2 O 4 nanocomposite. J Alloys Compd 2011;509:4682–7. https://doi.org/10.1016/j.jallcom.2010.11.198.

[52] Wang Y, Gao X, Zhang L, Wu X, Wang Q, Luo C, et al. Synthesis of Ti 3 C 2 /Fe 3 O 4 /PANI hierarchical architecture composite as an efficient wide-band electromagnetic absorber. Appl Surf Sci 2019;480:830–8. https://doi.org/10.1016/j.apsusc.2019.03.049.

[53] Song WL, Cao MS, Wen B, Hou ZL, Cheng J, Yuan J. Synthesis of zinc oxide particles coated multiwalled carbon nanotubes: Dielectric properties, electromagnetic interference shielding and microwave absorption. Mater Res Bull 2012;47:1747–54. https://doi.org/10.1016/j.materresbull.2012.03.045.

[54] Ma E, Li J, Zhao N, Liu E, He C, Shi C. Preparation of reduced graphene oxide/Fe3O4 nanocomposite and its microwave electromagnetic properties. Mater Lett 2013;91:209–12. https://doi.org/10.1016/j.matlet.2012.09.097.

[55] Ling J, Zhai W, Feng W, Shen B, Zhang J, Zheng WG. Facile preparation of lightweight microcellular polyetherimide/graphene composite foams for electromagnetic interference shielding. ACS Appl Mater Interfaces 2013;5:2677–84. https://doi.org/10.1021/am303289m.

[56] Wang T, Li Y, Geng S, Zhou C, Jia X, Yang F, et al. Preparation of flexible reduced graphene oxide/poly(vinyl alcohol) film with superior microwave absorption properties. RSC Adv 2015;5:88958–64. https://doi.org/10.1039/c5ra16158d.

[57] Hosseinabadi S, Sheykhifard Z, Mohseni M, Kokabi M, Jamilpanah L, Hajali M, et al. Preparation iron-nickel/graphene heterogeneous composites for enhanced microwave absorption performance via electrochemical exfoliation/deposition technique. Mater Chem Phys 2021;260:124155. https://doi.org/10.1016/j.matchemphys.2020.124155.

[58] Li N, Zheng M, Chang X, Ji G, Lu H, Xue L, et al. Preparation of magnetic CoFe2O4-functionalized graphene sheets via a facile hydrothermal method and their adsorption properties. J Solid State Chem 2011;184:953–8. https://doi.org/10.1016/j.jssc.2011.01.014.

[59] Fu M, Jiao Q, Zhao Y. Preparation of NiFe2O4 nanorod-graphene composites via an ionic liquid assisted one-step hydrothermal approach and their microwave absorbing properties. J Mater Chem A Mater 2013;1:5577–86. https://doi.org/10.1039/c3ta10402h.

[60] Mathew J, Sathishkumar M, Kothurkar NK, Senthilkumar R, Sabarish Narayanan B. Polyaniline/Fe3O4-RGO Nanocomposites for Microwave Absorption. IOP Conf Ser Mater Sci Eng, vol. 310, Institute of Physics Publishing; 2018. https://doi.org/10.1088/1757-899X/310/1/012138.

[61] Dosoudil R, Ušáková M, Franek J, Sláma J, Grusková A. Particle size and concentration effect on permeability and em-wave absorption properties of hybrid ferrite polymer composites. IEEE Trans Magn 2010;46:436–9. https://doi.org/10.1109/TMAG.2009.2033347.

[62] Li C, Song H, Jiang X, Zhang Z, Yu L. An efficient high-frequency electromagnetic wave absorber: Nickel-N@Carbon composite. J Alloys Compd 2020;814. https://doi.org/10.1016/j.jallcom.2019.152171.

[63] Kong L, Yin X, Yuan X, Zhang Y, Liu X, Cheng L, et al. Electromagnetic wave absorption properties of graphene modified with carbon nanotube/poly(dimethyl siloxane) composites. Carbon N Y 2014;73:185–93. https://doi.org/10.1016/j.carbon.2014.02.054.

[64] Liu L, Bian XM, Hou ZL, Wang CY, Li ZS, Hu HD, et al. Electromagnetic response of magnetic graphene hybrid fillers and their evolutionary behaviors. Journal of Materials Science: Materials in Electronics 2016;27:2760–72. https://doi.org/10.1007/s10854-015-4088-7.

[65] Chaudhary A, Kumari S, Kumar R, Teotia S, Singh BP, Singh AP, et al. Lightweight and Easily Foldable MCMB-MWCNTs Composite Paper with Exceptional Electromagnetic Interference Shielding. ACS Appl Mater Interfaces 2016;8:10600–8. https://doi.org/10.1021/acsami.5b12334.

[66] Lin JH, Lin ZI, Pan YJ, Huang CL, Chen CK, Lou CW. Polymer composites made of multi-walled carbon nanotubes and graphene nano-sheets: Effects of sandwich structures on their electromagnetic interference shielding effectiveness. Compos B Eng 2016;89:424–31. https://doi.org/10.1016/j.compositesb.2015.11.014.

[67] Fletcher A, Gupta MC, Dudley KL, Vedeler E. Elastomer foam nanocomposites for electromagnetic dissipation and shielding applications 2010;70:953–8. https://doi.org/10.1016/j.compscitech.2010.02.011.

[68] Thomassin JM, Pagnoulle C, Bednarz L, Huynen I, Jerome R, Detrembleur C. Foams of polycaprolactone/MWNT nanocomposites for efficient EMI reduction. J Mater Chem 2008;18:792–6. https://doi.org/10.1039/b709864b.

[69] Ameli A, Jung PU, Park CB. Electrical properties and electromagnetic interference shielding effectiveness of polypropylene/carbon fiber composite foams. Carbon N Y 2013;60:379–91. https://doi.org/10.1016/j.carbon.2013.04.050.

[70] Shen B, Zhai W, Tao M, Ling J, Zheng W. Lightweight , Multifunctional Polyetherimide / Graphene @ Fe 3 O 4 Composite Foams for Shielding of Electromagnetic Pollution 2013. https://doi.org/10.1021/am4036527.

[71] Alkuh MS, Famili MHN, Shirvan MMM, Moeini MH. The relationship between electromagnetic absorption properties and cell structure of poly (methyl methacrylate)/ multi-walled carbon nanotube composite foams. JMADE 2016;100:73–83. https://doi.org/10.1016/j.matdes.2016.03.075.

[72] Xu X Bin, Li ZM, Shi L, Bian XC, Xiang ZD. Ultralight conductive carbon-nanotube-polymer composite. Small 2007;3:408–11. https://doi.org/10.1002/smll.200600348.

[73] Yan DX, Pang H, Xu L, Bao Y, Ren PG, Lei J, et al. Electromagnetic interference shielding of segregated polymer composite with an ultralow loading of in situ thermally reduced graphene oxide. Nanotechnology 2014;25. https://doi.org/10.1088/0957-4484/25/14/145705.

[74] Jiang Q, Liao X, Li J, Chen J, Wang G, Yi J, et al. Flexible thermoplastic polyurethane/reduced graphene oxide composite foams for electromagnetic interference shielding with high absorption characteristic. Compos Part A Appl Sci Manuf 2019;123:310–9. https://doi.org/10.1016/j.compositesa.2019.05.017.

[75] Castles F, Isakov D, Lui A, Lei Q, Dancer CEJ, Wang Y, et al. Microwave dielectric characterisation of 3D-printed BaTiO3/ABS polymer composites. Sci Rep 2016;6. https://doi.org/10.1038/srep22714.

[76] Song Z, Liu X, Sun X, Li Y, Nie X, Tang W, et al. Alginate-templated synthesis of CoFe/carbon fiber composite and the effect of hierarchically porous structure on electromagnetic wave absorption performance. Carbon N Y 2019;151:36–45. https://doi.org/10.1016/j.carbon.2019.05.025.

[77] Yin L, Tian X. 3D printing and characterization of metamaterial composite structures for absorbing and shielding electromagnetic waves. J Phys Conf Ser, vol. 1721, IOP Publishing Ltd; 2021. https://doi.org/10.1088/1742-6596/1721/1/012026.

[78] Shi S, Peng Z, Jing J, Yang L, Chen Y. 3D Printing of Delicately Controllable Cellular Nanocomposites Based on Polylactic Acid Incorporating Graphene/Carbon Nanotube Hybrids for Efficient Electromagnetic Interference Shielding. ACS Sustain Chem Eng 2020;8:7962–72. https://doi.org/10.1021/acssuschemeng.0c01877.

[79] Yuan Y, Liu L, Yang M, Zhang T, Xu F, Lin Z, et al. Lightweight, thermally insulating and stiff carbon honeycomb-induced graphene composite foams with a horizontal laminated structure for electromagnetic interference shielding. Carbon N Y 2017;123:223–32. https://doi.org/10.1016/j.carbon.2017.07.060.

[80] Bollen P, Quievy N, Detrembleur C, Thomassin JM, Monnereau L, Bailly C. Processing of a new class of multifunctional hybrid for electromagnetic absorption based on a foam fi lled honeycomb. JMADE 2016;89:323–34. https://doi.org/10.1016/j.matdes.2015.09.129.

[81] Luo H, Chen F, Wang F, Wang X, Dai W, Hu S, et al. Preparation and microwave absorption properties of honeycomb core structures coated with composite absorber. AIP Adv 2018;8. https://doi.org/10.1063/1.5005163.

[82] Xu H, Yin X, Li M, Li X, Li X, Dang X, et al. Ultralight Cellular Foam from Cellulose Nanofiber/Carbon Nanotube Self-Assemblies for Ultrabroad-Band Microwave Absorption. ACS Appl Mater Interfaces 2019. https://doi.org/10.1021/acsami.9b03731.

[83] Kshetrimayum RS. A brief intro to metamaterials. IEEE Potentials 2004;23:44–6. https://doi.org/10.1109/MP.2005.1368916.

[84] Watts CM, Liu X, Padilla WJ. Metamaterial electromagnetic wave absorbers. Advanced Materials 2012;24. https://doi.org/10.1002/adma.201200674.

[85] Li W, Liu Q, Wang L, Zhou Z, Zheng J, Ying Y, et al. Low frequency and broadband metamaterial absorber with cross arrays and a flaked iron powder magnetic composite. AIP Adv 2018;8. https://doi.org/10.1063/1.5010821.

[86] Zhang Y, Feng Y, Zhu B, Zhao J, Jiang T. Graphene based tunable metamaterial absorber and polarization modulation in terahertz frequency. Opt Express 2014;22:22743. https://doi.org/10.1364/oe.22.022743.

[87] Choi G, Shahzad F, Bahk YM, Jhon YM, Park H, Alhabeb M, et al. Enhanced Terahertz Shielding of MXenes with Nano-Metamaterials. Adv Opt Mater 2018;6:1–6. https://doi.org/10.1002/adom.201701076.

[88] Tao H, Landy NI, Bingham CM, Zhang X, Averitt RD, Padilla WJ. A metamaterial absorber for the terahertz regime: design, fabrication and characterization. Opt Express 2008;16:7181. https://doi.org/10.1364/oe.16.007181.

[89] Landy NI, Sajuyigbe S, Mock JJ, Smith DR, Padilla WJ. Perfect Metamaterial Absorber 2008;207402:1–4. https://doi.org/10.1103/PhysRevLett.100.207402.

[90] Zhu B, Wang Z, Huang C, Feng Y, Zhao J, Jiang T. POLARIZATION INSENSITIVE METAMATERIAL ABSORBER WITH WIDE INCIDENT ANGLE. Progress In Electromagnetics Research 2010;101:231–9. https://doi.org/10.2528/PIER10011110.

[91] Rhee JY, Yoo YJ, Kim KW, Kim YJ, Lee YP. Metamaterial-based perfect absorbers. J Electromagn Waves Appl 2014;28:1541–80. https://doi.org/10.1080/09205071.2014.944273.

[92] Ma B, Chen F, Cheng Y, Li X, Luo H. Constructing broadband microwave metastructure absorber based on 2D Ti3CNTx MXene magnetic composites. J Alloys Compd 2023;953. https://doi.org/10.1016/j.jallcom.2023.170039.

[93] Zhou Q, Qi C, Shi T, Li Y, Ren W, Gu S, et al. 3D printed carbon based all-dielectric honeycomb metastructure for thin and broadband electromagnetic absorption. Compos Part A Appl Sci Manuf 2023;169. https://doi.org/10.1016/j.compositesa.2023.107541.

[94] Ren J, Yin JY. 3D-printed low-cost dielectric-resonator-based ultra-broadband microwave absorber using carbon-loaded Acrylonitrile Butadiene styrene polymer. Materials 2018;10. https://doi.org/10.3390/ma11071249.

[95] Jiang W, Yan L, Ma H, Fan Y, Wang J, Feng M, et al. Electromagnetic wave absorption and compressive behavior of a three-dimensional metamaterial absorber based on 3D printed honeycomb. Sci Rep 2018;8. https://doi.org/10.1038/s41598-018-23286-6.

[96] Huang L, Duan Y, Yang X, Gao S, Zeng Y, Ma G, et al. Ultra-flexible composite metamaterials with enhanced and tunable microwave absorption performance. Compos Struct 2019;229. https://doi.org/10.1016/j.compstruct.2019.111469.

[97] Avi Bregman. Morphology Control of Polymer Composites for Enhanced Microwave Absorption. 2019.

[98] Bregman A, Michielssen E, Taub A. Comparison of experimental and modeled EMI shielding properties of periodic porous xGNP/PLA composites. Polymers (Basel) 2019;11. https://doi.org/10.3390/polym11081233.

[99] Bregman A, Taub A, Michielssen E. Computational design of composite EMI shields through the control of pore morphology. MRS Commun 2018;8:1153–7. https://doi.org/10.1557/mrc.2018.171.

[100] Yan J, Huang Y, Wei C, Zhang N, Liu P. Covalently bonded polyaniline/graphene composites as high-performance electromagnetic (EM) wave absorption materials. Compos Part A Appl Sci Manuf 2017;99:121–8. https://doi.org/10.1016/j.compositesa.2017.04.016.

[101] Li X, Feng J, Du Y, Bai J, Fan H, Zhang H, et al. One-pot synthesis of CoFe2O4/graphene oxide hybrids and their conversion into FeCo/graphene hybrids for lightweight and highly efficient microwave absorber. J Mater Chem A Mater 2015;3:5535–46. https://doi.org/10.1039/c4ta05718j.

[102] Marra F, Lecini J, Tamburrano A, Pisu L, Sarto MS. Electromagnetic wave absorption and structural properties of wide-band absorber made of graphene-printed glass-fibre composite. Sci Rep 2018;8. https://doi.org/10.1038/s41598-018-30498-3.

[103] Zong M, Huang Y, Zhang N, Wu H. Influence of (RGO)/(ferrite) ratios and graphene reduction degree on microwave absorption properties of graphene composites. J Alloys Compd 2015;644:491–501. https://doi.org/10.1016/j.jallcom.2015.05.073.

[104] Synthesis of graphene@branching-like polypyrrole@CoFe2O4composites and their excellent electromagnetic waveabsorption properties.pdf n.d.

[105] Wu H, Xing L, Cai Y, Liu L, He E, Li B, et al. A study on the fused deposition modeling process of graphene/nano-Fe3O4 composite absorber and its absorbing properties of electromagnetic microwave. Applied Sciences (Switzerland) 2020;10:1–12. https://doi.org/10.3390/app10041508.

[106] Shahzad F, Yu S, Kumar P, Lee JW, Kim YH, Hong SM, et al. Sulfur doped graphene/polystyrene nanocomposites for electromagnetic interference shielding. Compos Struct 2015;133:1267–75. https://doi.org/10.1016/j.compstruct.2015.07.036.

[107] Shen B, Li Y, Zhai W, Zheng W. Compressible Graphene-Coated Polymer Foams with Ultralow Density for Adjustable Electromagnetic Interference (EMI) Shielding. ACS Appl Mater Interfaces 2016;8:8050–7. https://doi.org/10.1021/acsami.5b11715.

[108] D'Aloia AG, Marra F, Tamburrano A, De Bellis G, Sarto MS. Electromagnetic absorbing properties of graphene-polymer composite shields. Carbon N Y 2014;73:175–84. https://doi.org/10.1016/j.carbon.2014.02.053.

[109] Kim S, Oh J, Kim M, Jang W, Wang M, Kim Y, et al. Electromagnetic Interference (EMI) Transparent Shielding of Reduced Graphene Oxide (RGO) Interleaved Structure Fabricated by Electrophoretic Deposition 2014. https://doi.org/10.1021/am503893v.

[110] Marra F, Lecini J, Tamburrano A, Pisu L, Sarto MS. Electromagnetic wave absorption and structural properties of wide-band absorber made of graphene-printed glass-fibre composite. Sci Rep 2018;8:1–9. https://doi.org/10.1038/s41598-018-30498-3.

[111] Nasr Esfahani A, Katbab A, Taeb A, Simon L, Pope MA. Correlation between mechanical dissipation and improved X-band electromagnetic shielding capabilities of amine functionalized graphene/thermoplastic polyurethane composites. Eur Polym J 2017;95:520–38. https://doi.org/10.1016/j.eurpolymj.2017.08.038.

[112] Kashi S, Gupta RK, Baum T, Kao N, Bhattacharya SN. Dielectric properties and electromagnetic interference shielding effectiveness of graphene-based biodegradable nanocomposites. Mater Des 2016;109:68–78. https://doi.org/10.1016/j.matdes.2016.07.062.

[113] Kashi S, Gupta RK, Baum T, Kao N, Bhattacharya SN. Dielectric properties and electromagnetic interference shielding effectiveness of graphene-based biodegradable nanocomposites. Mater Des 2016;109:68–78. https://doi.org/10.1016/j.matdes.2016.07.062.

[114] Shi S, Peng Z, Jing J, Yang L, Chen Y. 3D Printing of Delicately Controllable Cellular Nanocomposites Based on Polylactic Acid Incorporating Graphene/Carbon Nanotube Hybrids for Efficient Electromagnetic Interference Shielding. ACS Sustain Chem Eng 2020;8:7962–72. https://doi.org/10.1021/acssuschemeng.0c01877.

[115] Jakus AE, Secor EB, Rutz AL, Jordan SW, Hersam MC, Shah RN. Three-dimensional printing of high-content graphene scaffolds for electronic and biomedical applications. ACS Nano 2015;9:4636–48. https://doi.org/10.1021/acsnano.5b01179.

[116] Yan D, Ren P, Pang H, Fu Q, Yang M, Li Z. Efficient electromagnetic interference graphene / polystyrene composite shielding of lightweight 2012.

[117] Zhang S, Wang Y, Ran Q, Fu Q, Gu Y. Electromagnetic interference shielding property of polybenzoxazine / graphene / nickel composites 2019. https://doi.org/10.1016/j.reactfunctpolym.2019.104324.

[118] Liang J, Wang Y, Huang Y, Ma Y, Liu Z, Cai J. Letter to the Editor Electromagnetic interference shielding of graphene / epoxy composites. Carbon N Y 2008;47:922–5. https://doi.org/10.1016/j.carbon.2008.12.038.

[119] Kong L, Yin X, Zhang Y, Yuan X, Li Q, Ye F, et al. Electromagnetic wave absorption properties of reduced graphene oxide modified by maghemite colloidal nanoparticle clusters. Journal of Physical Chemistry C 2013;117:19701–11. https://doi.org/10.1021/jp4058498.

[120] Wang C, Han X, Xu P, Zhang X, Du Y, Hu S, et al. The electromagnetic property of chemically reduced graphene oxide and its application as microwave absorbing material. Appl Phys Lett 2011;98:1–4. https://doi.org/10.1063/1.3555436.

[121] Das CK, Bhattacharya P, Kalra SS. Graphene and MWCNT: Potential Candidate for Microwave Absorbing Materials. Journal of Materials Science Research 2012;1:126–32. https://doi.org/10.5539/jmsr.v1n2p126.

[122] Kim H, Abdala AA, MacOsko CW. Graphene/polymer nanocomposites. Macromolecules 2010;43:6515–30. https://doi.org/10.1021/ma100572e.

[123] Meng F, Wang H, Huang F, Guo Y, Wang Z, Hui D, et al. Graphene-based microwave absorbing composites : A review and prospective. Composites Part B 2018;137:260–77. https://doi.org/10.1016/j.compositesb.2017.11.023.

[124] Guo Z, Chen Y, Lu NL, Yan X, Xiang L, He Q, et al. Electromagnetic Interference Shielding Polymer Nanocomposites. Multifunctional Nanocomposites for Energy and Environmental Applications, 2018, p. 567–601. https://doi.org/10.1002/9783527342501.ch19.

[125] Quan B, Liang X, Ji G, Cheng Y, Liu W, Ma J, et al. Dielectric polarization in electromagnetic wave absorption: Review and perspective. J Alloys Compd 2017;728:1065–75. https://doi.org/10.1016/j.jallcom.2017.09.082.

[126] Hsiao ST, Ma CCM, Tien HW, Liao WH, Wang YS, Li SM, et al. Effect of covalent modification of graphene nanosheets on the electrical property and electromagnetic interference shielding performance of a water-borne polyurethane composite. ACS Appl Mater Interfaces 2015;7:2817–26. https://doi.org/10.1021/am508069v.

[127] Bai X, Zhai Y, Zhang Y. Green approach to prepare graphene-based composites with high microwave absorption capacity. Journal of Physical Chemistry C 2011;115:11673–7. https://doi.org/10.1021/jp202475m.

[128] Zhang J, Yang H, Shen G, Cheng P, Zhang J, Guo S. Reduction of graphene oxide via L -ascorbic acid. Chem Commun 2010;46:1112–4. https://doi.org/10.1039/B917705A.

[129] Pei S, Cheng H. The reduction of graphene oxide. Carbon N Y 2012;50:3210–28. https://doi.org/10.1016/j.carbon.2011.11.010.

[130] Shen Y, Jing T, Ren W, Zhang J, Jiang ZG, Yu ZZ, et al. Chemical and thermal reduction of graphene oxide and its electrically conductive polylactic acid nanocomposites. Compos Sci Technol 2012;72:1430–5. https://doi.org/10.1016/j.compscitech.2012.05.018.

[131] Compton OC, Nguyen ST. Graphene oxide, highly reduced graphene oxide, and graphene: Versatile building blocks for carbon-based materials. Small 2010;6:711–23. https://doi.org/10.1002/smll.200901934.

[132] Zeng S, Li X, Li M, Zheng J, E S, Yang W, et al. Flexible PVDF/CNTs/Ni@CNTs composite films possessing excellent electromagnetic interference shielding and mechanical properties under heat treatment. Carbon N Y 2019;155:34–43. https://doi.org/10.1016/j.carbon.2019.08.024.

[133] Liao H, Li D, Zhou C, Liu T. Microporous Co / rGO nanocomposites : Strong and broadband microwave absorber with well-matched dielectric and magnetic loss 2019;782:556–65.

[134] Wang Y, Guan H, Dong C, Xiao X, Du S, Wang Y. Reduced graphene oxide (RGO)/ Mn 3 O 4 nanocomposites for dielectric loss properties and electromagnetic interference shielding effectiveness at high frequency. Ceram Int 2016;42:936–42. https://doi.org/10.1016/j.ceramint.2015.09.022.

[135] Dosoudil R, Ušáková M, Franek J, Grusková A, Sláma J. Dispersion of complex permeability and EM-wave absorbing characteristics of polymer-based composites with dual ferrite filler. J Magn Magn Mater 2008;320. https://doi.org/10.1016/j.jmmm.2008.04.071.

[136] Bi Y, Ma M, Liao Z, Tong Z, Chen Y, Wang R, et al. One-dimensional Ni@Co/C@PPy composites for superior electromagnetic wave absorption. J Colloid Interface Sci 2022;605:483–92. https://doi.org/10.1016/j.jcis.2021.07.050.

[137] Shen W, Ren B, Cai K, Song Y fei, Wang W. Synthesis of nonstoichiometric Co0.8Fe2.2O4/reduced graphene oxide (rGO) nanocomposites and their excellent electromagnetic wave absorption property. J Alloys Compd 2019;774:997–1008. https://doi.org/10.1016/j.jallcom.2018.09.361.

[138] Liu Y, Song D, Wu C, Leng J. EMI shielding performance of nanocomposites with MWCNTs, nanosized Fe 3O4 and Fe. Compos B Eng 2014;63:34–40. https://doi.org/10.1016/j.compositesb.2014.03.014.

[139] Ding Y, Liao Q, Liu S, Guo H, Sun Y, Zhang G, et al. Reduced Graphene Oxide Functionalized with Cobalt Ferrite Nanocomposites for Enhanced Efficient and

Lightweight Electromagnetic Wave Absorption. Sci Rep 2016;6:1–9. https://doi.org/10.1038/srep32381.

[140] Tung TT, Feller J, Kim T, Kim H, Yang WS, Suh KS. Electromagnetic Properties of Fe 3 O 4 -Functionalized Graphene and Its Composites with a Conducting Polymer 2012:927–35. https://doi.org/10.1002/pola.25847.

[141] Zhang XJ, Wang GS, Cao WQ, Wei YZ, Liang JF, Guo L, et al. Enhanced microwave absorption property of reduced graphene oxide (RGO)-MnFe2O4 nanocomposites and polyvinylidene fluoride. ACS Appl Mater Interfaces 2014;6:7471–8. https://doi.org/10.1021/am500862g.

[142] Singh AP, Mishra M, Sambyal P, Gupta BK, Singh BP, Chandra A, et al. Encapsulation of γ-Fe2O3 decorated reduced graphene oxide in polyaniline core-shell tubes as an exceptional tracker for electromagnetic environmental pollution. J Mater Chem A Mater 2014;2:3581–93. https://doi.org/10.1039/c3ta14212d.

[143] Bayat M, Yang H, Ko FK, Michelson D, Mei A. Electromagnetic interference shielding effectiveness of hybrid multifunctional Fe 3 O 4 / carbon nano fi ber composite 2014;55:936–43. https://doi.org/10.1016/j.polymer.2013.12.042.

[144] Dosoudil R, Franek J, Sláma J, Ušáková M, Grusková A. Electromagnetic wave absorption performances of metal alloy/spinel ferrite/polymer composites. IEEE Trans Magn 2012;48:1524–7. https://doi.org/10.1109/TMAG.2011.2172779.

[145] Wang Y, Gao X, Wu X, Zhang W, Luo C, Liu P. Facile design of 3D hierarchical NiFe2O4/N-GN/ZnO composite as a high performance electromagnetic wave absorber. Chemical Engineering Journal 2019;375. https://doi.org/10.1016/j.cej.2019.121942.

[146] Manna K, Srivastava SK. Fe3O4@Carbon@Polyaniline Trilaminar Core-Shell Composites as Superior Microwave Absorber in Shielding of Electromagnetic Pollution. ACS Sustain Chem Eng 2017;5:10710–21. https://doi.org/10.1021/acssuschemeng.7b02682.

[147] Wang Y, Gao X, Lin C, Shi L, Li X, Wu G. Metal organic frameworks-derived Fe-Co nanoporous carbon/graphene composite as a high-performance electromagnetic wave absorber. J Alloys Compd 2019;785:765–73. https://doi.org/10.1016/j.jallcom.2019.01.271.

[148] Feng X, Huang Y, Chen X, Wei C, Zhang X, Chen M. Hierarchical CoFe2O4/NiFe2O4 nanocomposites with enhanced electrochemical capacitive properties. J Mater Sci 2018;53:2648–57. https://doi.org/10.1007/s10853-017-1735-9.

[149] Oliveira PN, Silva DM, Dias GS, Santos IA, Cótica LF. Synthesis and physical property measurements of CoFe2O4:BaTiO3 core-shell composite nanoparticles. Ferroelectrics 2016;499:76–82. https://doi.org/10.1080/00150193.2016.1172882.

[150] Liu Z, Xu G, Zhang M, Xiong K, Meng P. Synthesis of CoFe2O4/RGO nanocomposites by click chemistry and electromagnetic wave absorption properties. Journal of Materials Science: Materials in Electronics 2016;27:9278–85. https://doi.org/10.1007/s10854-016-4966-7.

[151] Ismail MM, Rafeeq SN, Sulaiman JMA, Mandal A. Electromagnetic interference shielding and microwave absorption properties of cobalt ferrite CoFe2O4/polyaniline composite. Appl Phys A Mater Sci Process 2018;124:1–12. https://doi.org/10.1007/s00339-018-1808-x.

[152] Karthickraja D, Karthi S, Kumar GA, Sardar DK, Dannangoda GC, Martirosyan KS, et al. Fabrication of core-shell CoFe2O4@HAp nanoparticles: A novel magnetic platform for biomedical applications. New Journal of Chemistry 2019;43:13584–93. https://doi.org/10.1039/c9nj02510c.

[153] Fu M, Jiao Q, Zhao Y, Li H. Vapor diffusion synthesis of CoFe2O4 hollow sphere/graphene composites as absorbing materials. J Mater Chem A Mater 2014;2:735–44. https://doi.org/10.1039/c3ta14050d.

[154] Li X, Feng J, Du Y, Bai J, Fan H, Zhang H, et al. One-pot synthesis of CoFe2O4/graphene oxide hybrids and their conversion into FeCo/graphene hybrids for lightweight and highly efficient microwave absorber. J Mater Chem A Mater 2015;3:5535–46. https://doi.org/10.1039/c4ta05718j.

[155] Ismail MM, Rafeeq SN, Sulaiman JMA, Mandal A. Electromagnetic interference shielding and microwave absorption properties of cobalt ferrite CoFe 2 O 4 / polyaniline composite. Applied Physics A 2018;0:0. https://doi.org/10.1007/s00339-018-1808-x.

[156] Zong M, Huang Y, Wu H, Zhao Y, Wang Q, Sun X. One-pot hydrothermal synthesis of RGO/CoFe2O4 composite and its excellent microwave absorption properties. Mater Lett 2014;114:52–5. https://doi.org/10.1016/j.matlet.2013.09.113.

[157] Gill N, Sharma AL, Gupta V, Tomar M, Pandey OP, Singh DP. Enhanced microwave absorption and suppressed reflection of polypyrrole-cobalt ferrite-graphene nanocomposite in X-band. J Alloys Compd 2019;797:1190–7. https://doi.org/10.1016/j.jallcom.2019.05.176.

[158] Gill N, Sharma AL, Gupta V, Tomar M, Pandey OP, Singh DP. Enhanced microwave absorption and suppressed reflection of polypyrrole-cobalt ferrite-graphene

nanocomposite in X-band. J Alloys Compd 2019;797:1190–7. https://doi.org/10.1016/j.jallcom.2019.05.176.

[159] Yallapu MM, Foy SP, Jain TK, Labhasetwar V. PEG-functionalized magnetic nanoparticles for drug delivery and magnetic resonance imaging applications. Pharm Res 2010;27:2283–95. https://doi.org/10.1007/s11095-010-0260-1.

[160] Kalhapure RS, Bolla PK, Boddu SHS, Renukuntla J. Evaluation of oleic acid and polyethylene glycol monomethyl ether conjugate (Pegylated oleic acid) as a solubility enhancer of furosemide. Processes 2019;7. https://doi.org/10.3390/pr7080520.

[161] Chen J, Yao B, Li C, Shi G. An improved Hummers method for eco-friendly synthesis of graphene oxide. Carbon N Y 2013;64:225–9. https://doi.org/10.1016/j.carbon.2013.07.055.

[162] De Silva KKH, Huang HH, Yoshimura M. Progress of reduction of graphene oxide by ascorbic acid. Appl Surf Sci 2018;447:338–46. https://doi.org/10.1016/j.apsusc.2018.03.243.

[163] Zhang J, Yang H, Shen G, Cheng P, Zhang J, Guo S. Reduction of graphene oxide via L -ascorbic acid. Chem Commun 2010;46:1112–4. https://doi.org/10.1039/B917705A.

[164] Furst A, Berlo RC, Hooton S. Hydrazine as a Reducing Agent for Organic Compounds (Catalytic Hydrazine Reductions). Chem Rev 1965;65:51–68. https://doi.org/10.1021/cr60233a002.

[165] Zhao D, Wu X, Guan H, Han E. Study on supercritical hydrothermal synthesis of CoFe2O4 nanoparticles. Journal of Supercritical Fluids 2007;42:226–33. https://doi.org/10.1016/j.supflu.2007.03.004.

[166] Du F, Fischer JE, Winey KI. Coagulation method for preparing single-walled carbon nanotube/poly(methyl methacrylate) composites and their modulus, electrical conductivity, and thermal stability. J Polym Sci B Polym Phys 2003;41:3333–8. https://doi.org/10.1002/polb.10701.

[167] Tsipogiannis Ch. Microwave materials characterization using waveguides and coaxial probe. LTH, Lund University SE-221 00 Lund, Sweden 2012:61.

[168] Rothwell EJ, Frasch JL, Ellison SM, Chahal P, Ouedraogo RO. Analysis of the Nicolson-Ross-Weir method for characterizing the electromagnetic properties of engineered materials. Progress in Electromagnetics Research 2016;157:31–47. https://doi.org/10.2528/PIER16071706.

[169] De Paula AL, Rezende MC, Barroso JJ. Modified Nicolson-Ross-Weir (NRW) method to retrieve the constitutive parameters of low-loss materials. SBMO/IEEE MTT-S International Microwave and Optoelectronics Conference Proceedings 2011:488–92. https://doi.org/10.1109/IMOC.2011.6169293.

[170] Ulaby, F. T., Michielssen, E., & Ravaioli U (2010). Fundamentals of applied electromagnetics. 6th ed. Boston, Massachussetts: Prentice Hall; 2010.

[171] Wentworth SM. MATLAB demonstration of transmission line phenomena in electromagnetics. ASEE Annual Conference and Exposition, Conference Proceedings, 2012.

[172] Jovanović S, Spreitzer M, Tramšek M, Trontelj Z, Suvorov D. Supporting Information Effect of Oleic Acid Concentration on the Physicochemical Properties of Cobalt Ferrite Nanoparticles. n.d.

[173] Nalle FC, Wahid R, Wulandari IO, Sabarudin A. Synthesis and characterization of magnetic Fe 3 O 4 nanoparticles using oleic acid as stabilizing agent. Rasayan Journal of Chemistry 2019;12:14–21. https://doi.org/10.31788/RJC.2019.1214082.

[174] Gupta R, Pancholi K, De Sa R, Murray D, Huo D, Droubi G, et al. Effect of Oleic Acid Coating of Iron Oxide Nanoparticles on Properties of Magnetic Polyamide-6 Nanocomposite. JOM 2019;71:3119–28. https://doi.org/10.1007/s11837-019-03622-5.

[175] Rana S, Philip J, Raj B. Micelle based synthesis of cobalt ferrite nanoparticles and its characterization using Fourier Transform Infrared Transmission Spectrometry and Thermogravimetry. Mater Chem Phys 2010;124:264–9. https://doi.org/10.1016/j.matchemphys.2010.06.029.

[176] Kanagesan S, Hashim M, Tamilselvan S, Alitheen NB, Ismail I, Bahmanrokh G. Cytotoxic effect of nanocrystalline MgFe2O4 Particles for Cancer Cure. J Nanomater 2013;2013. https://doi.org/10.1155/2013/865024.

[177] Boobalan T, Suriyanarayanan N, Pavithradevi S. Structural, magnetic and dielectric properties of nanocrystalline cobalt ferrite by wet hydroxyl chemical route. Mater Sci Semicond Process 2013;16:1695–700. https://doi.org/10.1016/j.mssp.2013.04.013.

[178] Bohara RA, Thorat ND, Yadav HM, Pawar SH. One-step synthesis of uniform and biocompatible amine functionalized cobalt ferrite nanoparticles: A potential carrier for biomedical applications. New Journal of Chemistry 2014;38:2979–86. https://doi.org/10.1039/c4nj00344f.

[179] Mishra KA, Ramaprabhu S. Carbon dioxide adsorption in graphene sheets. AIP Advances 1 2016;032152:10–6. https://doi.org/https://doi.org/10.1063/1.3638178.

[180] Alam SN, Sharma N, Kumar L. Synthesis of Graphene Oxide (GO) by Modified Hummers Method and Its Thermal Reduction to Obtain Reduced Graphene Oxide (rGO). Graphene 2017;06:1–18. https://doi.org/10.4236/graphene.2017.61001.

[181] Rattana T, Chaiyakun S, Witit-Anun N, Nuntawong N, Chindaudom P, Oaew S, et al. Preparation and characterization of graphene oxide nanosheets. Procedia Eng, vol. 32, 2012, p. 759–64. https://doi.org/10.1016/j.proeng.2012.02.009.

[182] Andrijanto E, Shoelarta S, Subiyanto G, Rifki S. Facile synthesis of graphene from graphite using ascorbic acid as reducing agent. AIP Conf Proc, vol. 1725, 2016. https://doi.org/10.1063/1.4945457.

[183] Çiplak Z, Yildiz N, Cąlimli A. Investigation of graphene/Ag nanocomposites synthesis parameters for two different synthesis methods. Fullerenes Nanotubes and Carbon Nanostructures 2015;23:361–70. https://doi.org/10.1080/1536383X.2014.894025.

[184] Wang G, Ma Y, Wei Z, Qi M. Development of multifunctional cobalt ferrite / graphene oxide nanocomposites for magnetic resonance imaging and controlled drug delivery. CHEMICAL ENGINEERING JOURNAL 2016;289:150–60. https://doi.org/10.1016/j.cej.2015.12.072.

[185] Kotutha I, Duangchuen T, Swatsitang E, Meewasana W, Khajonrit J, Maensiri S. Electrochemical properties of rGO/CoFe2O4 nanocomposites for energy storage application. Ionics (Kiel) 2019;25:5401–9. https://doi.org/10.1007/s11581-019-03114-1.

[186] Chen Y, Niu Y, Tian T, Zhang J, Wang Y, Li Y, et al. Microbial reduction of graphene oxide by Azotobacter chroococcum. Chem Phys Lett 2017;677:143–7. https://doi.org/10.1016/j.cplett.2017.04.002.

[187] Wang Q, Wang Y, Meng Q, Wang T, Guo W, Wu G, et al. Preparation of high antistatic HDPE/polyaniline encapsulated graphene nanoplatelet composites by solution blending. RSC Adv 2017;7:2796–803. https://doi.org/10.1039/C6RA26458A.

[188] De Silva KKH, Huang HH, Yoshimura M. Progress of reduction of graphene oxide by ascorbic acid. Appl Surf Sci 2018;447:338–46. https://doi.org/10.1016/j.apsusc.2018.03.243.

[189] Gupta B, Kumar N, Panda K, Kanan V, Joshi S, Visoly-Fisher I. Role of oxygen functional groups in reduced graphene oxide for lubrication. Sci Rep 2017;7:1–14. https://doi.org/10.1038/srep45030.

[190] Tong XZ, Song F, Li MQ, Wang XL, Chin IJ, Wang YZ. Fabrication of graphene/polylactide nanocomposites with improved properties. Compos Sci Technol 2013;88:33–8. https://doi.org/10.1016/j.compscitech.2013.08.028.

[191] Teixeira EDM, De Campos A, Marconcini JM, Bondancia TJ, Wood D, Klamczynski A, et al. Starch/fiber/poly(lactic acid) foam and compressed foam composites. RSC Adv 2014;4:6616–23. https://doi.org/10.1039/c3ra47395c.

[192] Nanaki S, Barmpalexis P, Iatrou A, Christodoulou E, Kostoglou M, Bikiaris DN. Risperidone controlled release microspheres based on poly(lactic acid)-poly(propylene adipate) novel polymer blends appropriate for long acting injectable formulations. Pharmaceutics 2018;10. https://doi.org/10.3390/pharmaceutics10030130.

[193] XGScience Inc. xGnP® Graphene Nanoplatelets – Grade M Data Sheet. n.d.

[194] Abid, Sehrawat P, Islam SS, Mishra P, Ahmad S. Reduced graphene oxide (rGO) based wideband optical sensor and the role of Temperature, Defect States and Quantum Efficiency. Sci Rep 2018;8:1–13. https://doi.org/10.1038/s41598-018-21686-2.

[195] Chang H, Sun Z, Saito M, Yuan Q, Zhang H, Li J, et al. Regulating infrared photoresponses in reduced graphene oxide phototransistors by defect and atomic structure control. ACS Nano 2013;7:6310–20. https://doi.org/10.1021/nn4023679.

[196] Valizadeh Kiamahalleh M, Gholampour A, Tran DNH, Ozbakkaloglu T, Losic D. Physiochemical and mechanical properties of reduced graphene oxide–cement mortar composites: Effect of reduced graphene oxide particle size. Constr Build Mater 2020;250:118832. https://doi.org/10.1016/j.conbuildmat.2020.118832.

[197] Covaliu CI, Jitaru I, Paraschiv G, Vasile E, Biriş SŞ, Diamandescu L, et al. Core-shell hybrid nanomaterials based on CoFe2O4 particles coated with PVP or PEG biopolymers for applications in biomedicine. Powder Technol 2013;237:415–26. https://doi.org/10.1016/j.powtec.2012.12.037.

[198] Babu A, Thomas A, T BKK. Structural , magnetic , and acidic properties of cobalt ferrite nanoparticles synthesised by wet chemical methods 2015;4:199–205. https://doi.org/10.1007/s40145-015-0149-x.

[199] Cao Y, Cai SR, Fan SC, Hu WQ, Zheng M Sen, Dong QF. Reduced graphene oxide anchoring CoFe2O4 nanoparticles as an effective catalyst for non-aqueous lithium-oxygen batteries. Faraday Discuss 2014;172:215–21. https://doi.org/10.1039/c4fd00075g.

[200] Yao Y, Yang Z, Zhang D, Peng W, Sun H, Wang S. Magnetic CoFe 2O 4-graphene hybrids: Facile synthesis, characterization, and catalytic properties. Ind Eng Chem Res, vol. 51, 2012, p. 6044–51. https://doi.org/10.1021/ie300271p.

[201] Meidanchi A. Cobalt ferrite nanoparticles supported on reduced graphene oxide sheets: Optical, magnetic and magneto-antibacterial studies. Nanotechnology 2020;31. https://doi.org/10.1088/1361-6528/aba7e2.

[202] Sharifi I, Shokrollahi H, Doroodmand MM, Safi R. Magnetic and structural studies on CoFe 2O 4 nanoparticles synthesized by co-precipitation, normal micelles and reverse micelles methods. J Magn Magn Mater 2012;324:1854–61. https://doi.org/10.1016/j.jmmm.2012.01.015.

[203] Allaedini G, Tasirin SM, Aminayi P. Magnetic properties of cobalt ferrite synthesized by hydrothermal method. Int Nano Lett 2015;5:183–6. https://doi.org/10.1007/s40089-015-0153-8.

[204] Grigorova M, Blythe HJ, Blaskov V, Rusanov V, Petkov V, Masheva V, et al. Magnetic properties and Mössbauer spectra of nanosized CoFe2O4 powders. J Magn Magn Mater 1998;183:163–72. https://doi.org/10.1016/S0304-8853(97)01031-7.

[205] Arun T, Verma SK, Panda PK, Joseyphus RJ, Jha E, Akbari-Fakhrabadi A, et al. Facile synthesized novel hybrid graphene oxide/cobalt ferrite magnetic nanoparticles based surface coating material inhibit bacterial secretion pathway for antibacterial effect. Materials Science and Engineering C 2019;104:109932. https://doi.org/10.1016/j.msec.2019.109932.

[206] Alyami M, Khashab M, Costa PMFJ. Cobalt ferrite supported on reduced graphene oxide as a T 2 contrast agent for magnetic resonance imaging † 2019:6299–309. https://doi.org/10.1039/c8ra09476d.

[207] Dai Q, Lam M, Swanson S, Yu RHR, Milliron DJ, Topuria T, et al. Monodisperse cobalt ferrite nanomagnets with uniform silica coatings. Langmuir 2010;26:17546–51. https://doi.org/10.1021/la103042q.

[208] Che X-D, Bertram HN. Phenomenology of curves and magnetic interactions. vol. 116. 1992.

[209] Meidanchi A. graphene oxide sheets : optical , magnetic and Cobalt ferrite nanoparticles supported on reduced graphene oxide sheets : optical , magnetic and magneto-antibacterial studies 2020.

[210] Ateia EE, Arman MKAMM, Ramadan R, Shafaay AS. Optimizing the physical properties of cobalt / graphene nanocomposites for technological applications. Applied Physics A 2019;125:1–8. https://doi.org/10.1007/s00339-019-2815-2.

[211] Tarhini A, Tehrani-Bagha A, Kazan M, Grady B. The effect of graphene flake size on the properties of graphene-based polymer composite films. J Appl Polym Sci 2021;138:1–10. https://doi.org/10.1002/app.49821.

[212] Wang JY, Tao J, Severac L, Mesguich D, Laurent C. Modified Nicolson-Ross-Weir Method 2017;2.

[213] Zong M, Huang Y, Zhang N, Wu H. Influence of (RGO)/(ferrite) ratios and graphene reduction degree on microwave absorption properties of graphene composites. J Alloys Compd 2015;644:491–501. https://doi.org/10.1016/j.jallcom.2015.05.073.

[214] Bera R, Maitra A, Paria S, Karan SK, Das AK, Bera A, et al. An approach to widen the electromagnetic shielding efficiency in PDMS/ferrous ferric oxide decorated RGO–SWCNH composite through pressure induced tunability. Chemical Engineering Journal 2018;335:501–9. https://doi.org/10.1016/j.cej.2017.10.178.

[215] Huang Y, Li N, Ma Y, Du F, Li F, He X, et al. The influence of single-walled carbon nanotube structure on the electromagnetic interference shielding efficiency of its epoxy composites. Carbon N Y 2007;45:1614–21. https://doi.org/10.1016/j.carbon.2007.04.016.

[216] Liu Z, Bai G, Huang Y, Ma Y, Du F, Li F, et al. Reflection and absorption contributions to the electromagnetic interference shielding of single-walled carbon

nanotube/polyurethane composites. Carbon N Y 2007;45:821–7. https://doi.org/10.1016/j.carbon.2006.11.020.

[217] Choudhary HK, Kumar R, Pawar SP, Anupama A V., Bose S, Sahoo B. Effect of Coral-Shaped Yttrium Iron Garnet Particles on the EMI Shielding Behaviour of Yttrium Iron Garnet-Polyaniline-Wax Composites. ChemistrySelect 2018;3:2120–30. https://doi.org/10.1002/slct.201702698.

[218] Shi S, Zhang L, Li J. Complex permittivity and electromagnetic interference shielding properties of Ti3SiC2/polyaniline composites. J Mater Sci 2009;44:945–8. https://doi.org/10.1007/s10853-008-3207-8.

[219] Nasouri K, Shoushtari AM, Mojtahedi MRM. Theoretical and experimental studies on EMI shielding mechanisms of multi-walled carbon nanotubes reinforced high performance composite nanofibers. Journal of Polymer Research 2016;23:3–10. https://doi.org/10.1007/s10965-016-0943-3.

[220] Ni J, Zhan R, Qiu J, Fan J, Dong B, Guo Z. Multi-interfaced graphene aerogel/polydimethylsiloxane metacomposites with tunable electrical conductivity for enhanced electromagnetic interference shielding. J Mater Chem C Mater 2020;8:11748–59. https://doi.org/10.1039/d0tc02278k.

[221] Snarskii AA, Sarychev AK, Bezsudnov I V., Lagarkov AN. Thermoelectric figure of merit for bulk nanostructured composites with distributed parameters. Semiconductors 2012;46:659–65. https://doi.org/10.1134/S106378261205020X.

[222] Micheli D, Apollo C, Pastore R, Marchetti M. X-Band microwave characterization of carbon-based nanocomposite material, absorption capability comparison and RAS design

simulation. Compos Sci Technol 2010;70:400–9. https://doi.org/10.1016/j.compscitech.2009.11.015.

[223] Kong L, Yin X, Yuan X, Zhang Y, Liu X, Cheng L. Electromagnetic wave absorption properties of graphene modified with carbon nanotube / poly (dimethyl siloxane) composites. Carbon N Y 2014;73:185–93. https://doi.org/10.1016/j.carbon.2014.02.054.

[224] Abbas SM, Chatterjee R, Dixit AK, Kumar AVR, Goel TC. Electromagnetic and microwave absorption properties of (Co 2+-Si4+) substituted barium hexaferrites and its polymer composite. J Appl Phys 2007;101. https://doi.org/10.1063/1.2716379.

[225] Hou T, Jia Z, Wang B, Li H, Liu X, Chi Q, et al. Metal-organic framework-derived NiSe2-CoSe2@C/Ti3C2Tx composites as electromagnetic wave absorbers. Chemical Engineering Journal 2021;422. https://doi.org/10.1016/j.cej.2021.130079.

[226] Ran J, Guo M, Zhong L, Fu H. In situ growth of BaTiO3 nanotube on the surface of reduced graphene oxide: A lightweight electromagnetic absorber. J Alloys Compd 2019;773:423–31. https://doi.org/10.1016/j.jallcom.2018.09.142.

[227] Hou C, Li T, Zhao T, Zhang W, Cheng Y. Electromagnetic wave absorbing properties of carbon nanotubes doped rare metal/pure carbon nanotubes double-layer polymer composites. Mater Des 2012;33:413–8. https://doi.org/10.1016/j.matdes.2011.04.042.

[228] Liu P, Yao Z, Zhou J, Yang Z, Kong LB. Small magnetic Co-doped NiZn ferrite/graphene nanocomposites and their dual-region microwave absorption performance. J Mater Chem C Mater 2016;4:9738–49. https://doi.org/10.1039/c6tc03518c.

[229] Cui C, Guo R, Ren E, Xiao H, Zhou M, Lai X, et al. MXene-based rGO/Nb2CTx/Fe3O4 composite for high absorption of electromagnetic wave. Chemical Engineering Journal 2021;405. https://doi.org/10.1016/j.cej.2020.126626.

[230] Anurakparadorn Kanat, Taub Alan. A Comparative Study of the Effect of Compounding Methods and Processing of PLA/GNPs on the Micromorphology and Electrical Conductivity. Proceedings of the American Society of Composite the 38th Technical Conference, Boston, MA, USA 2023.

[231] Sun X, Liu X, Shen X, Wu Y, Wang Z, Kim JK. Graphene foam/carbon nanotube/poly(dimethyl siloxane) composites for exceptional microwave shielding. Compos Part A Appl Sci Manuf 2016;85:199–206. https://doi.org/10.1016/j.compositesa.2016.03.009.

[232] Jun Y, Sy S, Ahn W, Zarrin H, Rasen L, Tjandra R, et al. Highly conductive interconnected graphene foam based polymer composite 2015;95:653–8.

[233] Cao X, Lee LJ, Widya T, Macosko C. Polyurethane / clay nanocomposites foams : processing , structure and properties 2005;46:775–83. https://doi.org/10.1016/j.polymer.2004.11.028.

[234] Méjean C, Pometcu L, Benzerga R, Sharaiha A, Le Paven-Thivet C, Badard M, et al. Electromagnetic absorber composite made of carbon fibers loaded epoxy foam for anechoic chamber application. Materials Science and Engineering: B 2017;220:59–65. https://doi.org/10.1016/j.mseb.2017.03.009.

[235] Xu H, Yin X, Li M, Li X, Li X, Dang X, et al. Ultralight Cellular Foam from Cellulose Nanofiber/Carbon Nanotube Self-Assemblies for Ultrabroad-Band Microwave Absorption. ACS Appl Mater Interfaces 2019. https://doi.org/10.1021/acsami.9b03731.

[236] Sun Y, Luo S, Sun H, Zeng W, Ling C, Chen D, et al. Engineering closed-cell structure in lightweight and fl exible carbon foam composite for high-ef fi cient electromagnetic

interference shielding. Carbon N Y 2018;136:299–308. https://doi.org/10.1016/j.carbon.2018.04.084.

[237] Gedler G, Antunes M, Velasco JI. Effects of graphene nanoplatelets on the morphology of polycarbonate-graphene composite foams prepared by supercritical carbon dioxide two-step foaming. Journal of Supercritical Fluids 2015;100:167–74. https://doi.org/10.1016/j.supflu.2015.02.005.

[238] Gedler G, Antunes M, Velasco JI. Effects of graphene nanoplatelets on the morphology of polycarbonate-graphene composite foams prepared by supercritical carbon dioxide two-step foaming. Journal of Supercritical Fluids 2015;100:167–74. https://doi.org/10.1016/j.supflu.2015.02.005.

[239] Rubrice K, Castel X, Himdi M, Parneix P. Dielectric characteristics and microwave absorption of graphene composite materials. Materials 2016;9. https://doi.org/10.3390/ma9100825.

[240] Luo H, Chen F, Wang F, Wang X, Dai W, Hu S, et al. Preparation and microwave absorption properties of honeycomb core structures coated with composite absorber. AIP Adv 2018;8. https://doi.org/10.1063/1.5005163.

[241] Luo F, Liu D, Cao T, Cheng H, Kuang J, Deng Y, et al. Study on broadband microwave absorbing performance of gradient porous structure. Adv Compos Hybrid Mater 2021;4:591–601. https://doi.org/10.1007/s42114-021-00275-4.

[242] Yin L, Tian X, Shang Z, Li D. Ultra-broadband metamaterial absorber with graphene composites fabricated by 3D printing. Mater Lett 2019;239:132–5. https://doi.org/10.1016/j.matlet.2018.12.087.

[243] Zhu Z, Zhou J, Li Y, Qi X, Wang Y, Wen Y. Design of a composite metamaterial toward perfect microwave absorption and excellent load-bearing performance. Mater Des 2023;229. https://doi.org/10.1016/j.matdes.2023.111910.

[244] Zhang L, Fan J, Liu Y, Xie H, Xie J. Demonstration of broadband magnetic polymer composite absorber crossing S- and C-bands. Appl Phys B 2020;126. https://doi.org/10.1007/s00340-020-7415-5.

[245] Beeharry T, Yahiaoui R, Selemani K, Ouslimani HH. A dual layer broadband radar absorber to minimize electromagnetic interference in radomes. Sci Rep 2018;8. https://doi.org/10.1038/s41598-017-18859-w.

[246] COMSOL Inc. RF module user guide v5.4a 2017:1–224.

[247] Yang X-S. Multi-Objective Optimization. Nature-Inspired Optimization Algorithms, Elsevier; 2014, p. 197–211. https://doi.org/10.1016/b978-0-12-416743-8.00014-2.

[248] Lagarias JC, Reeds JA, Wright MH, Wright PE. Convergence properties of the Nelder-Mead simplex method in low dimensions. SIAM Journal on Optimization 1998;9:112–47. https://doi.org/10.1137/S1052623496303470.

[249] Luersen MA, Le Riche R. Globalized nelder-mead method for engineering optimization. Comput Struct, vol. 82, 2004, p. 2251–60. https://doi.org/10.1016/j.compstruc.2004.03.072.

[250] Poli R, Kennedy J, Blackwell T. Particle swarm optimization. Swarm Intelligence 2007;1:33–57. https://doi.org/10.1007/s11721-007-0002-0.

[251] Metropolis N, Ulam S. The Monte Carlo Method. J Am Stat Assoc 1949;44:335–41. https://doi.org/10.1080/01621459.1949.10483310.

[252] Neese JA, Harrell GK, Wang J. Bounded Monte Carlo integration using Java. Proceedings of the 2014 ACM Southeast Regional Conference, ACM SE 2014, Association for Computing Machinery; 2014. https://doi.org/10.1145/2638404.2638493.

[253] COMSOL. Introduction to LiveLink for MATLAB 2013:1–54.

[254] Comsol. LiveLink for MATLAB User's Guide. Version 43b 2013:282.

[255] Song WL, Guan XT, Fan LZ, Cao WQ, Zhao QL, Wang CY, et al. Tuning broadband microwave absorption via highly conductive Fe3O4/graphene heterostructural nanofillers. Mater Res Bull 2015;72:316–23. https://doi.org/10.1016/j.materresbull.2015.07.028.

[256] Guo H, Zhao H, Niu H, Ren Y, Fang H, Fang X, et al. Highly Thermally Conductive 3D Printed Graphene Filled Polymer Composites for Scalable Thermal Management Applications. ACS Nano 2021;15:6917–28. https://doi.org/10.1021/acsnano.0c10768.

[257] Spinelli G, Kotsilkova R, Ivanov E, Petrova-Doycheva I, Menseidov D, Georgiev V, et al. Effects of filament extrusion, 3D printing and hot-pressing on electrical and tensile properties of poly(Lactic) acid composites filled with carbon nanotubes and graphene. Nanomaterials 2020;10. https://doi.org/10.3390/nano10010035.

[258] Benelhadjsaid C, Porter RS. Crystalline-state extrusion of low density polyethylenes. J Appl Polym Sci 1985;30:741–53. https://doi.org/10.1002/app.1985.070300222.

[259] Guo H, Lv R, Bai S. Recent advances on 3D printing graphene-based composites. Nano Materials Science 2019;1:101–15. https://doi.org/10.1016/j.nanoms.2019.03.003.

[260] Chandran V. A comparative study of the mechanical performance of PLA specimens manufactured using compression molding and 3D printing. Toronto, Ontario, Canada: 2011.

[261] Craft DF, Kry SF, Balter P, Salehpour M, Woodward W, Howell RM. Material matters: Analysis of density uncertainty in 3D printing and its consequences for radiation oncology. Med Phys 2018;45:1614–21. https://doi.org/10.1002/mp.12839.

[262] Chandran V, Kalman J, Fayazbakhsh K, Bougherara H. A comparative study of the tensile properties of compression molded and 3D printed PLA specimens in dry and water saturated conditions. Journal of Mechanical Science and Technology 2021;35:1977–85. https://doi.org/10.1007/s12206-021-0415-5.

[263] Dul S, Fambri L, Pegoretti A. Fused deposition modelling with ABS-graphene nanocomposites. Compos Part A Appl Sci Manuf 2016;85:181–91. https://doi.org/10.1016/j.compositesa.2016.03.013.

[264] Wang B, Szkopek T, Cerruti M. Flow rate controls microstructural alignment of extruded graphene oxide structures. Carbon N Y 2022;192:145–52. https://doi.org/10.1016/j.carbon.2022.02.029.

[265] Gonçalves C, Gonçalves IC, Magalhães FD, Pinto AM. Poly(lactic acid) composites containing carbon-based nanomaterials: A review. Polymers (Basel) 2017;9:1–37. https://doi.org/10.3390/polym9070269.

[266] Li BW, Shen Y, Yue ZX, Nan CW. Enhanced microwave absorption in nickel/hexagonal-ferrite/polymer composites. Appl Phys Lett 2006;89:28–31. https://doi.org/10.1063/1.2357565.